REACTIVE TRANSPORT IN NATURAL POROUS MEDIA:

CONTAMINANT SORPTION AND PORE-SCALE HETEROGENEITY

A Thesis
Presented to
The Academic Faculty

by

Babak Shafei

In Partial Fulfillment of the
Requirements for the Degree
Doctor of Philosophy in the
School Of Earth and Atmospheric Sciences

Georgia Institute of Technology
December 2012

REACTIVE TRANSPORT IN NATURAL POROUS MEDIA:

CONTAMINANT SORPTION AND PORE-SCALE HETEROGENEITY

Approved by:

Prof. Philippe Van Cappellen,
School of Earth and Environmental Science
University of Waterloo

Dr. Christian Huber
School of Earth and Atmospheric Sciences
Georgia Institute of Technology

Prof. Martial Taillefert
School of Earth and Atmospheric Sciences
Georgia Institute of Technology

Dr. Marc Stieglitz
School of Civil and Environmental Engineering
Georgia Institute of Technology

Dr. Christof Meile
School of Marine Sciences
University of Georgia

Date Approved: August 14, 2012

If the facts don't fit the theory, change the facts.

Albert Einstein

I would like to dedicate my thesis to my parents for their love, endless support and encouragement. They did not only raise and nurture me but also sacrificed their lives dearly over the years for my education and advised me at each stage of my life.

This thesis is also dedicated to my brother who deserves my wholehearted thanks for always being a source of inspiration and motivation.

ACKNOWLEDGEMENTS

I would like to thank my advisor, Prof. Philippe Van Cappellen, for his guidance throughout this study. This thesis would not have been possible without his support.

I sincerely thank faculty of Earth and Atmospheric Sciences specially Dr. Christian Huber and Prof. Martial Taillefert for their support during the last year of my Ph.D. Dr. Christian Huber has always been very sincere and generous with his knowledge, availability and feedback.

My special thanks go to my committee Dr. Christof Meile, Dr. Marc Stieglitz, Dr. Christian Huber, Prof. Martial Taillefert and Prof. Philippe Van Cappellen for their instructions and diligence in reviewing my thesis.

I would like to acknowledge all of my collaborators who I have shared great moments with: Dr. Raoul Couture, Dr. Lucie Pastor, Dr. Doug LaRowe, Kristen Mitchel and Ester Torres.

So many great scientists I met through AquaTRAIN project in Europe. My special thanks go to Prof. David Polya, Prof. Bernhard Wehrli, Prof. Gerhard Furrer and Dr. David Senn. I would like to thank all of my friends and colleagues at Utrecht University and ETH Zurich: Dr. Tom Jilbert, Dr. Susann Vollrath, Dr. Amir Raoof, Dr. Haydon Mort, Dr. David Aguilera, Dr. Andy Dale, Dr. Luis Rodrigues, Dr. Barbara Casentini, Dr. Cristina Jimenez, Dr. Jasmin Mertens, Dr. Simone Peter, Dr. Tonya Del Sontro, Nanina Blank, Nuttakan Wongfun, Dr. Roland Zurbrügg, Jan Landert. My visit wouldn’t be productive without them.

TABLE OF CONTENTS

LIST OF TABLES

LIST OF FIGURES

GLOSSARY

RTM	Reactive Transport Model
LEA	Local Equilibrium Assumption
SKIT	Separation of the Kinetically Influenced Term
EDA	Early Diagenesis Application
GWA	Groundwater Application
ODE	Ordinary Differential Equation
PDE	Partial Differential Equation
LB	Lattice Boltzmann
Pe	Peclet Number
Da	Damkohler Number
SRT or BGK	Single Relaxation Time
TRT	Two Relaxation Time

SUMMARY

Reactive Transport Models (RTMs) provide quantitative tools to analyze the interaction between transport and biogeochemical processes in subsurface environments such as aquatic sediments and groundwater flow. Because of the coupling of fluid and solute transport with biogeochemical reactions in the Earth's crust, modeling the dynamic behavior of the reactive transport processes is a challenging task. The complexity of the field is the consequences of a wide range of possible mechanisms and rates by which minerals, organisms and aqueous species may interact. In most of the cases because of the nonlinearity of these interactions, special treatment is required in order to incorporate them in mathematical models. Furthermore, a tremendous amount of research has shown the role and impact of scaling behavior of the reactive systems which stems from geologic heterogeneity. This heterogeneity refers to the ubiquitous spatial variability in subsurface formation materials, their physical and chemical heterogeneity. The complex interplay and non-linear coupling between surface reactions, flow and diffusive transport in an evolving porous medium (e.g. dissolution-precipitation) requires a pore-scale description and the ability to solve for the distribution of reactant inside pores.

Depending on the kinetics of the reactions, three different types of formulations have been proposed to describe reactions in RTMs. If the reaction rates are fast enough compared to the transport time scales, local equilibrium assumption (LEA) can be considered. Otherwise the reactions are considered to be kinetically controlled. In a fully

kinetic approach, theoretical or experimental reaction rate laws defined by ordinary differential equations (ODEs) can be used. Mass action laws which are algebraic expressions replace the ODEs in a fully equilibrium approach. If both slow and fast reactions coexist a mixed equilibrium-kinetic description may be the most appropriate. Mathematical description of sorption processes, one of the key processes that control the fate of dissolved constituents, often requires a choice between models based on the LEA and models involving reaction kinetics. Applying LEA simplifies the thermodynamics, mathematics and numerical analysis in many practical cases. Unfortunately, there are currently no general quantitative criteria to evaluate when LEA is a valid approximation in early diagenesis models. It is applied intuitively and many hypothesizes are made. The objective of Chapter 2 is to develop a quantitative, though approximate, criteria on the range of validity of LEA in aquatic sediments with irreversible heterogeneous reactions.

In Chapter 3, we present a one-dimensional (1-D) early diagenetic module, MATSEDLAB, developed in MATLAB. The interactive programming environment MATLAB provides a flexible platform in which an individual user can easily develop, adapt, test and manage models. Also by avoiding the hurdles of traditional programming languages, the user can focus on the definition and performance of her model, rather than on the technicalities of writing code. Because MATLAB provides many visualization capabilities, the graphical analysis of the results is also greatly facilitated and enhanced. The module, MATSEDLAB, provides templates for representing the reaction network, boundary conditions and transport regime, which the user can then modify to fit the particular early diagenetic model configuration of interest. We describe the theoretical background of the model and introduce the MATLAB *pdepe* solver, followed by

calibration and validation of the model by a number of theoretical and empirical applications. The latter are used to demonstrate the capabilities of MATSEDLAB, but also to illustrate how to modify existing templates.

In chapter 4 we introduce a new pore-scale model using lattice Boltzmann (LB) approach. It uses an iterative scheme for the chemical transport-reaction part and is therefore more accurate and stable for high reaction rates, moreover, it uses recent advances in the development of optimal advection-diffusion solvers within the lattice Boltzmann method framework. The calculations conducted in this study are divided into two separate sections. We present results for the dissolution and precipitation of a porous medium under different dynamical conditions, varying reaction rates and the ratio of advective to diffusive transport (*Pe*, Peclet number) for linear reactions. We focus on the effect of a given porosity change on the permeability of an identical porous structure subjected to different dissolution and precipitation conditions. We also compare the results for linear reactions to second order dissolution or precipitation reactions. The final set of calculations considers sorption reactions on a heterogeneous porous medium. We use our model to investigate the effect of heterogeneity on the pore-scale distribution of sorption sites and the competition between three different sorption reactions

CHAPTER 1: OVERVIEW

1.1 Reactive Transport In Natural Porous Media

In natural porous media, such as sediments and aquifers, complex biogeochemical processes regulate elemental cycling. Therefore it is a challenging task to predict the biogeochemical responses to variable environmental conditions and to quantify the contributions of individual processes on measured profiles of chemical species. Reactive Transport Models (RTMs) provide quantitative tools to analyze the interaction between transport and biogeochemical processes. They are used to investigate the fate and transport of a selected set of chemical species within a given compartment of the earth system (Aguilera et al., 2005). The basic principles of continuum theory of RTMs has been documented (Lichtner, 1985). Also the theoretical and numerical basis of RTMs has been reviewed (Yeh and Tripathi, 1989). In groundwater aquifers the utility of RTMs as tools to interpret the spatial and temporal distributions of chemical species has been demonstrated (Appelo, 1994; Valocchi et al., 1981). RTMs have been applied extensively to explain the redox zonation of aquatic sediments by coupled transport processes and biologically mediated oxidation of organic matter (Berner, 1980). Numerous models have been introduced to describe the early diagenetic transformations taking place in sediments (Boudreau, 1997; VanCappellen and Wang, 1996; Wang and VanCappellen, 1996).

1.2 Heterogeneity And Scaling

The physical transport in heterogeneous porous media and heterogeneous distributions of chemical and biological species in the subsurface exert scaling behavior of reactive transport processes. In most cases the fully characterization of the system is impossible because of the inherent random distribution of the material properties. RTMs are typically applied at larger scales, therefore spatial heterogeneities are necessarily ignored at scales smaller than the size of model discretization (Tartakovsky et al., 2007; Tartakovsky et al., 2008). Therefore scaling methods can be developed to include the pore-scale reactive transport processes and the impact of the heterogeneities.

Upscaling approaches are the mathematical means by which appropriate parameter values and processes associated with the corresponding reactive problem are assigned to the larger scale (Acharya, 2004). Numerous upscaling methods have been developed and reviewed in hydrologic sciences over the last few decades (Cushman et al., 2002) : e.g. mathematical homogenization, mixture and hybrid mixture theory, spatial averaging, moment methods, central limit or Martingale methods, stochastic-convective approaches, various other Eulerian and Lagrangian perturbation schemes, projection operators, renormalization group techniques, variational approaches, space transformational methods, continuous time random walks, and etc.

Usually the scale at which rate data are applied in RTMs (i.e., the scale of model discretization) differs from the scale at which rate data are measured. Typically most of the geochemical processes such as mineral dissolution and precipitation reactions are modeled using reaction kinetics measured in laboratory systems that are very different in

scale and structure from natural systems. Therefore scaling methods are required to prevent errors associated with laboratory-based rate laws (Li et al., 2006).

The development of scale-dependent reaction rates at the single pore and fracture scale, has been studied (Li et al., 2008; Meile and Tuncay, 2006). The comparison of the averaged mineral dissolution rates under various conditions of flow, pore size, and fracture length indicate that mismatch between reaction rates arise primarily where concentration gradients develop due to comparable rates of reaction and advective transport, and incomplete mixing via molecular diffusion (Li et al., 2008) .

The pore-scale reactive transport simulations in diffusion-dominated systems such as muddy sediments or soil aggregates have shown that inhomogeneous solute distribution within the pores can affect estimates of elemental turnover rates (Meile and Tuncay, 2006). Type of reaction, pore geometry, reaction kinetics and macroscopic concentration gradient are the factors that can impact on errors associated with large-scale rate estimates. Therefore a scaling correction term is introduced which can be evaluated numerically from measured macroscopic concentration gradients.

Physical and geochemical heterogeneity effects on the bioremediation of a contaminated site have been studied by integrating the field scale measurements, laboratory experiments and formulating reactive transport models (Englert et al., 2009; Scheibe et al., 2006). It has been shown that some reaction rates were influenced solely by physical properties of the subsurface environment, while reactions such as iron reduction was driven by geochemical heterogeneities. The predictive models were applied to explore the efficacy of the bioremediation processes on immobilization of the uranium and contaminated site cleanup.

Upscaling approaches have been employed to study the scale effects for different kinetics. A combination of analytical and numerical scaling approaches has been applied for Monod-type kinetics within a single pore, to obtain effective rate expressions at larger scales (Hesse et al., 2009). The results showed that the effective rate representation does no longer follow Monod-type kinetics. Therefore appropriate effective parameters relations must be introduced, which provide an acceptable approximation of degradation dynamics using an effective Monod-type reaction rate.

Upscaling of reaction-transport processes in porous media with fast or finite kinetics has also been observed in the literature (Kechagia et al., 2002). In this study for reaction-transport processes with fast kinetics (in the limit of thermodynamic equilibrium) conventional volume averaging was proposed to determine effective kinetic parameters.

Developing pore scale and hybrid models to capture the scale effects on the biogeochemical and transport processes is the field that continues to evolve with new interests and efforts. Upscaling subsurface processes and linking laboratory and field scale rates are still frontier research questions.

1.3 Treatment Of Reaction Processes: Equilibrium, Kinetic And Mixed Approaches

Three different types of formulations have been used to describe reactions in RTMs of subsurface environments. If the reaction rates are fast enough compared to the transport time scales, equilibrium can be assumed. Otherwise the reactions are considered to be kinetically controlled. In a fully kinetic approach, theoretical or experimental reaction rate laws defined by ordinary differential equations (ODEs) can be used. Mass action laws which are algebraic expressions replace the ODEs in a fully equilibrium

approach. If both slow and fast reactions coexist a mixed equilibrium-kinetic description may be the most appropriate.

Multiple examples of RTMs for natural porous media based on fully kinetic reaction descriptions have been appeared in the literature (Macquarrie et al., 1990; Soetaert et al., 1996). Many of them involve microbially-mediated redox reactions which are controlled by slow rates and therefore require a kinetic description. Homogeneous acid-base reactions and heterogeneous reversible sorption processes are usually described by equilibrium expressions.

CHAPTER 2: VALIDITY OF LOCAL EQUILIBRIUM ASSUMPTION IN EARLY DIAGENESIS MODELS

2.1 Introduction

Upon deposition of natural or man-made materials at the bottom of the body of the water, different physical, chemical and biological processes are taken place. Reactive Transport Models (RTMs) provide quantitative tools to analyze the interaction between transport and biogeochemical processes(Aguilera et al., 2005; Appelo, 1994; Lichtner, 1985; Valocchi et al., 1981; Yeh and Tripathi, 1989). Local and global non-equilibrium are the drivers of reactions in reactive transport problems which arise from deviations of the locally uniform species concentrations from the law of mass action and global non-transport-controlled mixing, respectively (Sanchez-Vila et al., 2007).

Sorption reactions are one of the major processes that control the fate of dissolved constituents released by diagenesis. Sorption in the context of the early diagenesis refers to the net uptake of the dissolved species from sediment pore water on to the surface of the enclosing solid phase. Here, the term is used in its general sense to include both uptake (adsorption) and release (desorption). Mathematical description of sorption processes often requires a choice between models based on the local equilibrium assumption (LEA) and models involving reaction kinetics (Jennings and Kirkner, 1984; Valocchi, 1985). If sorption reactions proceed instantaneously, i.e., are fast enough with respect to the bulk fluid flow rates, a local chemical equilibrium can be assumed. However, systematically applying LEA to all subsurface environments, such as aquatic

sediments and aquifers, regardless of their transport regime may result in erroneous predictions. In the case of early diagenesis application (EDA), such as lake bottom sediment, transport phenomena that occur on different timescales include burial of the particles, molecular diffusion of the dissolved constituents, solid and solute transport by bioturbation, and non-local solute transport by bio-irrigation (Boudreau, 1997). These transport processes are different than those prevailing in groundwater application (GWA), dominated by dissolved species advection, hydrodynamic dispersion and molecular diffusion. Hence, the selection of the LEA in GWA differs from GWA and should be done on a critical basis. A quantitative criteria to assess the validity of the LEA has been presented for one-dimensional steady-state flow through homogeneous soils using solute breakthrough curve time moments (Valocchi, 1985). Direct comparison of kinetic and local equilibrium formulations for solute transport affected by sorption reactions has allowed to identify the kinetically influenced term in the LEA formulation (Bahr and Rubin, 1987).

If an initial non-equilibrium condition relaxes to an equilibrium state over a distance and time period that is less than the spatial and temporal scales-of-interest, LEA can be treated as an acceptable assumption (Lichtner, 1988). These scales-of-interest depend on the particular problem under investigation and include the range of scales such as hundreds of meters for field investigations, the sub-meter for laboratory investigations and the pore-scale. Similar to spatial scales, deferent processes show a wide range of temporal scales. For the reactive transport modelers the spatial and temporal discretization size defines the scales-of-interest.

Most of the sorption studies of chemical species are carried out in batch experiments lasting for a relatively short time, usually from several hours to a few days. While these short time-scales can adequately allow to observation of the fast sorption of dissolved constituent in contact with pure mineral phases, it is likely that the system will approach equilibrium at a slower rate in field conditions. Different factors can lead to conditions of chemical disequilibrium frequently results. These are: i) heterogeneity of surface sites, ii) competition for available surface sites, iii) incorporation into the solid matrix, and iv) pore-scale diffusion.

Analytical solution representing the scale-of interest and describing one dimensional advective, diffusive and dispersive transport coupled with irreversible heterogeneous reaction has been derived for a single component (silica) (Knapp, 1989). The time and distance required for an impulse of fluid, initially undersaturated with respect to quartz, to relax to equilibrium was calculated for a wide range of reactions rates and transport conditions. The similar analytical approach has been developed to study the impact of the local scale non-equilibrium conditions on the transport controlled-reaction rate for a precipitation/dissolution problem (Sanchez-Vila et al., 2007) .

Applying the LEA principle whenever it is a good approximation simplifies the thermodynamics, mathematics and numerical analysis and in many practical cases it is the only possible approach. Unfortunately, there are currently no general quantitative criteria to evaluate when LEA is a valid approximation in early diagenesis models. LEA is applied intuitively and many hypothesizes are made. The objective of this chapter is to develop a quantitative, though approximate, guidelines on the range of validity of LEA in early diagenesis problem with irreversible heterogeneous sorption reactions.

2.2 Modeling Formulation

A general transient one-dimensional continuum representation of single species coupled mass transport and biogeochemical reaction in earth systems such as aquifers and aquatic sediments is expressed as a set of partial differential equations (PDEs) as below (Aguilera et al., 2005):

$$\frac{\partial}{\partial t}(\varepsilon C_i) = \left[\frac{\partial}{\partial x}\left(\varepsilon D \frac{\partial C_i}{\partial x}\right) - \frac{\partial}{\partial x}(\vartheta \varepsilon C_i)\right] + \varepsilon \sum r_m \quad (2.1)$$

where C_i is the concentration of component i, x is the position along the 1-D spatial domain and t denotes the time. $\sum r_m$ represents the summation of all rate expressions for slow chemical reactions affecting concentration C_i. Different units are used for EDA and GWA applications. In EDA solute and solid concentrations are expressed in moles/$L_{porewater}$ and moles/g_{solid} respectively, and concentrations in moles/$L_{porewater}$ for the solutes and moles/$g_{total\ sediment}$ for the solids in the GWA. The variables ε, D and ϑ are generic and will take different meanings depending on the studied environment. Table 2.1 shows their definitions for the GWA and EDA.

In GWA we assume that the solid matrix is nondeformable, i.e., $\frac{\partial \varphi}{\partial t} = 0$ (Bear, 1972). Advection in EDA refers to the bulk flow of solids or pore water relative to an adopted reference frame. The velocity, V_f, of the pore water is made of the two components one due to compaction and the other due to externally impressed flow which as an example happens in the case of the submarine discharge of the fresh water percolating up in the sediments. When compaction is negligible, porosity within a given layer does not change during burial. In this case, in the absence of externally impressed flow, advection of the pore water will be essentially the same as the rate of the burial of the solids and we use the concept of steady-state compaction (Berner, 1980).

Table 2-1: Meaning of the generalized variables in Equation (2.1) for different subsurface environments: φ [-], porosity; V_f [LT^{-1}], externally imposed flow velocity; ω[LT^{-1}], burial velocity defined with respect to the sediment water interface (SWI); D_b[L^2T^{-1}], bioturbation coefficient; D_d molecular diffusion coefficient, D_{disp}[L^2T^{-1}] $=\propto_L |V_{flow}|$, longitudinal dispesion where $\propto_L$ [L] is the longitudinal dispersivity.

	Aquatic sediments		Groundwater flow	
	Solids	Solutes	Solids	solutes
ε	1-φ	φ	1-φ	φ
v	ω	$V = \omega + V_f$	0	V_{flow}
D	D_b	$D_s = D_b + D_d$	0	D_{disp}
δ	0	1	0	1

This means that the sedimentation rate is constant and $\frac{\partial \varphi}{\partial t} = 0$. We are interested in comparing the LEA applicability in both groundwater and sediment subsurface environments. We will apply the approach derived by Bahr and Rubin (1987) for LEA applicability in GWA, where the porosity was assumed to be constant with respect to depth. Without loss of generality, we will apply the same assumption along with steady-state compaction.

Sorption process of a single species can be represented as following reaction:

$$A_{(aq)} + S_{(s)} \leftrightarrow AS_{(s)}$$

where $A_{(aq)}$ is the sorbate concentration in aqueous phase, $S_{(s)}$ is the available reactive surface site of the media for the sorbate sorption and $AS_{(s)}$ is the concentration of the sorbate on solid phase. The formulation of sorption depends upon the rate by which it occurs. If the rate of the sorption is slower or the same order of magnitude as transport

processes which affect dissolved species concentrations, then adsorption reaction at a given depth may not be in equilibrium with the enclosing solids. In this case it is described by the kinetic rate laws and is lumped along with other rate-controlled reactions, i.e. $\sum r_m$, such as dissolution, precipitation, bacterial decomposition and etc. By contrast, if the rate of the sorption is very fast, compared to the transport processes, one may assume the sorption equilibrium is present at all depths and times. Then, various isotherms that are algebraic expressions relating adsorbed and dissolved species concentrations are applied for mathematical formulation.

For the proposed sorption conceptual model above, we assume the net rate of reaction *r*, ignoring activity coefficients, can be described as a first-order linear kinetic expression with respect to the both sorbent and sorbate concentrations. Furthermore it is assumed that the concentration of the sorbent is much greater than that of the sorbate, thus the available sorption surface site would virtually remain unchanged during the process (i.e., the rate law can be treated as a pseudo-order reaction). The sorption rate results in to the following form:

$$r = \varphi \frac{dc}{dt} = -\rho_b(1-\varphi)\frac{ds}{dt} = -\varphi k_f c + \rho_b(1-\varphi)k_r s \qquad (2.2)$$

where *c* is the concentration of the dissolved species *A* and *s* is the concentration of the sorbed species AS. k_f and k_r are rate constants for the forward and reverse reactions and both have the units of T^{-1}. The dry sediment density is denoted by ρ_b [M_{solid}/L_{solid}]. It should be noted that the rate law defined in Equation (2.2) indicates the contribution to changes in *c* and *s* due to the chemical reactions. The physical nonequilibrium will not be considered where the overall sorption rate is controlled by the rate at which the solute is transported to and from the reaction soil surfaces. In these models fluid inside the porous

aggregates is assumed stagnant, and thus the total liquid phase is partitioned into mobile and immobile zones.

In the GWA, solid phase is immobile and solute is transported through the pore space. In contrast, in sediments the solid phase is subjected to advection primarily due to the burial deposition of fresh sediment layers. This process is encompassed within the advective term of *w* in the mass balance equation (MBE) of (2.1). In other words, in EDA, the adsorbed solid concentrations are not only influenced by the adsorption reactions but the transport processes such as sedimentation and bioturbation. The nonequilibrium transport formulation of the sorption reaction consists of two MBE's including one PDE for each of the solute and sorbed species:

$$\frac{\partial c}{\partial t} = \left[\frac{\partial}{\partial x}\left(D_s \frac{\partial c}{\partial x}\right) - \frac{\partial}{\partial x}(Vc)\right] - k_f c + \frac{\rho_b(1-\varphi)}{\varphi} k_r s \tag{2.3}$$

$$\frac{\partial s}{\partial t} = \left[\frac{\partial}{\partial x}\left(D_b \frac{\partial s}{\partial x}\right) - \frac{\partial}{\partial x}(ws)\right] + \frac{\varphi}{\rho_b(1-\varphi)} k_f c - k_r s \tag{2.4}$$

It is seen from Equation (2.4) that transport processes are included in MBE of solid phase. For local equilibrium, the net rate of the reaction is zero and (2.2) can be solved to yield the algebraic isotherms of

$$s = \frac{K_d}{F} c \tag{2.5}$$

where $F = \frac{\rho_b(1-\varphi)}{\varphi}$ is the conversion factor and $K_d = \frac{k_f}{k_r}$ is the equilibrium distribution coefficient. The general MBE which expresses the effects upon the depth and time distribution of a dissolved constituent, of diffusion, pore water advection, burial due to deposition and equilibrium adsorption has been presented (Berner, 1976). For the special case of linear adsorption isotherm (2.5), it is expressed by:

$$\frac{\partial c}{\partial t} = \frac{1}{R_f}\left\{\left[\frac{\partial}{\partial x}\left(D_s \frac{\partial c}{\partial x} + FD_b \frac{\partial s}{\partial x}\right)\right] - \left[\frac{\partial}{\partial x}(Vc + Fws)\right]\right\} \tag{2.6}$$

In this equation, it is assumed that the solid phase surface properties are constant with depth and time.

LEA applicability in GWA has been investigated (Bahr and Rubin, 1987; Valocchi, 1985). Bahr and Rubin (1987) introduced SKIT (separation of the kinetically influenced term) method, which calls for parallel derivations of LEA, and nonequilibrium (SKIT) formulations for a given solute transport problem. This formulation contains exactly the same terms as the LEA one plus an additional nonequilibrium term. The SKIT procedure for EDA begins by multiplying both sides of the Equation (2.3) in φ and Equation (2.4) in $\rho_b(1-\varphi)$ and then adding both of them which yields in:

$$\frac{\partial c}{\partial t} = \left[\frac{\partial}{\partial x}\left(D_s \frac{\partial c}{\partial x} + FD_b \frac{\partial s}{\partial x}\right)\right] - \left[\frac{\partial}{\partial x}(Vc + Fws)\right] - F\frac{\partial s}{\partial t} \tag{2.7}$$

By rearranging the Equation (2.4) to obtain an explicit expression for the adsorbed species *s* we will have:

$$s = \frac{1}{k_r F}\left\{\frac{\partial c}{\partial t} - \left[\frac{\partial}{\partial x}\left(D_s \frac{\partial c}{\partial x}\right) - \frac{\partial}{\partial x}(Vc)\right]\right\} + \frac{k_f}{k_r F} \quad c \tag{2.8}$$

Differentiating Equation (2.8) with respect to time results in:

$$\frac{\partial s}{\partial t} = \frac{1}{k_r F}\frac{\partial}{\partial t}\left\{\frac{\partial c}{\partial t} - \left[\frac{\partial}{\partial x}\left(D_{dif} \frac{\partial c}{\partial x}\right) - \frac{\partial}{\partial x}(Vc)\right]\right\} + \frac{k_f}{Fk_r} \quad \frac{\partial c}{\partial t} \tag{2.9}$$

Substituting Equation (2.9) into (2.7) we have:

$$\frac{\partial c}{\partial t} = \frac{1}{R_f}\left\{\left[\frac{\partial}{\partial x}\left(D_s \frac{\partial c}{\partial x} + FD_b \frac{\partial s}{\partial x}\right)\right] - \left[\frac{\partial}{\partial x}(Vc + Fws)\right]\right\} - \frac{1}{k_f + k_r} L(c) \tag{2.10}$$

where $L(c) = \frac{\partial}{\partial t}\left\{\frac{\partial c}{\partial t} - \left[\frac{\partial}{\partial x}\left(D_s \frac{\partial c}{\partial x}\right) - \frac{\partial}{\partial x}(Vc)\right]\right\}$.

Equation (2.10) is referred to the SKIT formulation of diagenesis equation. Comparing Equations (2.6) and (2.10), show that SKIT Equation (2.10) contains an additional kinetically influenced term. This term is the product of the differential factor of $L(c)$ and the prefix factor with the dominator defined as

$$p_d = k_f + k_r \tag{2.11}$$

Each term in the MBE of solid and dissolved species expresses a contribution resulting from physical and chemical phenomenon. Obviously, not all these processes are of the same order of magnitude and time scales. It may, therefore, be of interest, once a complete model has been developed, and before attempting to solve it, to analyze the order of magnitude of the various terms. This can give us an insight to identify the dominant processes. The level of dominance of a term can be determined by comparing it with other terms that appear in the same balance equation through introducing the dimensionless parameters.

The LEA and SKIT formulations can be converted to dimensionless forms employing the following substitutions:

$$X = x/x_r$$

where $x_r$is the reference length,

$$T = Vt/R_f x_r$$

$$\bar{c} = c/c_r$$

$$\bar{s} = Fs/c_r$$

$$\gamma = w/V$$

where c_r is a reference concentration,

$$Pe1 = x_r V/D_s$$

a Peclet number I and

$$Pe2 = x_r V/D_b$$

a Peclet number II,

$$Da1 = x_r k_f/V$$

a Damkohler number I and

$$Da2 = x_r k_r / V$$

a Damkohler number II.

Using the above definitions, the dimensionless LEA and SKIT Equations (2.6) and (2.10) will be:

$$\frac{\partial \bar{c}}{\partial T} = \frac{1}{Pe1}\frac{\partial^2 \bar{c}}{\partial X^2} + \frac{1}{Pe2}\frac{\partial^2 s}{\partial X^2} - \frac{\partial \bar{c}}{\partial X} - \gamma \frac{\partial \bar{s}}{\partial X} \tag{2.12}$$

and

$$\frac{\partial \bar{c}}{\partial T} = \frac{1}{Pe1}\frac{\partial^2 \bar{c}}{\partial X^2} + \frac{1}{Pe2}\frac{\partial^2 \bar{s}}{\partial X^2} - \frac{\partial \bar{c}}{\partial X} - \gamma \frac{\partial \bar{s}}{\partial X} - \frac{1}{Da1+Da2}\frac{\partial}{\partial T}\left(\frac{1}{1+\frac{Da1}{Da2}}\frac{\partial \bar{c}}{\partial T} - \frac{1}{Pe1}\frac{\partial^2 c}{\partial X^2} + \frac{\partial c}{\partial X}\right) \tag{2.13}$$

respectively. Comparing the dimensionless LEA and SKIT formulations reveals the extra kinetically influenced term in SKIT formulation. The dominator of the dimensionless prefix factor in this term is:

$$P_D = Da1 + Da2 \tag{2.14}$$

which is a function of the summation of the *Da* numbers. The fact that the kinetic information appears only in the prefix dominator defines its critical factor in determining the applicability of LEA models in early diagenesis equation which is similar to the groundwater application. The kinetic term is negligible when with increases in rate constants or decrease in porewater velocity, the differential factor does not increase in magnitude faster than P_D.

2.3 Use Of the Prefix Dominator To Determine Applicability Of LEA Models

We use the results of early diagenesis simulations of solute and solid species to explore the magnitude of the kinetically influenced term. Consequently the extent of departure from LEA results depends on the magnitude of the prefix factor. A reactive

transport model is developed to simulate dimensionless forms of diagenesis Equations (2.3) and (2.4). A detailed description of the model can be found in Chapter 3. The upper boundary condition at x = 0 for a solute is equal to its bottom water concentration at sediment water interface (SWI) and has the general form of

$$c(0,t) = c_0 \tag{2.15}$$

Zero concentration gradients at depth is imposed as lower boundary condition:

$$\frac{\partial}{\partial x}[c(x = x_L, t)] = 0 \tag{2.16}$$

Assuming c_0 and x_L (sediment thickness) as the reference concentrations and length, the dimensionless forms of the Equations (2.15) and (2.16) will be:

$$\bar{c}(0,T) = 1 \tag{2.17}$$

and

$$\frac{\partial}{\partial X}[\bar{c}(X = 1, T)] = 0 \tag{2.18}$$

At t = 0, the initial conditions of the form

$$c(x,0) = 0 \tag{2.19}$$

should be satisfied which in dimensionless form is:

$$\bar{c}(X,0) = 0 \tag{2.20}$$

For the adsorbed species, flux continuity condition is usually imposed at SWI:

$$(ws - D_b \frac{\partial s}{\partial x})_{x=0} = J/F \tag{2.21}$$

In which J (M L^{-2} T^{-1}) is the depositional flux. The dimensionless form of (2.21) is derived as:

$$(\gamma \bar{s} - \frac{1}{Pe2}\frac{\partial \bar{s}}{\partial x})_{X=0} = \bar{J} \tag{2.22}$$

where $\bar{J}$ is the dimensionless depositional flux equals to $J/(VC_0)$.

The departure from LEA at a given distance L' from the sediment water interface and time t can be quantified as the ratio of the measured sorbed phase concentration to the one that would be in equilibrium with the solution phase:

$$\mu_{L'}(t) = \frac{s(L',t)}{s_{eq}(L',t)} \tag{2.23}$$

or in dimensionless form

$$\mu_L(T) = \frac{\bar{s}(L,T)}{\bar{c}(L,T)} \tag{2.24}$$

where $L = L'/x_L$. By definition LEA is applicable when:

$$\mu_L(T)_{LEA} = 1 \tag{2.25}$$

The values of $\mu_L(T)$ are plotted versus T in Figure 2.1 for different Da numbers. All the simulations are run based on the biturbation and diffusion coefficient values from (Couture et al., 2010b). They studied non-steady state modeling of kinetically controlled arsenic sorption in lake sediments. The molecular diffusion coefficient for arsenic was 5.8×10^{-6} cm^2/s. Bioturbation coefficient was constrained as 2.2×10^{-9} cm^2/s. The diagenetic reactions are continued over the 15 cm thickness of the sedimentary column. The average sedimentation rate of 0.131 cm/yr was applied. There was no porewater advection due to SGD or porosity change; in other words γ was equal to unity. However we run the simulations for different values of γ to examine the effect of porewater flow on deviation from LEA and it will be discussed in following section. In this simulation, the rates of the adsorption and desorption reactions are assumed to be equal. In other words K_d equals to one and $Da1=Da2=P_D/2$. This results in R_f value of 2, where $R_f = 1 + K_d$ is frequently referred to as the retardation factor in GWA. Later we will examine the dependency of the LEA applicability on the R_f values. Departures from LEA results in $\mu_L(T) < 1$. For all conditions $\mu_L(T)$ approaches to one as T increases. The

ratio $\mu_L(T)$ remains close to zero for the extreme case of a reaction whose rate is so slow in relation to flow rates that at any finite time the mass transfer between solute and solid phase is almost zero. According to Figure 2.1, for the dimensionless *T* value of 3.33 which is associated with an early diagenesis period of 100 years, the value of $\mu_L(T)$ will be less than 10 percent when *Da*1=*Da*2=0.005 and 0.05. This means a considerable deviation from LEA and its failing in simulating arsenic sorption in early diagenesis application. For *Da*1=*Da*2=0.05 the results will be improved comparing to the last case since $\mu_L(T)$ reaches to value of almost 60 percent. The most confidential results in applicability of LEA will happen in *Da*1=*Da*2=5. Almost 90 percent of LEA will be reached in this case.

As it is seen the ratio $\mu_L(T)$ is time dependent and for early times (prior to arrival of the solute front at *L*) or at the extreme of the late times when the solute has reached its concentration at sediment water interface is of no value in determining the applicability of LEA models. One convenient time at which to evaluate $\mu_L(T)$ in order to detect significant departures from LEA transport is the time corresponds to half of the concentration of at SWI, i.e., the time τ at which

$$\bar{c}(L,\tau) = \bar{c}(0,\tau)/2 \tag{2.26}$$

The ratio computed for time τ is defined as

$$E_L = \mu(L,\tau) \tag{2.27}$$

will be used to quantify the departure from LEA.

Dimensionless concentrations of the dissolved and sorbed species were obtained using

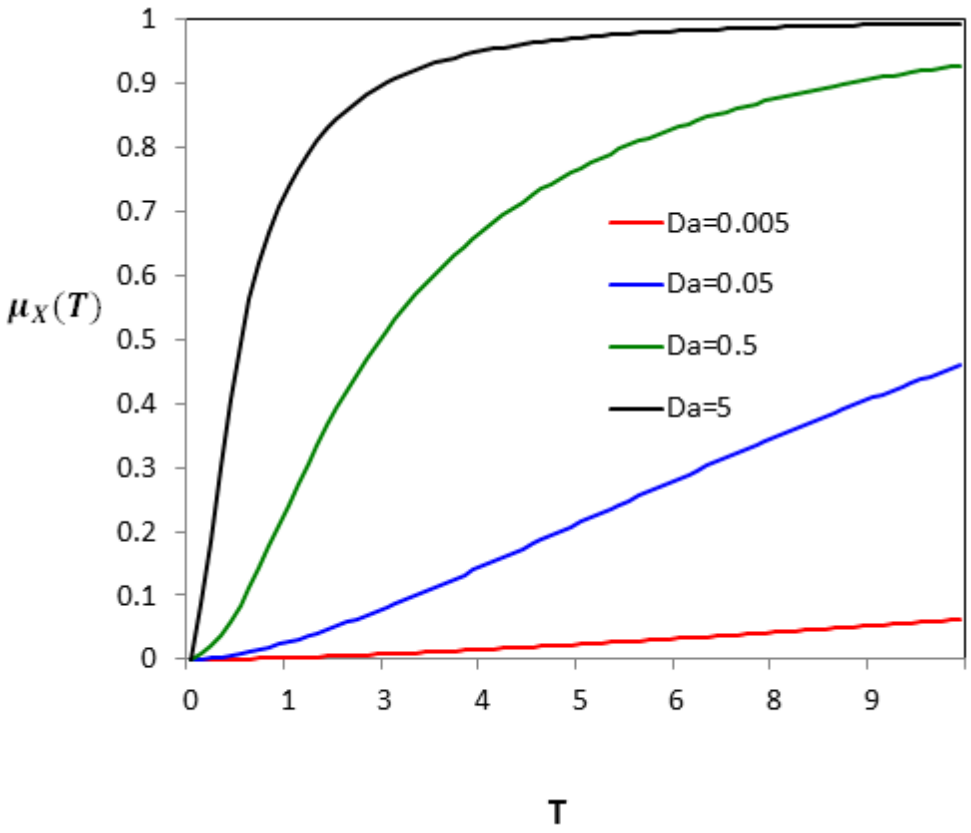

Figure 2-1: Influence of transport time on a measure of departure from equilibrium. Four curves are based on simulation of EDA using the identical values of w=0.131 cm/yr, L=15 cm, D_{dif}=160 cm^2/yr, D_b=0.0694 cm^2/yr, γ=0.1, $Da1$=$Da2$=Da and X=1

combinations of transport parameters giving P_D's ranging from 1.1 to 50. It resulted in E_L's ranging from 0.84 to 0.99 and are illustrated in Figure 2.2. As it is shown in all of the cases, the dissolved species have not yet reached their maximum concentration. In cases that LEA is satisfied, the plots of dimensionless concentrations of the dissolved and sorbed species would coincide at all times. At a given distance and time, higher solute concentrations and lower sorbed concentrations with respect to those predicted using LEA models, express departures from LEA. For example it can be seen that for simulations yielding computed values of E_L=0.84, the diagenesis modeling results are significantly different than the ones predicted by the corresponding LEA model. For the simulation with P_D=3.2 resulting in E_L=0.94, the sorbed species dimensionless concentrations almost coincide with the dimensionless solute concentrations. For E_L =0.98 and E_L =0.99, the simulation using P_D =17 and P_D=50, the two concentrations are indistinguishable from the ones using LEA model. It suggests that the LEA is definitely applicable when $E_L \geq 0.98$ and is also a reasonable approximation when $E_L \geq 0.90$.

2.4 Results And Discussion

By examining dimensionless form of the new kinetics-based sorption formulation in EDA, we may interpret significance of various transport processes, qualitatively. As it is seen from Equation (2.12), new dimensionless numbers, $Pe2$ and γ, are introduced compared to the dimensionless form of MBEs of GWA. This stems from the transport of the solid phase in EDA. $Pe1$ compares the advection rate of the dissolved species relative to sum of bioturbation and molecular diffusion while $Pe2$ compares the pore water advective flux with respect to the bioturbation only. Note that since in both definitions pore water velocity, V is used, for any diagenesis scenario $Pe1<Pe2$. $Pe2$ does

not reflect the typical definition of peclet number of the solid phase in the sediments in which the sedimentation rate is compared with bioturbation rate instead of pore water velocity. For this purpose $Pe2^* = \frac{wx_L}{D_b}$ is introduced to describe the sorbed phase transport regime properly. In diffusion dominant scenarios for both sorbed and dissolved species ($Pe2^* \ll 1$ and $Pe1<<1$), we need to define different forms of *Da* number which will enable us to compare the reaction rates with respect to diffusion/bioturbation processes. It is defined as $Da1^* = \frac{k_f {x_L}^2}{D_s}$ and $Da2^* = \frac{k_f {x_L}^2}{D_b}$ for the dissolved constituent and sorbed species, respectively. They can also be written as $Da1^* = Da1 \times Pe1$ and $Da2^* = Da1 \times Pe2$. Note that same definition can be used by applying desorption rate coefficient as the reaction characteristic time scale. Predictions based on these numbers can be summarized as below:

– $Da1^* \ll 1$ (or $Da2^* \ll 1$), the reaction is referred to as a *slow reaction* with respect to dissolved species (or the sorbed ones).

• When $Pe1>>1$ (or $Pe2^* \gg 1$), transport by advection dominates over that by diffusion plus bioturbation (or bioturbation only). If also:

– $Da1 \gg 1$ (or $Da1/\gamma \gg 1$), the reaction is referred to as a *fast reaction* with respect to dissolved species (or the sorbed ones).

• When $Pe1<<1$ (or $Pe2^* \ll 1$), transport by diffusion plus bioturbation (or bioturbation

– $Da1 \ll 1$ (or $Da1/\gamma \ll 1$), the reaction is referred to as a *slow reaction* with respect to dissolved species (or the sorbed ones).

γ is the ratio of the sedimentation rate of the solid species to the advection rate of dissolved species.

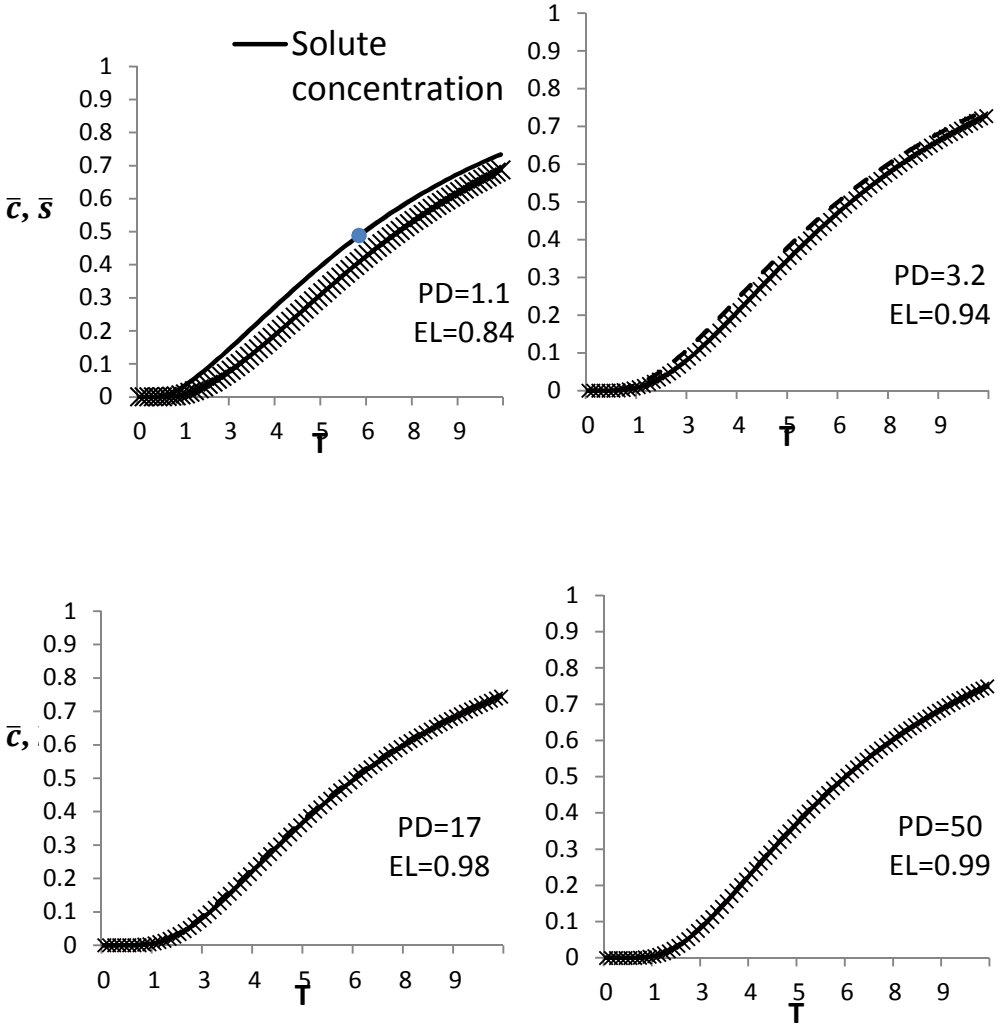

Figure 2-2: Measure E_L as an indicator of departure from LEA. Measure's effectiveness is demonstrated by four pairs of dimensionless concentrations using the values of w=0.131 cm/yr, x_L=15 cm, D_{dif}=160 cm^2/yr, D_b=0.0694 cm^2/yr, $\gamma = 0.1$ and indicated values of P_D.

Advection rate is in fact the summation of two vectors ($V = w + V_f$), that can have the same or opposite directions with respect to each other. Depending on the direction and size of the advection term, γ values will change. If the pore water velocity (V_f) happens in the same direction of the solid phase deposition, then $0 < \gamma < 1$. In the cases such as upward submarine groundwater discharge, where pore water velocity is in the opposite direction of the sediment deposition, γ value is dependent on the size of the pore water velocity. If $|V_f| < w$ then $\gamma > 1$ otherwise $\gamma < 0$. When $\gamma = 1$, it implies that externally impressed flow is negligible. In other words, in the absence of externally impressed flow, both adsorbed and dissolved species are buried at the same rate. If $\gamma = 0$ it is switched into GWA in which solid phase is immobile.

Detailed description of LEA applicability requires the evaluation of different ranges of all the discussed dimensionless parameters. Here we will focus on the effects of newly introduced parameters. Applying the values from Couture et al, (2010b) results in $Pe1$=0.122, $Pe2$=283.14 and $Pe2^*$=28.31. It is seen that $Pe2$ is 3 orders of magnitude greater than $Pe1$. Also while dissolved constituent experiences a diffusion dominant transport, sorbed species will have an advection-dominant transport. According to the above discussion, the sorption process can be referred as a fast reaction if $Da1^* \gg 1$ or $Da1 \gg 1/Pe1$ and $Da1 \gg \gamma$. Therefore when $Da1 \gg \max\{1/Pe1, \gamma\}$, the fast reaction condition is applicable.

In the following discussions we assume that the E_L values of >0.90 are the critical ones where the LEA is applicable and E_L=0.90 in all the parametric analyses will be the upper boundary of LEA application. The lower boundary will be determined based on the

special features for each scenario. There will be cases where it is needed to present E_L boundaries as low as 0.60 to observe the effects of that specific parameter on its values.

To examine the effect of the pairs of the critical dimensionless numbers on E_L values, the plots will be presented in 3 different ways. First the 3-D figures of E_L as a function of two dimensionless parameters are plotted. Then 2-D mapping of E_L values in the dimensionless parameters surface will be shown. This will help us to simply identify the zones of LEA applicability. Furthermore, the boundaries of these zones will be specifically presented.

2.4.1 Comparing GWA And EDA

As stated before, one of the main differences between the groundwater flow and early diagenesis models is that the solid phase in sediments is subjected to the transport processes. Our goal is to investigate the effect of solid phase transport via sedimentation and bioturbation on applicability of LEA in the sediments. To do that, we simulated the same problem of Figure 2.2, in a porous media where the solid phase is immobile which will result in $\gamma = 0$. Furthermore transport of solid phase via bioturbation is no longer considered and therefore D_b=0. This is similar to GWA with a difference that the groundwater advection rates are not in the same order of magnitudes reported in the literature. As we assume $\gamma = 0.1$ in EDA, it will give us the advection rate of V=1.31 *cm/yr* for the porewater flow which is one order of magnitude smaller than the typical groundwater velocities in 10-1500 *cm/yr* range.

As it is illustrated in Figure 2.3, the results show more deviation from LEA in immobile solid phase condition comparing to Figure 2.2 where solid phase is mobile. For example, for P_D=1.1, E_L value of 0.69 is obtained which is less than E_L=0.84 for the same

case in EDA. When the solid phase is immobile the lag between dissolved and sorbed species concentrations is increased i.e. the results are deviated more from the local equilibrium condition unless the adsorption rates are greater than the transport rates. This is true since as pore water and solid phase are advected in the same direction, porewater/solid phase chemical exchange increases. As P_D values are increased to 17 and 50, E_L values of 0.97 and 0.99 are reached. These E_L values are almost the same as the ones from EDA simulations. This shows that, the solid phase transport effect in EDA vanishes as P_D increases and LEA can be applicable in both GWA and EDA.

To examine the effect of the advection velocity on deviation from LEA, we decreased the advection rate to V=0.0131 *cm/yr*. The results are shown in Figure 2.4. This caused the dissolved concentrations to reach their maximum value and no tailing is observed. E_L values such as 0.02 obtained which shows the failure of the LEA, drastically. Still in this case, we can get reasonable approximations using LEA by increasing P_D value to 50.

2.4.2 Effect Of γ

In the dimensionless model of EDA, by setting a constant value for the sedimentation rate *w*, the dissolved species advection rate is determined by assigning different values for γ. We run various simulations using γ values of -1.5, -1, -0.5, 0.5, 1 and 1.5. The results are shown in Figure 2.5. In all the simulations the P_D value is fixed at the value of 1.1. The E_L values, flow and sedimentation rate are summarized in Table 2.2. It is shown that in either of the cases of $\gamma > 0$ or $\gamma < 0$ by increasing $|\gamma|$ the results deviate more from LEA. This means that, irrespective of the direction of the solid and dissolved

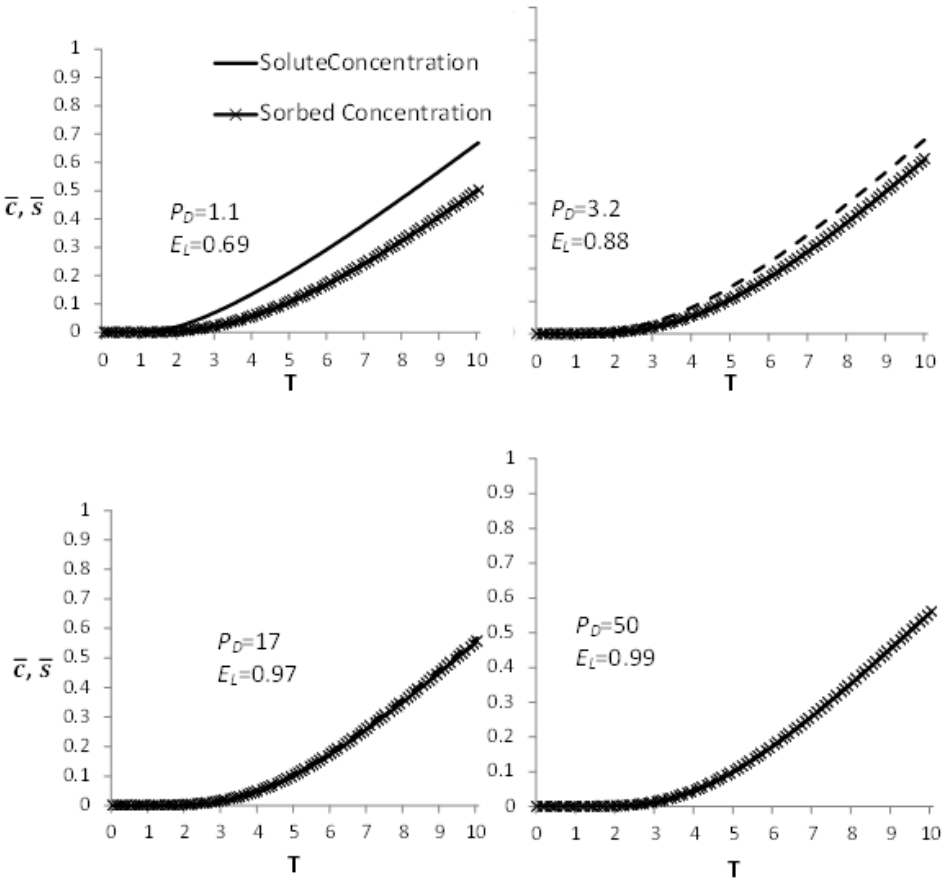

Figure 2-3: E_L values for the case of immobile solid phase. Measure's effectiveness is demonstrated by four pairs of dimensionless concentrations using the values of V=1.31 cm/yr, L=15 cm, D_{dif}=160 cm^2/yr, D_b=0 and indicated values of P_D.

Table 2-2: E_L values for different values of γ. Measure's effectiveness is demonstrated by four pairs of dimensionless concentrations using the values of w=0.131 cm/yr, L=15 cm, D_{dif}=160 cm^2/yr, D_b=0.0694, P_D=1.1 and indicated values of γ.

γ	w	V	E_L
0.1	0.131	1.310	0.84
0	0	1.310	0.69
0.5	0.131	0.262	0.55
1	0.131	0.131	0.31
1.5	0.131	0.087	0.21
-0.5	0.131	-.262	0.05
-1	0.131	-0.131	0.025

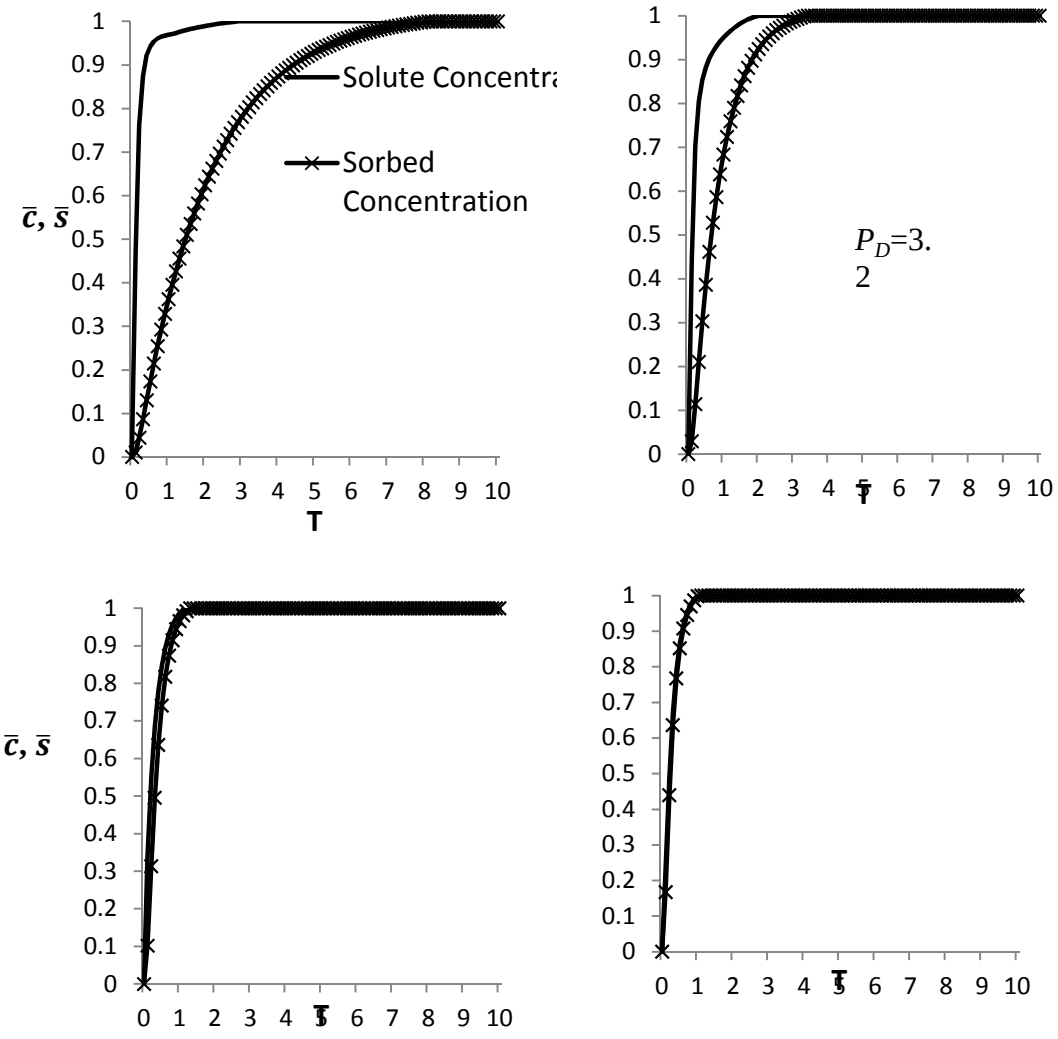

Figure 2-4: E_L values for the case of immobile solid phase. Measure's effectiveness is demonstrated by four pairs of dimensionless concentrations using the values of V=1.31 cm/yr, x_L=15 cm, D_{dif}=160 cm^2/yr, D_b=0 and indicated values of P_D.

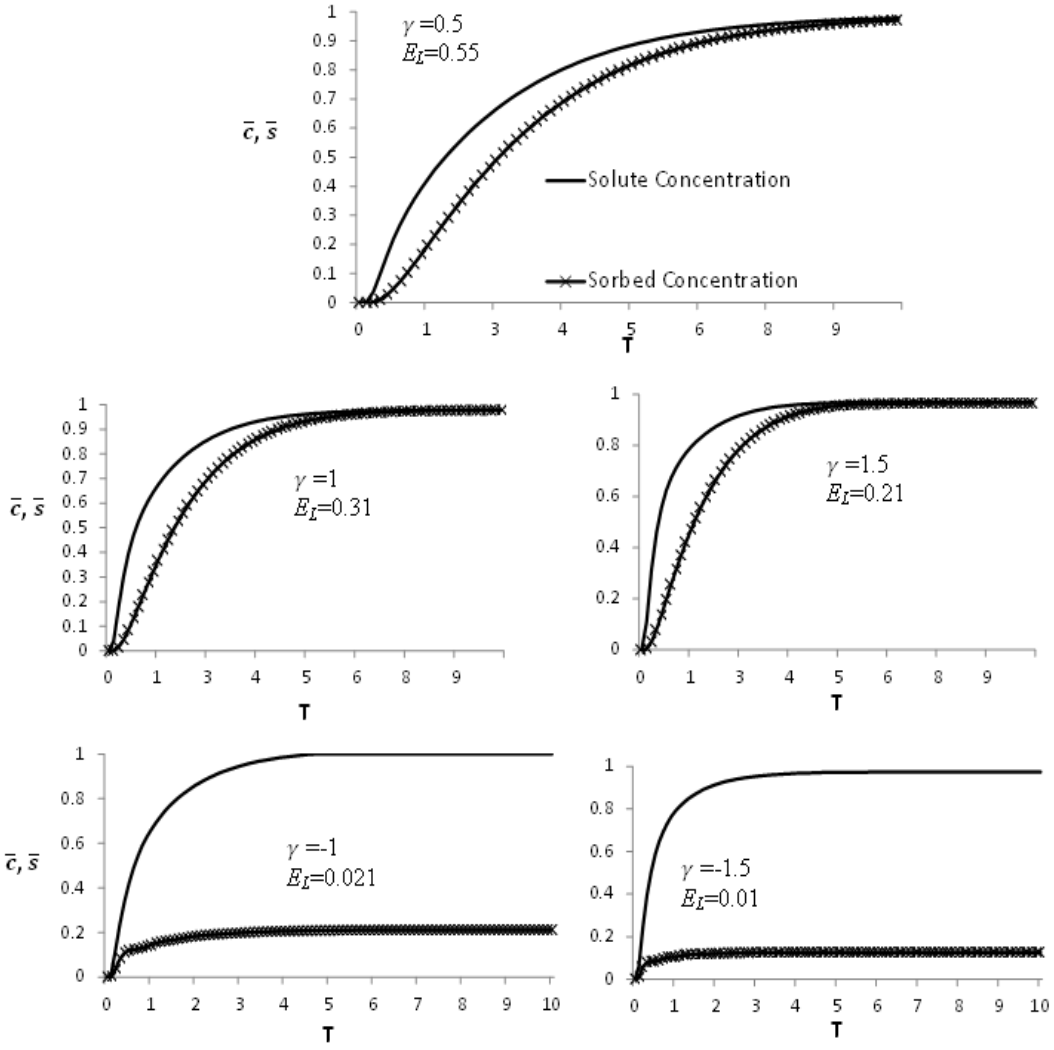

Figure 2-5: E_L values for the different values of γ including positive and negative ones.

if the porewater velocity increases the LEA will yield better approximation expect in conditions where $|V_f| > w$ and $\gamma < 0$. The E_L values differ substantially from each other as sedimentation rates and porewater advection rate happen at opposite directions. For example when γ =1.5 the E_L value of 0.21 is obtained. The correspondent value of E_L while $\gamma = -1.5$ yields to the value as low as 0.01.

2.4.3 Effect Of Da1 And Da2

Figure 2.6 illustrates E_L values using combinations of transport parameters and giving *Da*1 and *Da*2 ranging from 0 to 50. The area of E_L >0.9 contains a small fraction of the domain which results from *Da*1<1 and *Da*2>10. This feature is not observed for the case of *Da*2<1. In other words distribution of E_L values with respect to the *Da*1=*Da*2 line is asymmetric. This shows unequivalent influence of *Da*1 and *D*a2 on E_L values. When *Da*1<1 then the pore water advection dominates adsorption reaction. Therefore adsorption reaction is slower with respect to the transport processes. However, *Da*2>1 and $Pe2^* > 1$ results in a fast desorption process. The overall sorption reaction is even faster when *Da*2>10. This proves that how difference in characteristics between the dissolved and adsorbed species in aqueous and solid phases can control the overall rate of the reaction. Any particular dissolved species when adsorbed is much more concentrated compared to its concentration in the solution. It implies that any small change in the concentration of the adsorbed phase can greatly effect on the solution. For this reason although adsorption reaction is slow, fast desorption rate can result in LEA conditions.

2.4.4 Effect Of Pe1 And P_D

P_D and *Pe*1 effects on E_L values are plotted in Figure 2.7. The boundaries of E_L =0.90 and 0.70 are presented in the two dimensional view. As it was expected, by increasing P_D

value the kinetically influenced term in the SKIT formulation tends to zero and LEA is satisfied. Increasing $Pe1$, results in failure of LEA applicability as LEA values decrease. If P_D accepts smaller values such as P_D <<2, then $Da1^* \ll 1$ which results in slow sorption reactions. That is why we observe a small region of low E_L values indicating slow reactions on the left side of the plots. As we increase P_D values, then $Da1^* \gg 1$ which results in faster sorption reactions. Note that based on the order of the $Pe1$, our simulations run in [0,1] range. Different features can be expected as we theoretically run for $Pe1$>1.

2.4.5 Effect Of R_f And P_D

Figure 2.8 shows the effect of R_f and P_D values effect on E_L values. Here P_D values are varied in the domain of [0,50] while R_f values of [0,100] are used. Comparison with the results of Figure 2.7 dramatically shows the influence of the increasing of the retardation factor. Based on this E_L distribution, the minimum value of P_D =7 and R_f =40 are required to reach the values of E_L >0.90. The E_L boundaries of 0.90 and 0.60 are plotted in the two-dimensional view.

2.5 Conclusion

The mathematical approach presented leads to parallel derivations of LEA and SKIT diagenesis formulations. The form of the SKIT equation indicates the equivalence of the error associated with the use of an LEA and the error of neglecting the kinetically influenced terms. For sufficiently small kinetic term, LEA is an applicable assumption. The two formulations for a given transport problem are easily comparable because they consist of the same variables. The simulation results presented in this chapter demonstrate that dimensionless prefix dominator (P_D) and reaction transport parameters

such as *Pe*, *Da* and γ conveniently determine the criteria for applicability of LEA diagenesis models. Knowledge of rate laws and rate constants as well as information on the physical transport parameters and boundary conditions are required to evaluate the dimensionless parameters for a given problem. It is concluded that kinetic data are necessary in order to make an appropriate choice of model, LEA or kinetic based for simulating transport under a given set of conditions.

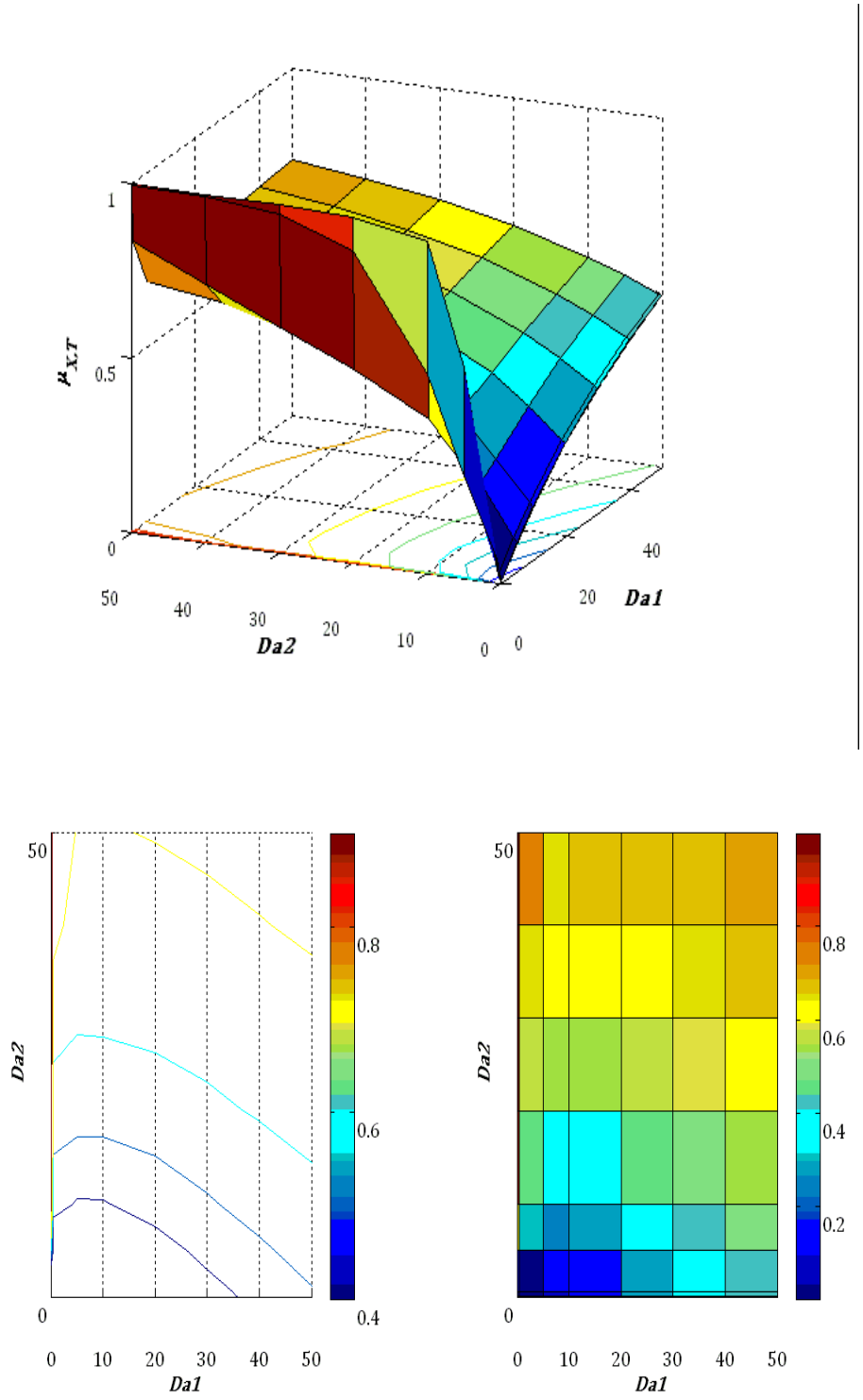

Figure 2-6: 3-D and 2-D presentation of E_L values as a function of *Da*1 and *Da*2.

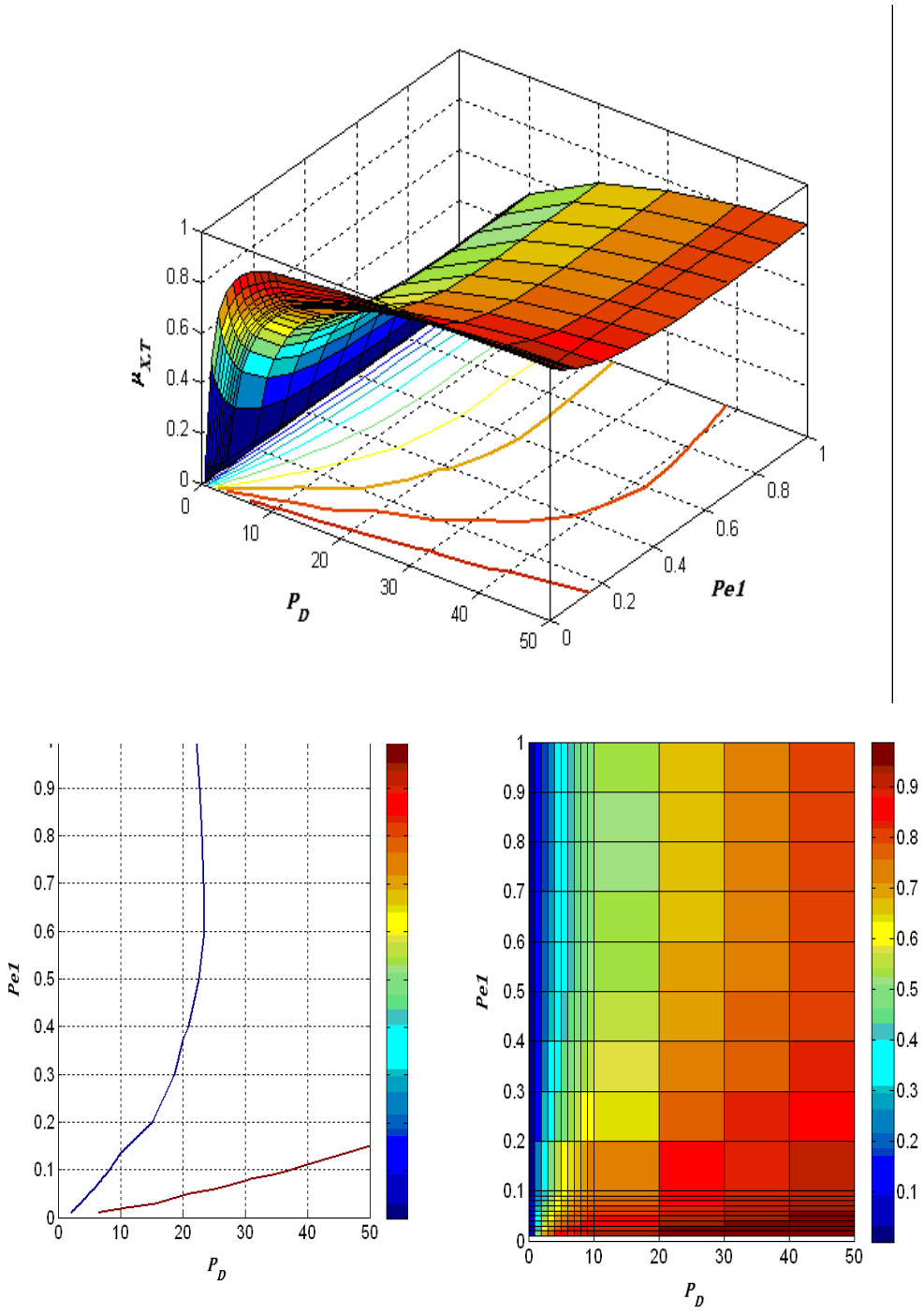

Figure 2-7: 3-D and 2-D presentation of E_L values as a function of $Pe1$ and P_D.

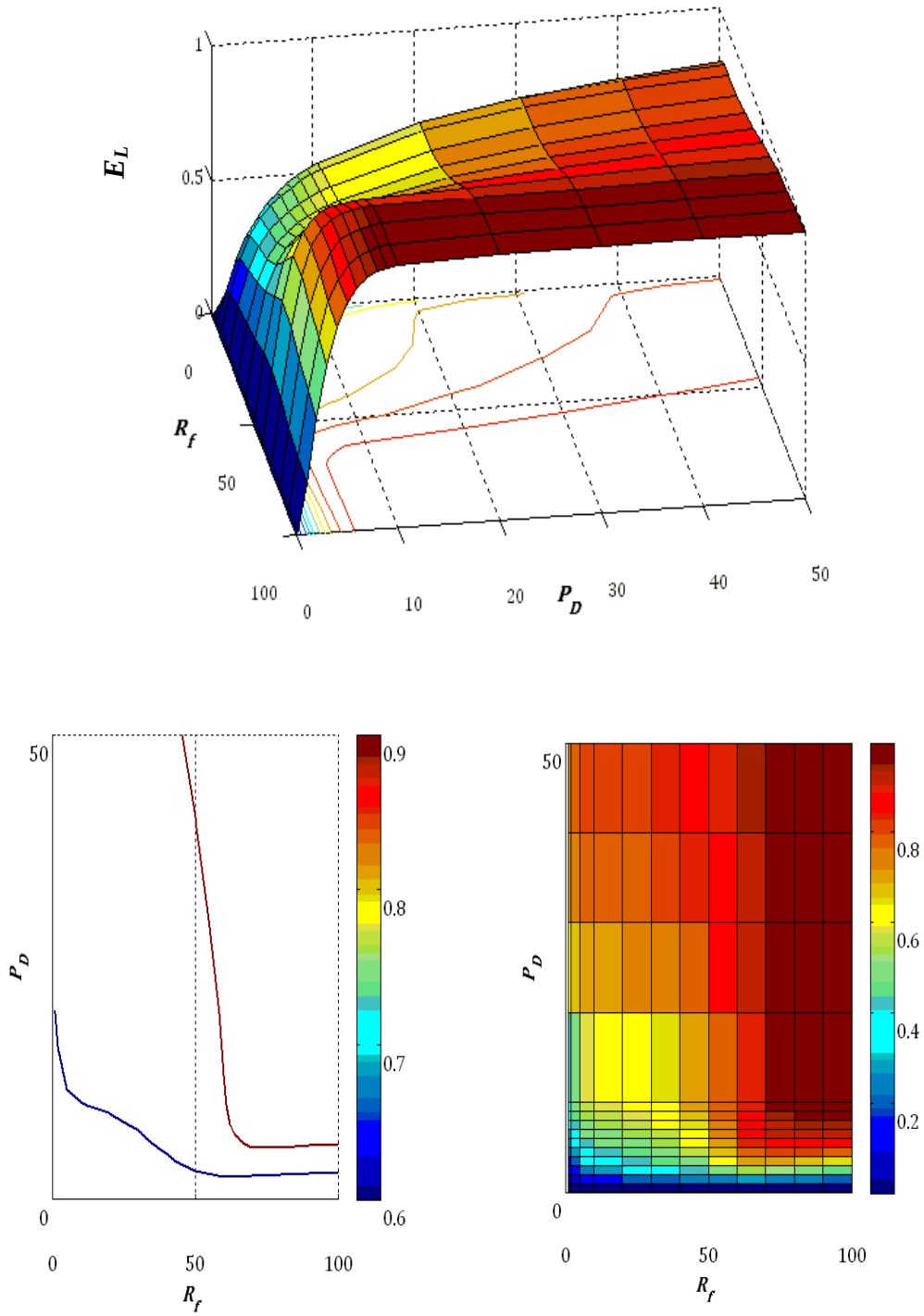

Figure 2-8: 3-D and 2-D presentation of E_L values as a function of R_f and P_D.

CHAPTER 3: A MULTI-COMPONENT, NON-STEADY STATE BIOGEOCHEMICAL SIMULATION MODULE OF EARLY DIAGENESIS IN MATLAB®

3.1 Introduction

Reactive transport models (RTMs) are used to simulate and analyze the dynamic coupling of transport and transformation processes in a variety of environments, both natural and engineered. In particular, RTMs have been applied with great success in the field of early diagenesis in aquatic sediments (Berner, 1980; Boudreau, 1997; Meysman et al., 2003a; VanCappellen and Gaillard, 1996). RTMs of aquatic sediments have reached high levels of sophistication in the representation of the complex reaction networks that drive early diagenetic element cycling and redox dynamics (Katsev et al., 2004; Luff et al., 2001; Meysman et al., 2003b; Regnier et al., 2003; Schulz and Kohler, 2006; VanCappellen and Gaillard, 1996). Through the continuous integration of new observational and theoretical advances, sediment RTMs have remained abreast of advances in biogeochemistry and transport theory. In addition to the quantitative interpretation of pore water and solid sediment data, these RTMs provide powerful tools to identify gaps in our conceptual understanding of the functioning of aquatic sediments,

assess uncertainties in model structure and parameter values, and predict the response of benthic processes to changes in external forcings.

Nevertheless, the potential of early diagenetic RTMs is not yet exploited to its fullest extent. In part, this is because current RTMs tend to be problem- and site-specific (Meysman et al., 2003b). Adaptation of RTMs generated in traditional programming languages, such as FORTRAN or C++, often requires time-consuming rewriting and compilation of the source codes, which restricts their accessibility to many potential users. As a consequence, a number of research groups have made efforts to develop more flexible and user-friendly computer codes for early diagenesis (Meysman et al., 2003a, b; Regnier et al., 2003; Schulz and Kohler, 2006). A relatively recent trend in this area is the use of high-level programming software packages, such as Mathematica®, MATLAB® or MAPLE®. These interactive programming environments provide flexible platforms in which an individual user can easily develop, adapt, test and manage models. By avoiding the hurdles of traditional programming languages, the user can focus on the definition and performance of her model, rather than on the technicalities of writing code. Because the new programming environments provide many visualization capabilities, the graphical analysis of the results is also greatly facilitated and enhanced.

The RTM code BRNS (Biogeochemical Reaction Network Simulator) stands out because of its flexibility and generality (Regnier et al., 2003). It is based on the symbolic programming language MAPLE and offers a modeling framework within which a large number of reactive transport systems can be quantitatively described and interfaced with relevant processes by means of an expandable, web-distributed Knowledge Base (KB) of process equations and parameters. The user builds her own model application in a

MAPLE template. The template is sent to an automatic code generator (ACG), which in turn generates an executable FORTRAN code on the home server. The server returns the executable file to the user who can run it on her personal computer. While the BRNS-KB-ACG offers an efficient and adaptive platform for early diagenetic applications, it requires sustained institutional support to periodically upgrade the KB, maintain the server and provide trouble-shooting.

As an intermediate approach, we present a one-dimensional (1-D) early diagenetic module developed in MATLAB. The module, MATSEDLAB, provides templates for representing the reaction network, boundary conditions and transport regime, which the user can then modify to fit the particular early diagenetic model configuration of interest. In contrast to BRNS, MATSEDLAB is not designed to anticipate all possible combinations of reactions, transport processes and boundary conditions, but rather lets the user expand on existing early diagenetic scripts. The approach is therefore accessible to any user with a basic working knowledge of MATLAB. The choice of MATLAB over other mathematical software packages reflects its prevalence in the biogeosciences community. As an interactive programming environment, MATLAB provides a range of tools for solving systems of coupled differential equations. In particular, the module presented here relies on the computationally efficient MATLAB *pdepe* solver, which allows complex early diagenetic scenarios to be simulated and analyzed on a personal computer.

Somewhat surprisingly, few existing early diagenetic models have been developed in MATLAB. A MATLAB solver for calculating pH distributions in marine systems has been developed (Luff et al., 2001). In related research areas, however,

MATLAB-based biogeochemical models are more common. For instance, an ecosystem model computes the flows of carbon along a food web (Kumblad et al., 2003), and in another model the transfer of nutrients and contaminants from bulk soil via roots to plants is simulated (Szegedi et al., 2008).

In this chapter, we describe the theoretical background of the model and introduce the MATLAB *pdepe* solver, followed by calibration and validation of the model using data obtained from the sediments of a lake in eastern Canada (Couture et al., 2010a) followed by a number of applications. The latter are used to demonstrate the capabilities of MATSEDLAB, but also to illustrate how to modify existing templates. All the corresponding MATLAB.m files are provided as Supplementary Materials.

3.2 Theory

3.2.1 Diagenetic Equation

The general, one-dimensional continuum representation of coupled mass transport and biogeochemical reaction in aquatic sediments is expressed by a set of PDEs in Equation (2.1). Advection in early diagenetic models corresponds to the bulk displacement of solids or pore water, relative to the adopted reference frame, that is, the SWI: $x = 0$. If there is negligible compaction or externally impressed flow, advection of the pore water equals the burial rate of the solids (Berner, 1964). Examples of environments with externally impressed pore water flow include active submarine seeps or sediments in groundwater-fed lakes.

For solute, the upper boundary condition at $x = 0$ is the bottom water concentration:

$$C(0,t) = C_0(t) \tag{3.1}$$

For solid-bound species, the flux continuity condition is used at $x = 0$:

$$D\frac{\partial C}{\partial x} - \vartheta C = J/F \tag{3.2}$$

where J is the (time-dependent) depositional flux of the given solid-bound species, while ϑ and D are the linear sedimentation rate (w) and bioturbation coefficient (D_b) at the SWI. The conversion factor, F, ensures consistency among the units of J, C, w and D_b. In the scripts provided here the units used are µmol cm^{-2} yr^{-1} (J), µmol g^{-1} (C), cm yr^{-1} (w) and cm^2 yr^{-1} (D_b). As lower boundary condition, zero gradients ($\frac{\partial C}{\partial x} = 0$) are imposed for all solute and solid-bound species.

3.2.2 pdepe Solver

The *pdepe* function of MATLAB is used to solve ordinary differential equations (ODEs) as well as partial differential equations (PDEs). Comparison of the accuracy of classical numerical schemes, including finite difference, shooting and collocation methods, with those of the *pdepe* function when solving 1-D transport-reaction PDEs under steady-state conditions has been done (Yudianto and Xie, 2010). The results show a higher accuracy of the *pdepe* function, especially when using larger grid spacing, as well as shorter computation times when small grid spacing are imposed.

The *pdepe* function is designed to solve initial-boundary value problems (IBVPs) consisting of systems of parabolic and elliptic PDEs in one space variable and time. The numerical method is based on a simple piecewise nonlinear Garlekin/Petrov–Garlekin method with second-order accuracy. The method solves the ODEs resulting from the spatial discretization of the PDEs, using a built-in MATLAB ODE solver to obtain approximate solutions at specified times within a defined time interval. An algorithm has been derived and demonstrated the applicability of the method to a variety of advection–

diffusion and diffusion problems (Skeel and Berzins, 1990). An important attribute of the solver is that the time-step is determined dynamically by MATLAB to insure stability of the integration. However, the user can impose a minimum time step. Spatial discretization is fully user-defined.

At the core of MATSEDLAB is a *pdepe* function formulated to have recognizable flux and source terms. The function is solved within defined temporal ($t_0<t<t_f$) and spatial ($a<x<b$) domains, and implemented under the following general form:

$$c\left(x,t,u,\frac{\partial u}{\partial x}\right)\frac{\partial u}{\partial t}=x^{-m}\frac{\partial}{\partial x}\left(x^{m}f\left(x,t,u,\frac{\partial u}{\partial x}\right)\right)+s\left(x,t,u,\frac{\partial u}{\partial x}\right) \quad (3.3)$$

where vector u contains all the unknown (dependent) variables. In the present case of early diagenetic applications, the latter are typically the concentrations of pore water and solid-bound constituents. The coefficients of the time derivatives are collected in the diagonal matrix c (note that c here does not refer to a concentration). The coupling of the partial derivatives with respect to time is restricted to multiplication by c. The diagonal elements of the c matrix can be either identically zero or positive. On the right hand side of Equation (3.3), the functions f and s – the flux and source terms, respectively – are vector functions, which depend on x, t , u and $\partial u/\partial x$. The general form of the function f differentiates between advective and diffusive flux terms. The integer m relates to the symmetry of the problem, with values of 0, 1, and 2 corresponding to slab, cylindrical, or spherical symmetry, respectively.

To complete the mathematical formulation of the problem in the *pdepe* format, it is necessary to set both initial and boundary conditions. For $t=t_0$, and for all depths x, the initial condition is:

$$u(x,t_0)=u_0(x) \quad (3.4)$$

At the boundaries $x=a$ and $x=b$, the following condition applies:

$$p(x,t,u) + q(x,t)f\left(x,t,u,\frac{\partial u}{\partial x}\right) = 0 \tag{3.5}$$

where f is the flux-vector from Equation (3.3). As can be seen from Equations (3.4) and (3.5), the initial conditions are depth dependent while the boundary conditions can also be time dependent. The commonly used formulations for boundary conditions, such as Dirichlet, Neumann and Cauchy/Robin are imbedded in Equation (3.5) and can be selected by the user (see Table 3.1). Note that, when using *pdepe*, the dependent variables included in vector u may be assigned different types of boundary conditions.

To use the *pdepe* function for solving early diagenetic problems, the diagenetic equation (Equation 1.1) is expressed in the form of Equation (3.3). The corresponding matrices become:

$$f\left(x,t,u,\frac{\partial u}{\partial x}\right) = D\frac{\partial(\varepsilon C_i)}{\partial x} - \vartheta\varepsilon C_i \qquad i=1,2,..,L \tag{3.6}$$

and

$$s\left(x,t,u,\frac{\partial u}{\partial x}\right) = \varepsilon\sum r_j \tag{3.7}$$

As x corresponds to the distance along the vertical direction below the SWI, the integer m (see Equation 1.1) is 0. The term f in Equation (3.6) represents the total flux of constituent i; it encompasses sediment burial (advection rate ϑ), molecular diffusion (diffusion coefficient D) and sediment mixing by benthic organisms (bioturbation coefficient D_b). In Equation (3.7), the term s accounts for the net production or consumption of the given chemical species by (bio)geochemical reactions and, for solutes, also non-local bioirrigation. The *pdepe* format offers great flexibility in the modeling of early diagenetic processes. Depth- and time-dependent transport intensities and reaction kinetics, as well as transient boundary conditions, can easily be implemented

Table 3-1: Implementation of different types of boundary conditions using *pdepe*. The flux matrix is composed of advection and diffusion terms i.e. $f = D\frac{\partial u}{\partial x} - vu$ where u is the concentration of the species, v is the advection rate, D is the diffusion coefficient and J is flux term at the boundary. For simplicity, a single unknown variable *u*, rather than an array of unknowns, is considered here.

Type	Formula	p	q
Dirichlet	$u = u_1$	$u - u_1$	0
Neumann	$\frac{\partial u}{\partial x} = J$	$vu - JD$	1
Cauchy or Rubin	$D\frac{\partial u}{\partial x} - vu = J$	$-J$	1

through Equations (3.4) to (3.7).

3.3 Using And Modifying MATSEDLAB

MATSEDLAB was developed in MATLAB 7.6 (release R2008a) and tested up to release R2011b. The program structure is shown in Figure 3.1. The early diagenetic configuration being simulated is defined in MATLAB script *MATSEDLAB_00.m* (this file is associate with *shafei_babak_201212_phd_matsedlab_00.pdf* and the user has to create the MATLAB .m using the .pdf file. The same approach has to be applied for the rest of the MATSEDLAB files. See the Appendix 1). It is in this script that the user specifies the model parameters, such as rate constants or diffusion coefficients. A simulation is initiated by executing the *MATSEDLAB_00.m* script. The example *MATSEDLAB_00.m* script provided in the Supplementary Materials, corresponds to the non-steady state early diagenetic model for C, Fe, S and As in a lake sediments which will be discussed in detail in "Calibration of MATSEDLAB" section.

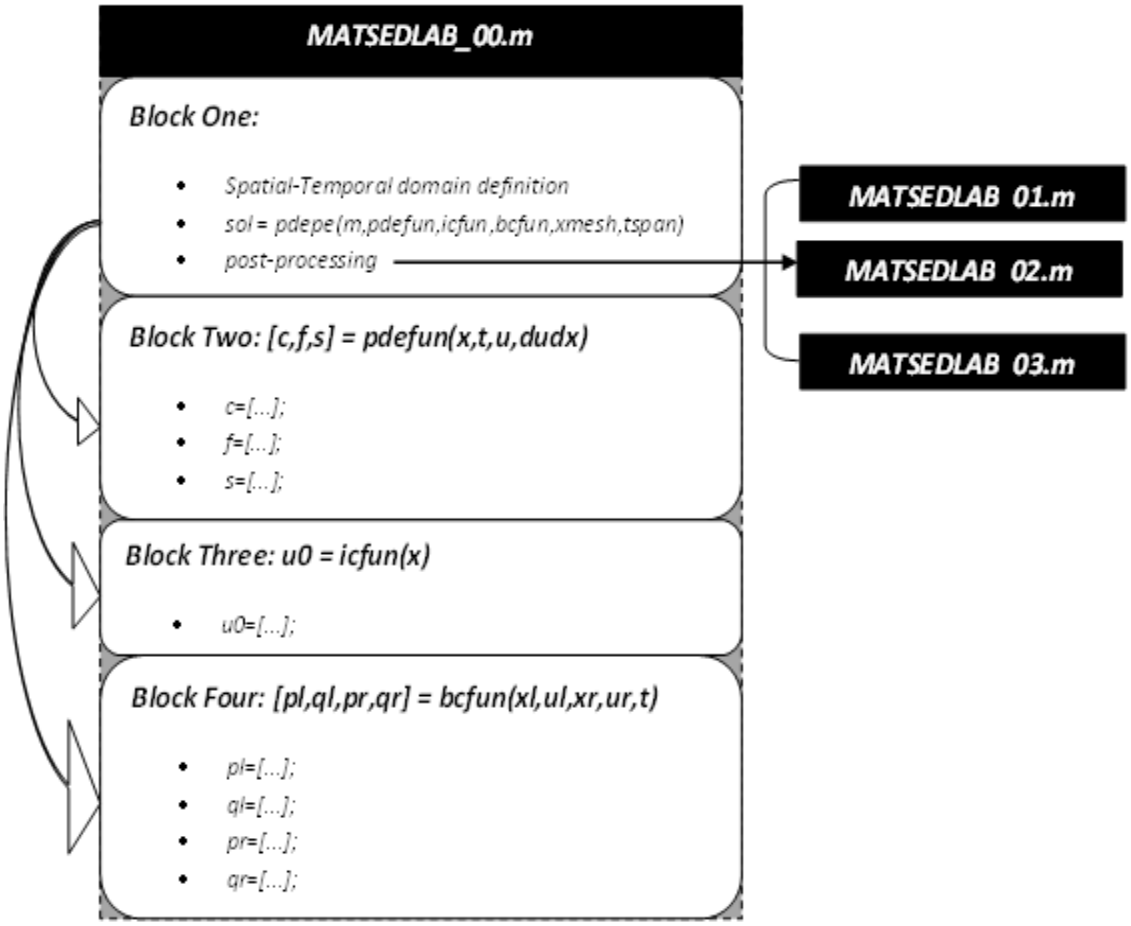

Figure 3-1: Structure of the MATSEDLAB code. The MATLAB.m files comprising the code are denoted in black textboxes, while the subsections, or blocks, of the controlling script *main.m* are denoted in white textboxes.

The prospective user is encouraged to examine and run the *MATSEDLAB_00.m* script supplied in the Supplementary Materials, and to read the MATSEDLAB Getting Started Guide provided in Appendix 1 before starting to modify it to fit the particular early diagenetic system of interest. In *MATSEDLAB_00.m*, the comment 'USER DEFINED' identifies attributes that the user can adapt in a fairly straightforward manner. These include switches to select between alternative model formulations, for example between steady-state and non-steady-state conditions, or constant and depth-dependent porosity distributions.

The first part of the script (*Block One*, Figure 3.1) configures the spatial and temporal domains through the definition of the vectors *x* and *t*. By using *x = linspace (a,b,xres)*, the user generates *xres* equally spaced grid points within the spatial domain [*a, b*]; similarly, the time span [*t0, tf*] is divided in *tres* intervals by defining the vector *t = linspace (t0,tf,tres)*. Once the spatial and temporal domains are specified, the code can be run. The *pdepe* solver and its input functions are automatically called via the command *sol = pdepe(m,pdefun,icfun,bcfun,xmesh,tspan)*, where *pdefun, icfun* and *bcfun* correspond to the three other blocks within *MATSEDLAB_00.m*, and *xmesh* and *tspan* are the depth and time steps that have been defined by the *x* and *t* vectors.

3.3.1 Reaction Network

Adaptation of the MATSEDLAB module to a new early diagenetic application will more often than not require the user to modify the reaction network and the set of chemical species. Therefore, we first describe how reactions are included in MATSEDLAB and then illustrate how a new reaction can be added. The function *pdefun* in *Block Two* (Figure 3.1) defines the transport and reaction components in the set of

diagenetic equations. The matrixes *c*, *f* and *s* (see Equation 3.3) are defined within this block. If the total number of species considered is *L*, with *S* pore water solutes and (*L*-*S*) solid-bound species, and if, for the purpose of this illustration, we keep the porosity constant, the matrices are given by:

$$c = \{ones(S,1); ones(L-S,1)\}_{L\times 1}, \tag{3.8}$$

$$f = \begin{Bmatrix} \begin{pmatrix} (D_b + \varphi D_1)\left(\frac{\partial u_1}{\partial x}\right) - (w+V)u_1 \\ (D_b + \varphi D_2)\left(\frac{\partial u_2}{\partial x}\right) - (w+V)u_2 \\ \vdots \\ (D_b + \varphi D_S)\left(\frac{\partial u_S}{\partial x}\right) - (w+V)u_S \end{pmatrix}_{S\times 1} \\ \begin{pmatrix} D_b\left(\frac{\partial u_{S+1}}{\partial x}\right) - wu_{S+1} \\ D_b\left(\frac{\partial u_{S+2}}{\partial x}\right) - wu_{S+2} \\ \vdots \\ D_b\left(\frac{\partial u_L}{\partial x}\right) - wu_L \end{pmatrix}_{(L-S)\times 1} \end{Bmatrix}_{L\times 1} \tag{3.9}$$

and

$$s = \begin{Bmatrix} \begin{pmatrix} [\alpha_x(u_{1,0} - u_1) + \sum r_1] \\ [\alpha_x(u_{2,0} - u_2) + \sum r_2] \\ \vdots \\ [\alpha_x(u_{S,0} - u_S) + \sum r_S] \end{pmatrix}_{S\times 1} \\ \begin{pmatrix} \sum r_{S+1} \\ \sum r_{S+2} \\ \vdots \\ \sum r_L \end{pmatrix}_{(L-S)\times 1} \end{Bmatrix}_{L\times 1} \tag{3.10}$$

where the function *ones* in Equation (3.8) creates an array with all elements equal to one, and $u_{i,0}$ is the concentration of solute i at the SWI; u_i and du_i/dx are the MATLAB notations used to design the numerical solution u and its derivative with respect to x. In Equation (3.10), the bioirrigation source term is explicitly shown (α_x is the irrigation coefficient at depth x), that is, $\sum r_i$ in this equation only contains the (bio)geochemical reaction rates.

3.3.2 Initial Conditions

In the baseline script *MATSEDLAB_00.m*, the initial concentrations of all the species are set equal to zero. However, it is possible to specify non-zero, depth-dependent initial distributions for dissolved and solid-bound species using the *icfun* function in *Block Three* of the *MATSEDLAB_00.m* script. The function has the form *u = icfun(x)*, which returns initial values of all the chemical species at depth *x* in the column vector *u*. The user may thus specify any set of initial depth profiles, including spatially heterogeneous ones.

3.3.3 Boundary Conditions

The boundary conditions are defined by *bcfun*, in *Block Four* of *MATSEDLAB-_00.m*. The function has the form [*pl*,*ql*,*pr*,*qr*] = *bcfun*(*xl*,*ul*,*xr*,*ur*,*t*), where *ul* is the numerical solution at the upper boundary, *xl = a*, and *ur* that at the lower boundary, *xr = b*. In order to formulate the boundary conditions (Equations 3.1 and 3.2) using the *pdepe* formulation (Equation 3.5) the column vectors *pl* and *ql* (at *xl*), and *pr* and *qr* (at *xr*) need to be defined (see Table 3.1). Using Dirichlet and Cauchy/Robin boundary conditions for the solutes and solid-bound species at the upper boundary, respectively, and zero gradient Neumann conditions at the lower boundary for all the species, we have:

$$pr = \begin{Bmatrix} \begin{pmatrix} (w+V)u_1 \\ (w+V)u_2 \\ . \\ . \\ . \\ (w+V)u_S \end{pmatrix}_{S\times 1} \\ \begin{pmatrix} wu_{S+1} \\ wu_{S+2} \\ . \\ . \\ . \\ wu_L \end{pmatrix}_{(L-S)\times 1} \end{Bmatrix}_{L\times 1} \quad (3.12)$$

$$ql = [zeros(S,1); ones(L-S,1)] \quad (3.13)$$

$$qr = [ones(L,1)] \quad (3.14)$$

As can be seen, *bcfun* is called with argument *t*, which means the code evaluates the boundary values at each time step. This gives the user the possibility to impose transient boundary conditions. The latter is particularly useful when simulating the fate of compounds whose inputs are changing due to, for example, anthropogenic activity, or when dealing with systems where the bottom water chemistry varies over time. The baseline *MATSEDLAB_00.m* script uses non-steady state boundary conditions for the concentration of sulphate and the deposition flux of arsenic at the SWI, while imposing time-invariant boundary conditions for all other chemical species.

3.3.4 Porosity

Matrices (3.8)-(3.14) can be modified to account for depth-dependent porosity. The baseline *MATSEDLAB_00.m* script contains two sets of matrices, one corresponding to a constant porosity distribution, the other to an exponentially decreasing porosity given by $\varphi(x) = 0.9\exp(-0.2x)$, where *x* is depth below the SWI in cm. In the baseline script, the depth-variable porosity matrices are commented out, but the user can switch to them by

commenting out the constant porosity set of matrices. The porosity depth distribution can obviously also be changed by the user.

3.3.5 Post-processing

Several *post-processing* steps are called automatically within *MATSEDLAB_00.m* in order to facilitate the treatment and display of the results. The *pdepe* solver returns the solution as the multidimensional array *sol*, where u_i = *sol(:,:,i)* contains the concentrations of chemical species *i*. The element u_i*(j,k)* = *sol(j,k,i)* represents the numerical solution u_i at *(t,x)= (tspan(j),xmesh(k))*. *MATSEDLAB_01.m* transfers the concentration values at each time and depth into a Microsoft Excel® file and saves it as 'simulation_results.xls' in the current directory. This file is useful to examine individual concentration depth profiles at given time points during a transient simulation, but it is not used later on by MATSEDLAB for plotting purposes.

MATSEDLAB has the built-in capability for plotting model-computed concentration depth profiles of the pore water and solid-bound chemical species against measured values. The user must save an Excel® file named 'FIELD_DATA.xls' containing the measured concentrations and depths in the *MATSEDLAB_02.m* working directory. This file should consist of *L* individual worksheets, each corresponding to one of the chemical species in the same order as in MATSEDLAB. At the end of a simulation, the script *MATSEDLAB_03.m* will then automatically produce depth-concentration plots on which measured concentrations are displayed together with the computed profiles, in addition it will create a series of associated figures in the working directory. In case field data are not available for a given species, the corresponding Excel® worksheet should be left blank and only the model-computed profiles will be

plotted. The post-processing capabilities are further illustrated in the applications presented in the next section.

3.4 Calibration Of MATSEDLAB

As starting point we applied MATSEDLAB to describe the non-steady state dynamics of arsenic and major redox elements in water-saturated sediments of Lake Tantaré (47°04'15"N, 71°33'42"W) a headwater oligotrophic lake located in an ecological reserve, 38 km northwest of Québe that has experienced variations in atmospheric deposition of As and SO_4^{2-} over the last century. The aim of this work was to study sedimentary cycle of arsenic coupled with the cycles of other elements, in particular iron (Fe) and sulfur (S) (O'day et al., 2004) and to predict Arsenic (As) release from lake sediments under non-steady state conditions.

In the proposed conceptual model, ferric iron oxyhydroxides and iron sulfides are considered as the main carrier phase of the arsenic in the oxic and anoxic zones of the sediments respectively. Reducing conditions in sediments may cause the dissolution of the Fe(III) oxyhydroxides, thereby releasing As to the pore water (Root et al., 2007). Retention of As within the sediment occurs when upward migrating dissolved As is adsorbed on authigenic Fe(III) oxyhydroxides (Belzile and Tessier, 1990). Dissolved As may also migrate downwards into more reducing zones, where it is immobilized, via As binding to authigenic Fe sulfide minerals(Bostick et al., 2004; O'day et al., 2004).

3.4.1 Model Formulation And Reaction Network

Model development followed the general approach outlined in the literature (VanCappellen and Wang, 1996). Mathematically, a set of partial differential equations (PDEs) defined a coupled transport-reaction system in which all the reactions were

described by kinetic expressions; 13 reaction pathways and 11 chemical species are considered (Table 3.2). Briefly, the reaction network included three primary redox reactions describing the degradation of OM via oxic respiration (R1), dissimilatory iron reduction (R2), and sulfate reduction (R3) (Table 3.2). Nitrate reduction was not considered, because of the low values and poor precision of the NO_3^- concentration measurements. Manganese (Mn) oxyhydroxides were similarly excluded as potential electron acceptor, because neither the solid-phase nor the pore water Mn profiles showed evidence for significant Mn redox cycling Lake Tantaré (Couture et al., 2010b). An exponential decay function was imposed to describe the depth-dependent rate of total OM degradation, based on the mineralization rates measured in the sediment slurries. Consumption of a given terminal electron acceptor (TEA = O_2, $Fe(OH)_{3(s)}$ and SO_4^{2-}) is coupled to the rate of OM oxidation through a Monod kinetic dependency on the TEA concentration, and an inhibition term limiting the rate of a respiratory pathway in the presence of stronger oxidants.

The secondary redox reactions considered were the oxidation of pore water Fe(II) by O_2, and of H_2S by O_2 and $Fe(OH)_{3(s)}$ (R4, R5 and R6, respectively; Table 3.2). Bimolecular reaction rate laws were used for these reactions, thereby restricting their occurrence to depth intervals where both oxidant and reductant were present at non-zero concentrations. The rates of precipitation and dissolution of $FeS_{(s)}$ (R7 and R−7, respectively) were explicitly dependent on the corresponding pore water saturation state. The rate of $FeS_{2(s)}$ precipitation (R8) was assumed to be proportional to the concentrations of pore water H_2S and of solid phase $FeS_{(s)}$, and the rate of diagenetic

sulfidization of sediment OM (R9) was assumed to depend on the concentrations of OM and pore water H_2S (Dale et al., 2009).

Sorption of As to $Fe(OH)_{3(s)}$ (R10) and $FeS_{(s)}$ (R11) were treated as irreversible processes. Remobilization of sorbed As required the dissolution of $Fe(OH)_{3(s)}$ (R12) and $FeS_{(s)}$ (R13), whereby stoichiometric release of the solid-bound As was assumed (Table 3.2). Formation of pure As oxides, As sulfides and metal arsenates were not considered, because the pore waters remained undersaturated with respect to these mineral phases by several orders of magnitude.

The model did not explicitly account for depth variations in [As] speciation; according to thermodynamic calculations > 99% of [As] should be in the form of $As(OH)_3^0$. The transport processes included in the one-dimensional conservation equations were molecular diffusion, bioirrigation, bioturbation and sediment accumulation. α was assumed to decrease exponentially from a fixed boundary value at the sediment water interface (SWI) ($\alpha_0 = 4.58\times10^{-7}$ s^{-1}) to zero at 10 cm depth, since no benthic animals were found below this depth in the sediments. The measured near-constant porosity, from the SWI to 30 cm depth, of 0.970 ± 0.002 was used in the calculations. Zero concentration gradients were used as lower boundary condition for all solutes and solids. An average deposition flux of reactive Fe oxyhydroxides ($J^{Fe(OH)_3}$ = 6.7 μmol cm^{-2} yr^{-1}) was imposed as upper boundary value at the SWI. The measured water column concentrations of solutes, except that of [SO_4^{2-}], were also imposed as upper boundary values at the SWI. Time-dependent variation in water column [SO_4^{2-}] was assumed to parallel the increasing sulfate deposition from 1940 until the mid 1980's and the subsequent drop since then, which has been reported for lakes from eastern North

America [*29*]. Accordingly, the variation over time (t) in [SO_4^{2-}] at the SWI (y^{SO_4}) was described by the following bell function (Matisoff and Holdren, 1995):

$$y^{SO_4} = y_0^{SO_4} + a.e^{\left[-0.5\left(\frac{t-t_{max}}{b}\right)\right]^2} \quad (3.15)$$

where $y_0^{SO_4}$ (10 μM) is the pre-industrial lake water [SO_4^{2-}], t_{max} (1985) is the year of peak SO_4^{2-} atmospheric deposition, a (60 μM) defines the maximum [SO_4^{2-}] at t_{max} and b defines the width of the peak (~ 60 years). The variation in particulate As deposition flux at the SWI (J_{dep}^{As}) was also described by Equation (3.15), replacing y^{SO_4} and $y_0^{SO_4}$ by J_{dep}^{As} and $J_{dep,0}^{As}$, respectively. The values of t_{max} (1950), a (2.5 nmol cm^{-2} yr^{-1}) and b (8 yr) were calculated by assuming that J_{dep}^{As} parallels the historical trend in atmospheric As during the last century, as reconstructed by (Couture et al., 2008) through inverse modeling of {As} and [As] profiles measured in an adjacent, seasonally anoxic basin of Lake Tantaré. The value of $J_{dep,0}^{As}$ (2.1 nmol cm^{-2} yr^{-1}) is the estimated background flux of As deposited at the SWI of the site. The transient boundary conditions for [SO_4^{2-}] and As deposition are shown in Figures 3.2. g and h.

3.4.2 Results And Discussion

The rate of OM mineralization decreased exponentially over depth. Pore water O_2 was depleted within the uppermost 0.5 cm of sediment (Figure 3.2a). Pore water concentrations of dissolved Fe(II) and As were higher than those in the overlying water (Figures 3.2b and e). Pore water SO_4^{2-} concentrations decreased with depth below the SWI, whereas ΣS(−II), which near of below detection in the overlying water, increased below 2–6 cm sediment depth (Figures 3.2c and d). Solid-phase As

Table 3-2: Reaction network and kinetic formulations used in the model.

Description	Reaction	Kinetic formulation	I.D.
Aerobic respiration	$CH_2O + O_2 \rightarrow CO_2 + H_2O$	Rc f_{O2} accel	R1
Fe oxide reduction	$CH_2O + 4Fe(OH)_{3(s)} + 7CO_2 + H_2O \rightarrow 4Fe(II) + 8HCO_3^- + 3H_2O$	Rc $f_{Fe(OH)3}$	R2
Sulfate reduction	$2CH_2O + SO_4^{2-} \rightarrow H_2S + 2HCO_3^-$	Rc f_{SO4}	R3
Fe(II) oxidation by O_2	$Fe(II) + 0.25O_2 + 2HCO_3^- + 2H_2O \rightarrow Fe(OH)_{3(s)} + 2CO_2$	k_{feox} [Fe(II)] [O_2]	R4
H_2S oxidation by O_2	$H_2S + 2O_2 + 2HCO_3^- \rightarrow SO_4^{2-} + 2CO_2 + 2H_2O$	k_{tsox} $\Sigma(S{-}II)$[a] [O_2]	R5
H_2S oxidation by Fe oxide	$H_2S + 14CO_2 + 8Fe(OH)_{3(s)} \rightarrow 8Fe(II) + SO_4^{2-} + 14HCO_3^- + 6H_2O$	k_{tsfe} $\Sigma(S{-}II)$ {$Fe(OH)_3$ }	R6
$FeS_{(s)}$ dissolution [b]	$FeS_{(s)} + 2H^+ \rightarrow Fe(II) + H_2S$	k_{FeSdis} {FeS} $(1{-}\Omega_{FeS})$	R−7
$FeS_{(s)}$ precipitation	$Fe(II) + H_2S \rightarrow FeS_{(s)} + 2H^+$	k_{FeSpre} $(\Omega_{FeS}{-}1)$	R7
Pyrite precipitation	$FeS_{(s)} + H_2S \rightarrow FeS_{2(s)} + H_2$	k_{pyrpre} {FeS} $\Sigma(S{-}II)$	R8
OM sulfidization	$OM + H_2S \rightarrow$ “OM-H_2S”	k_{Sorg} {OM} $\Sigma(S{-}II)$	R9
As sorption to [$_{(s)}$	$As + Fe(OH)_{3(s)} \rightarrow$ “$Fe(OH)_3$-As”	$k_{adsFeOH}$ [As] {$Fe(OH)_3$}	R10
As sorption to $FeS_{(s)}$	$As + FeS_{(s)} \rightarrow$ “FeS-As”	k_{adsFeS} [As] {FeS}	R11
As release during dissolution of $Fe(OH)_{3(s)}$		{As}:{Fe(OH)3} $(4\times R2 + 8\times R6)$	R12
As release during dissolution of $FeS_{(s)}$		{As}:{FeS} $(R{-}7)$	R13

[a] $\Sigma(S{-}II) = [H_2S] + [HS^-]$ [b] $\Omega_{FeS} = [Fe(II)] \times [H_2S]/[(H^+)]^2 K_{FeS}$

concentration decreased with depth in the upper 2 cm of the sediment, then increased to reach a local maximum at a depth of about 5.5 cm, and decreased again (Figure 3.2h). Figure 3.2f shows that {$Fe(OH)_3$} dropped sharply in the top 2 cm and then decreased more gently below this horizon. A distinctive sub-surface maximum {FeS} was observed at about 5 cm depth (Figure 3.2.g).

Imposing the boundary conditions described above and using the reaction parameters taken from the literature as the initial guesses, the baseline simulation were carried out. The aim was to capture the general features of the observed pore water and solid phase concentration profiles. The parameters derived from the literature, were further adjusted to fit the experimental data while taking into account the parameter ranges reported in the literature, when available (Table 3.3). In preliminary simulations, where reaction R9 was omitted, {FeS} concentrations one were obtained order of magnitude higher than the measured values. Another study, using a similar modeling approach, also over-predicted lake sediment {FeS}(Canavan et al., 2006).

Therefore in order to reproduce the {FeS} profile and the trends in the ΣS(−II) profiles (Figures 3.2d and g), OM sulfidization (R9) must then represent the main sink for sulfide in Lake Tantaré sediment. In the reactive transport model, the [As] and {As} distributions are completely determined by the redox transformations of carbon, oxygen, iron and sulfur, and by the upper boundary conditions for $J_{\mathrm{dep}}^{\mathrm{As}}$ and [SO_4^{2-}]. The predicted [As] profile reflects the post-depositional redistribution of As between the Fe(III) oxyhydroxide and Fe(II) sulfide pools and because of that the shape of the {As} sediment record deviates substantially from that imposed time-dependent As deposition flux

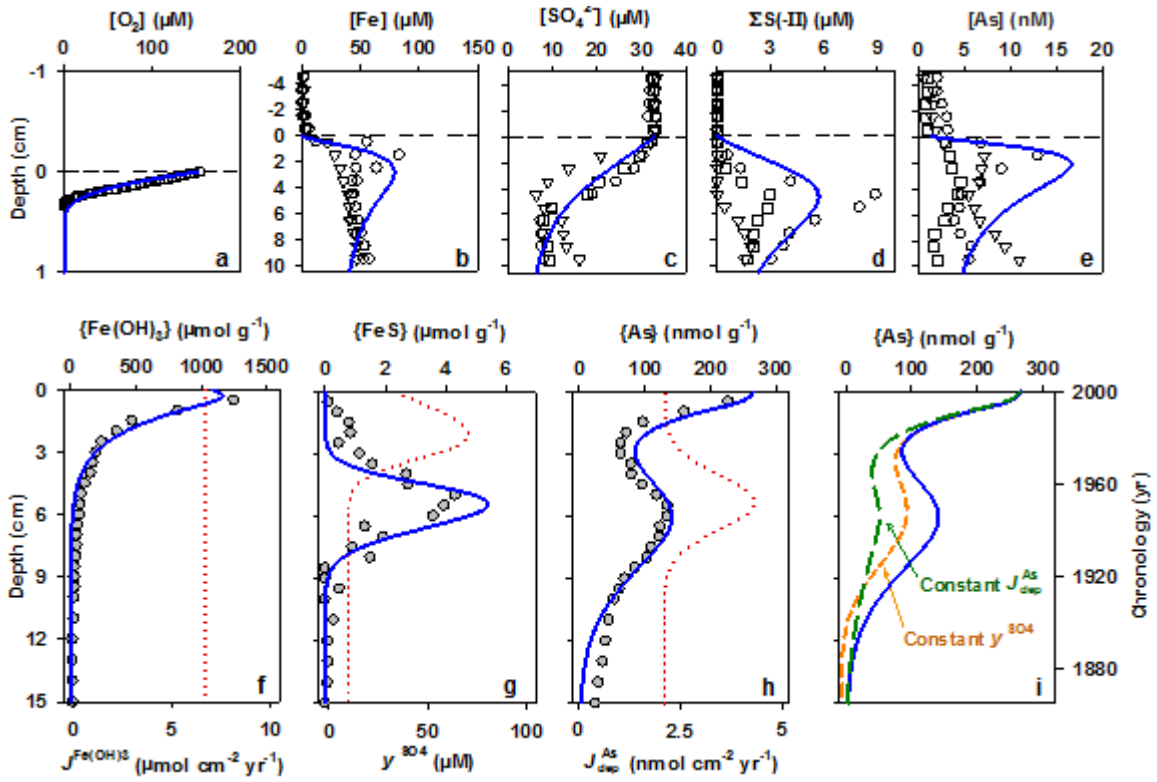

Figure 3-2: Depth profiles of the concentrations of dissolved O_2 and the average concentrations of triplicate porewater measurements of Fe, SO_4^{2-}, ΣS(−II) and As (Panels a to e) measured in July 2003 (open squares), September 2003 (open circles) and August 2004 (open triangles), as well as the concentrations of solid-phase Fe(III) oxyhydroxides, $FeS_{(s)}$ and As (Panels f to g). In Panels a to h the solid line is the model-predicted concentration profile for year 2003 of the baseline simulation. In Panels f to h the dotted lines represent the upper boundary conditions imposed for the deposition flux of $Fe(OH)_{3(s)}$, water column $[SO_4^{2-}]$ and deposition flux of As, respectively. In Panel i, the model-predicted concentration profile using the baseline boundary conditions (solid line) is compared to predicted concentration profiles when keeping either bottom water $[SO_4^{2-}]$ constant at the pre-industrial value of 10 μM (dashed line), or the As deposition flux constant at the pre-industrial value of 2.1 nmol cm^{-2} yr^{-1} (short dashed line).

(Figure 3.2h). The release of As to the pore water just below the SWI is due to the reductive dissolution of the Fe(III)oxyhydroxides (Figure 3.2e), whereas its removal below 2 cm depth is attributed to sorption onto precipitating Fe(II) sulfides. Depth-integrated reaction rates and fluxes (Figure 3.3) from the baseline simulation indicate that about 10% of As currently deposited at the SWI is buried in the form of $FeS_{(s)}$-bound As whereas 75% is transported to the overlying water, suggesting that the remaining 15% of is trapped in the redox loop associated with the $Fe(OH)_{3(s)}$ recycling.

In the baseline simulation, the benthic flux of [As] from the sediment to the water column ($J_{SWI}^{As} = J_{diffusion} + J_{bioirrigation}$) reaches its maximum value 26 yr after the particulate As deposition flux peaked, i.e. in 1976 rather than in 1950 (Figure 3.4a). A noteworthy feature of Figure 3.4a is that, after reaching its peak value, J_{SWI}^{As} drops sharply becoming even lower than the pre-industrial level around the year 2006. This minimum value of J_{SWI}^{As} occurs at the time $\{Fe(OH)_3\}$ reaches a minimum at the SWI (Figure 3.4a) which was unexpected since with low concentrations of $Fe(OH)_3$ the release of As through SWI should be increased.

The decreasing As sorption capacity of Fe(III) oxyhydroxides, however, is offset by the increase in that of $FeS_{(s)}$ (reaction R11). The model further predicts a lag time of about 21 yr between the peak input of SO_4^{2-} to the lake in 1985 and the minimum in As efflux from the sediments.

A sensitivity analysis revealed that J_{SWI}^{As} is most sensitive to parameters that influence the OM degradation rates and the abundance of $Fe(OH)_{3(s)}$. Hence, imposing higher rates of OM degradation increases As release to the overlying water, because of the upward migration of the oxic-anoxic boundary in the sediment and the reduced

availability of Fe(III) oxyhydroxides close to the SWI (Figure 3.4b). Conversely, decreasing the OM degradation rates results in a thicker oxic zone near the SWI and, thus, a greater capacity to trap upward diffusing As by Fe(III) oxyhydroxides, thereby lowering and delaying the dissolved As efflux from the sediment. The complex effects of water column [SO_4^{2-}], another key forcing parameter, on J_{SWI}^{As} are illustrated in Figure 3c. Simulations are provided for pre-industrial [SO_4^{2-}] that have been increased or decreased by a factor of two relative to the baseline scenario. Both case result in generally decrease of the efflux of dissolved As to the overlying lake water, although the departure from the baseline scenario remain relatively small. The higher pre-industrial [SO_4^{2-}] increases As retention in the sediment because of higher $FeS_{(s)}$ production, while the lowering of J_{SWI}^{As} when pre-industrial [SO_4^{2-}] is decreased reflects the increased abundance of ferric iron oxyhydroxides near the SWI, which act as a barrier against upward migrating pore water As. In contrast to the OM degradation rate, variations in lake water [SO_4^{2-}] have no effect on the timing of maximum As release. Overall, $FeS_{(s)}$ formation in Lake Tantaré sediments acts as a buffer against benthic remobilization of anthropogenic As. Once the reactive transport models will have been validated with respect to this new mechanistic and kinetic information, its capacity to quantitatively predict the fate of As, and ultimately other contaminants, under changing environmental conditions (e.g., eutrophication, pollution events) will have been greatly improved.

3.4.3 Sensitivity Analysis

This application, *MATSEDLAB_app_01.m*, is an extension of the reactive transport model simulations of baseline script *MATSEDLAB_00.m*. In *MATSEDLAB_app_01.m*, the sensitivity of the model-computed benthic efflux of dissolved As (J_{As}) to model

parameters is quantitatively evaluated. The sensitivity, *S(x,y)*, of the selected model outcome *x* (= J_{As}) to changes in parameter *y* is defined as (Schauser et al., 2006):

$$S(x,y) = \frac{dx/x}{dy/y} = \frac{dlnx}{dlny} \tag{3.16}$$

A high positive or negative value of *S(x,y)* indicates a highly sensitive parameter. The parameters tested are listed in Table 6 and include the organic matter degradation rate at the SWI (R_C^0), half saturation constants (K_m), inhibition constants (K_{in}), rate coefficients (k), upper boundary conditions and transport parameters. The results of the sensitivity analysis are summarized in Table 3.4: the absolute values of *S(x,y)* range from near zero to 1.59, with R_C^0 being the most sensitive parameter. The latter result is not surprising as the degradation of organic matter is the driving force for most biogeochemical processes in aquatic sediments (e.g., Van Cappellen and Gaillard, 1996). Higher organic matter degradation rates cause the upward migration of the oxic-anoxic boundary and decrease the availability of iron (oxy)hydroxides near the SWI, hence allowing more pore water As to escape to the water column. Other sensitive reaction parameters (*S(x,y)* > ± 0.3) are all linked to the cycling of O_2 and Fe. Among the transport parameters, the bioirrigation coefficient is the most sensitive. The corresponding *S(x,y)* value is negative (-0.57) because increased irrigation deepens the oxic-anoxic boundary and increases the abundance of Fe (oxy)hydroxides, hence resulting in a more efficient retention of As by these mineral phases in the sediment.

3.4.4 Arsenic Sorption: Equilibrium, Kinetic and Mixed Approaches

Sorption reactions are key processes that govern the fate of dissolved contaminant in porous media. Mathematical description of sorption processes often requires a choice between models based on the local equilibrium assumption (LEA) and models involving

reaction kinetics (Bahr and Rubin, 1987; Valocchi, 1985). If sorption reactions proceed instantaneously, i.e., are fast enough with respect to the bulk fluid flow rates, a local chemical equilibrium can be assumed. However, systematically applying LEA to all subsurface environments, such as aquatic sediments and aquifers, regardless of their transport regime may result in erroneous prediction. In the case of aquatic sediments, such as lake bottom sediment, transport phenomena that occur on different timescales include burial of the particles, molecular diffusion of the dissolved constituents, solid and solute transport by bioturbation, and non-local solute transport by bio-irrigation (Boudreau, 1997). These transport processes are different than those prevailing in aquifers, dominated by dissolved species advection, hydrodynamic dispersion and molecular diffusion (Bahr and Rubin, 1987). Hence, the selection of the LEA should be done on a critical basis.

On a microscopic level, sorption processes are often described as multi-step reactions involving both adsorption and coprecipitation reactions, which can be occurred either in sequence or simultaneously. In the physical space, adsorption is a two dimensional process by which an element binds to the planar solid phase surface, while coprecipitaion is a three dimensional process incorporating the element into the bulk-particle structure. Because the formation mechanisms of adsorbed and coprecipitated phase are different, the kinetics of the associated reverse reactions, desorption and dissolution, respectively, differ from each other. In particular, an element that is coprecipitated is less readily released upon changes in the solution composition, such as pH or ionic strength. Therefore, the scope of this section is to address the importance of distinguishing between adsorption and coprecipitation in reactive-transport modeling,

Table 3-3: Reaction parameters used in application 1; Arsenic early diagenesis in lake sediment.

Parameter	Value*	Unit	Description
Rc	$400\times e^{(-0.183x)}$	$\mu mol^{-1}\ cm^{3}\ yr^{-1}$	Rate of organic matter mineralization
accel	25		Acceleration factor for R1
$f_{O2}, f_{Fe(OH)3}, f_{SO4}$	0−1		Fraction of total OM degraded by each pathway
$K_m\ O_2$	4×10^{-3}	$\mu mol\ cm^{-3}$	Half-saturation for oxic respiration, R1
$K_m\ Fe(OH)_3$	2×10^{3}	$\mu mol\ g^{-1}$	Half-saturation for Fe(III) reduction, R2
$K_m\ SO_4$	0.5	$\mu mol\ cm^{-3}$	Half-saturation for SO_4 reduction, R3
$K_{in}\ O_2$	3.2×10^{-6}	$\mu mol\ cm^{-3}$	Inhibition from O_2, R1
$K_{in}\ Fe(OH)_3$	200	$\mu mol\ g^{-1}$	Inhibition from Fe(III), R2
k_{tsox}	1×10^{3}	$cm^{3}\ \mu mol^{-1}\ yr^{-1}$	Rate constant for sulfide oxidation by O_2, R4
k_{feox}	4×10^{4}	$cm^{3}\ \mu mol^{-1}\ yr^{-1}$	Rate constant for Fe(II) oxidation by O_2, R5
k_{tsfe}	2.5	$cm^{3}\ \mu mol^{-1}\ yr^{-1}$	Rate constant for sulfide oxidation by Fe-oxides, R6
K_{FeS}	9.6×10^{3}	μM	FeS stability constant
k_{FeSdis}	1×10^{-3}	yr^{-1}	Rate constant for FeS dissolution, R7
k_{FeSpre}	1.5×10^{3}	$\mu mol\ g^{-1}\ yr^{-1}$	Rate constant for FeS precipitation, R_7
$k_{adsFeOH}$	1.35	$cm^{3}\ \mu mol^{-1}\ yr^{-1}$	Rate constant for As adsorption onto $Fe(OH)_3$, R8
k_{adsFeS}	10	$cm^{3}\ \mu mol^{-1}\ yr^{-1}$	Rate constant for As adsorption onto FeS, R9
k_{Sorg}	4×10^{-2}	$cm^{3}\ \mu mol^{-1}\ yr^{-1}$	Rate constant for sulfidization of organic matter, R10

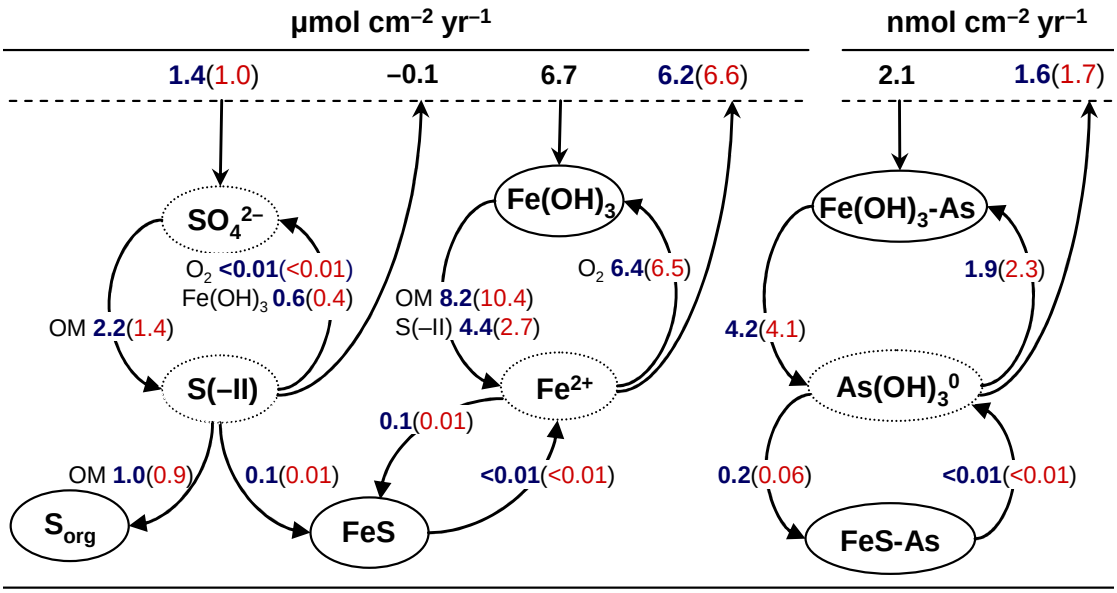

Figure 3-3: Depth-integrated rates and fluxes of the coupled As−Fe−S cycles in the upper 15 cm of the sediment column. The numbers in bold are the values derived for year 2003 of the baseline simulation. The numbers between brackets are the steady state, depth-integrated rates and fluxes when using constant (pre-industrial) water column [SO_4^{2-}] and particulate deposition As flux as upper boundary conditions.

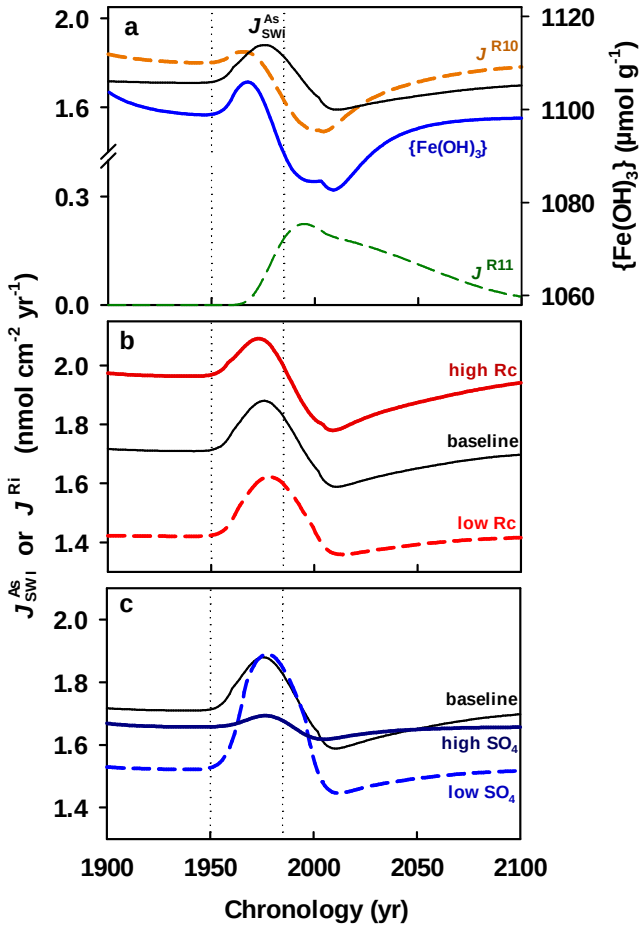

Figure 3-4: Model-predicted efflux of dissolved As from the sediments (J^{As}_{SWI}) as a function of time for the baseline simulation (Panel a), and for scenarios where the rate of organic matter (OM) degradation, *R*c (Panel b) and the sulfate concentration of SO_4^{2-} in the lake bottom water (Panel c) are varied. Also shown in Panel a are the variations in the rate of As sorption to Fe(III) oxyhydroxides (J^{R10}) and to Fe(II) sulfides (J^{R11}), as well as the concentration of Fe(III) oxyhydroxides in the uppermost cm of sediment. The dotted vertical lines represent the dates of maximum As input to the lake (1950) and of maximum water column [SO_4^{2-}] (1985) during these simulations. See text for a description of the variable OM and SO_4^{2-} scenarios.

Table 3-4: Sensitivity of As release rate to changes in the most important parameters.

Parameter	*S(x,y)*
Rc	1.59
K_m O_2	-0.51
K_m $Fe(OH)_3$	-0.39
K_m SO_4	-0.05
K_{in} O_2	0.59
K_{in} $Fe(OH)_3$	0.06
k_{tsox}	2.64E-5
k_{feox}	0.08
k_{tsfe}	0.12
$k_{adsFeOH}$	-0.47
k_{adsFeS}	-6.2E-14
BC_O_2	-0.40
BC_SO_4	0.09
$BC\_Fe(OH)_3$	0.32
w	0.07
α_0	-0.57
D_B	0.03

since this can have a significant effect on the model-predicted release of an element from soils and sediments. The sorption of As will be discussed as an example contaminant.

Ferric iron (oxy)hdroxides are major sorbents of As and often control the mobility of this toxic metalloid in subsurface environments (Belzile and Tessier, 1990; O'day et al., 2004; Root et al., 2007). They are formed in oxygenated aquatic environments and are found as a wide range of minerals, most commonly ferrihydrite (Fe(OH)3), lepidocrocite (FeOOH), goethite (Fe2O3) and hematite (FeX); each having different stability, specific surface area and reactivity. In environment that becomes reducing, due for instance to the

microbially-mediated oxidation of organic matter, Fe (oxy)hydroxides will undergo reductive dissolution, hence releasing both ferrous iron (Fe(II)) and dissolved As. Under sulfate-reducing conditions, aqueous sulfide may form iron sulfide phases, such as mackinawite (FeS), troilite (FeS) and pyrite (FeS2;). Binding to iron sulfides have been shown to control As sequestration in anoxic sediments (Wolthers et al., 2005) and may further represents the main sedimentary sink as well as act as a buffer against benthic remobilization of As to the water column (Couture et al., 2010b).

Despite the numerous studies that have investigates the mechanism responsible for the bonding of As onto Fe(III) (oxy)hydroxides, very few have specifically studied coprecipitation, during which the precipitation of ferrihydrite and adsorption of As simultaneously occur. Yet, this is likely to occur in many natural subsurface environment and remediation scenario. Indeed, co-precipitation and adsorption have been shown to occur simultaneously in a range of geochemical conditions. Arsenic uptake in artificial, organic matter-free groundwater containing competing anions such as carbonates and phosphates has been systematically investigated (Sahai et al., 2007). It is shown that even though natural attenuation of As by adsorption onto Fe(III) oxyhydroxides may be limited by competition from other oxyanions, uptake by coprecipitation can locally sequester As. X-ray diffraction has been used to investigate sorption of As(V) at low concentrations in the presence of ferrihydrite at pH 5 and 7 (Tokoro et al., 2010). The result show that As is primarily adsorbed when the molar As:Fe ratio is <0.4, while it is instead coprecipitated when the molar As:Fe ratio was >0.4. At pH <8, As is initially sequestered by Fe(III) (oxy)hydroxides through adsorption, shown by surface complexation modeling, then form coprecipitated ferric arsenate (Jia et al., 2006). A

similar pathway, from adsorption to coprecipitation has been delineated as As sorption proceed through inner-sphere complexation via ligand exchange, followed by the formation of an inner-sphere surface complexes between As oxyanions and metal oxides (Fendorf et al., 1997; Manning et al., 1998). These complexes were shown to be mononuclear monodentate, mononuclear bidentate and binuclear bidentate, as a function of As concentration in the aqueous phase.

A similar conclusion have been reached with respect to As sorption onto Fe(II) sulfides, as it has been shown that As(III) adsorption onto troilite is followed by co-precipitation of a arsenopyritelike mineral (Bostick and Fendorf, 2003). Together, these studies reveal that the solid-phase As resulting from interaction of dissolved As with Fe minerals must be considered as both irreversibly coprecipitated and reversibly-adsorbed. According to the previously mentioned studies, the specific geochemical conditions leading to either one dominating the solid phase As pool are not well constrained. Indeed, it is difficult to distinguish between these two processes using solely laboratory experiments.

Here, we conduct a quantitative investigation, using reactive-transport modeling, of the mechanisms by which dissolved As is sorbed to Fe(III) (oxy)hydroxides) and Fe(II) sulfides in the subsurface. Adsorption and coprecipitation are considered as distinct pathways for As to sorb onto two relevant mineral phases: ferrihydrite ($Fe(OH)_3$) and mackinawite (FeS). These mineral phases were chosen due to their environmental relevance and to availability of literature data for As sorption.

3.4.4.1. Conceptual Model

Here the sequestration of As in Fe-rich porous media is assumed to proceed through both adsorption and co-precipitation. These processes can occur either separately or collectively in the porous media. In the latter cases two broad classes of sequestration mechanisms during with both adsorption and coprecipitation occur: simultaneous mechanisms or sequential mechanisms.

The simultaneous occurrence of adsorption and coprecipitation reflect the cases when As is incorporated within the mineral structure during the formation of a main carrier phase such as Fe (oxy) hydroxides. In contrast, the sequential occurrence of these two pathways considers the cases when three dimensional growth of As on the surface of the sorbent is in continuation of surface complexation. It is the cases in most experiments when As is added to Fe mineral suspensions(Fendorf et al., 1997; Jia et al., 2006; Tokoro et al., 2010), or in field studies where groundwater flows through Fe-rich porous media (Jung et al., 2009). These pathways of As sequestration are schematized in Figure 3.5.

To embody these pathways in a reactive transport model, they have first to be mathematically represented. Base on the large body of evidence demonstrating that adsorption reaction are generally fast, we assumed adsorption reactions are satisfying the LEA. On the other hand, copee3rcipitation is more reasonably treated as a slow, kinetically controlled reaction. The equilibrium treatment of adsorption and the kinetic treatment of coprecipitation is the pivotal point in the mathematical formulation of As sequestration in our work.

To sum up, formulation of the pathways for As sorption fall into the following 4 modeling approaches: 1) fully kinetic (i.e., only coprecipitaion), 2) fully equilibrium (i.e.,

only adsorption), 3) concurrent mixed kinetic-equilibrium (simultaneous adsorption and coprecipitation), and 4) consecutive mixed kinetic-equilibrium (sequential adsorption and coprecipitation). In our model, dissolution and desorption can occur simultaneously, or sequentially. Adsorption being a reversible reaction, changes in the geochemical conditions of the aqueous phase will release As. Since we assume that LEA is satisfied for As adsorption, the same goes for desorption and therefore dissolved and adsorbed As will be at equilibrium at any given time.

On the other hand, dissolution is likely to be responsible for As release under acidic or reducing conditions where Fe (oxy)hydroxides dissolve. The simultaneous occurrence of these two processes is exemplified Pederson et al. (2006) who observed that during the dissolution of Fe (oxy)hydroxidese), as well as during the transformation of ferrihydrite and lepidocrocite into more stable phases such as goethite, As may remain adsorbed until the quantity of surface adsorption sites becomes too small. If dissolution continues, As is rapidly released to the aqueous phase. Similarly, remobilization of As occur through the transformation of ferrihydrite into to green rust-like phases (Kocar et al., 2010). Based on these experimental results, we assume in the model that the coprecipitated As is released to the aqueous phase through stochiometric dissolution of the solid mineral. In the model, As release from the solid phase can occur through desorption or dissolution. It is noteworthy that, in contrast to As sequestration studies, relatively few works have been done to investigate the release of As from minerals or soils where it is either adsorbed or coprecipitated. Recent researches have shown that As release is highly dependent on the conditions prevailing when the As-mineral complex was formed (Pedersen et al., 2006).

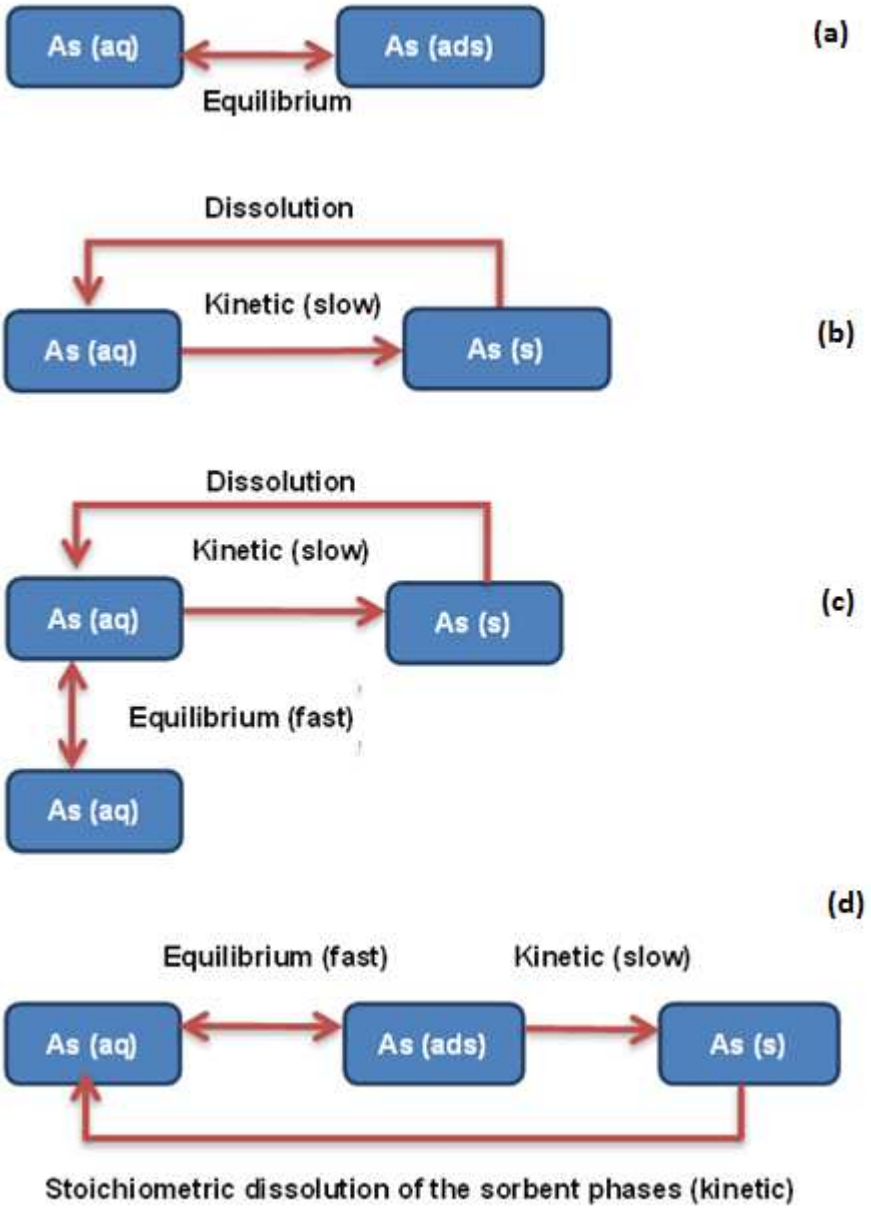

Figure 3-5: Different approaches and pathways of As sorption are depicted. Pools of adsorbed and coprecipitated As which are denoted by As(ads) and As(s), occurs on both of the Fe minerals: FeOH and FeS. a) adsorption of As defined by LEA, b) coprecipitation of As defined by a fully kinetic approach, c) concurrent adsorption and coprecipitation of As defined by a mixed kinetic-equilibrium approach, d) consecutive adsorption and coprecipitation of As defined by a mixed kinetic-equilibrium approach

3.4.4.2. Modeling Approaches

3.4.4.2.1. Adsorption Only: Fully Equilibrium Models

3.4.4.2.1.1. Singe K_d

The mathematical formulation of LEA is mostly commonly done in terms of various isotherms, which are expressions relating sorbed to dissolved concentrations at a fixed temperature. K_d provides a simple mean of describing adsorption in porous media which relates the concentrations of dissolved and adsorbed contaminant through a linear isotherm. However, K_d values are only valid for the specific conditions under which they were determined, and therefore should not be user if geochemical parameters, such as pH, oxidation state of the ions and temperature, have changes (Bethke and Brady, 2000). Despite these shortcomings, the K_d approach is widely used to predict contaminant partitioning in porous media, primarily due to its simplicity

K_d values can be integrated easily within a reactive transport model, bearing in mind that the K_d value is specific to the particular solid phase and a solution composition from which it was extracted.

3.4.4.2.1.2. Variable K_d

Single K_d value does not represent adsorption behavior over a wide range of geochemical conditions, they can lead to unrealistic modeling predictions. For this reason, surface complexation models (SCM) have long been preferred over K_d, despite their complexity. SCM can be used to calculate variable K_d values by imposing the depth-dependant distribution of the geochemical parameters in the aqueous phase, estimated surface site densities and available dataset of adsorption constants. Alternatively, multiple- K_d based on geochemical properties of the solid phase can be determined

experimentally and imposed in the model using empirical equation (Jung et al., 2009). This allowed them to build a reactive transport model for As in a coastal aquifer and to represent the characteristics of distinct geochemical zones. As an additional step, the K_d values obtained using this approach could also be linearly interpolated between the depth intervals in the model.

3.4.4.2.2. Coprecipitation Only: Fully Kinetic Model

Most of the As sorption studies are carried out in batch experiments lasting for a relatively short time, usually from several hours to a few days (Darland and Inskeep, 1997; Elkhatib et al., 1984). While these short time-scales can adequately allow to observation of the fast sorption of As in contact with pure mineral phases, it is likely that the system will approach equilibrium at a slower rate in field conditions. From a modeling perspective, the fact that the equilibrium between the aqueous phase and the surface sites is not achieved implies that the LEA ceases to apply.

The factors that can lead to kinetically-controlled sorption reaction are: i) heterogeneity of surface sites, ii) competition for available surface sites, iii) incorporation into the solid matrix, and iv) pore-scale diffusion. Surface site heterogeneity arises from the variable composition and structures found at both the interparticles and intraparticles scales of soils and sediments. Such a distributions of surfaces sites with different geometries and chemical affinity have a profound impact on sorption reactions. Competitions, on the other hand, refer to the properties of the different aqueous species for a single type of sorption site. For instance, many ions have been shown to compete with As for surface sites (Darland and Inskeep, 1997; Dixit and Hering, 2003). In particular, the competition by natural organic matter (NOM) has received much attention

recently. It has been shown that NOM, when incubated together with As in the presence of hematite, can dramatically delay the attainment of a sorption equilibrium and diminished the extent of sorption of both arsenate and arsenite (Redman et al., 2002). Deviation from LEA can be due to pore-scale diffusion, as often described in soil matrices in which solutes can diffuse into the pores formed by aggregated particles. In a fully kinetic approach, all the above described kinetic factors can be lumped in a single-step slow reaction assuming the whole sorbed As is coprecipitated.

3.4.4.2.3. Mixed Kinetic-Equilibrium Models

A method to deal with the simultaneous fast and slow As uptake through adsorption and coprecipitation is to use a "multisite model". The formulation of such a model needs the prescription of the number of the sites, or compartments which are either at equilibrium or undergo kinetically controlled reactions. The most common multisite model is a two-sites model where it is assumed that the sorbate is divided into two fractions, one that is at fast local equilibrium with the sorbent and one that is governed by the slow and kinetically controlled uptake (Qi and Donahoe, 2008, 2011; Zhang and Selim, 2006, 2008). This model, which assumes that kinetic and equilibrium sorption sites are available simultaneously, will be hereafter referred to as the concurrent mixed model.

It has been demonstrated that equilibrium and kinetically controlled reaction can not only simultaneously but also one after another, i.e, that sequestration can first proceed through adsorption then continues through co-precipitation (Darland and Inskeep, 1997; Elkhatib et al., 1984; Tronc et al., 1992). In order to account for this two-step sorption mechanism, we introduce the consecutive mixed kinetic-equilibrium model, where fast

adsorption on the sorbent surface is followed by the slow coprecipitation. In the consecutive mixed model, the rate of the coprecipitation depends on the concentrations of the adsorbed phase instead of the concentrations of sorbents, as in the concurrent mixed model.

*3.4.4.3. **Mathematical Representation Of Reactive-Transport Equations***

Due to the interplay of the various kinetic factors described above, a multisite model is needed to consider several interaction of As with the solid phase matrix. Equation (2.1) for a solute concentration of *C* is modified to impose multisite model as below:

$$\varphi \frac{\partial C}{\partial t} + (1-\varphi)\rho_b \sum_{j=1}^{P} \sum_{k=1}^{M} \frac{\partial S_{jk}}{\partial t} = \left[\frac{\partial}{\partial x}(\varphi D C) - \frac{\partial}{\partial x}(\vartheta \varphi C)\right] + \varphi \sum r_m \tag{3.17}$$

$$S_{ads\_jk} = f(C, C', S', A, B, K, \dots) \tag{3.18}$$

$$\frac{\partial S_{cop\_jk}}{\partial t} = g(C, C', S', A, B, K, \dots) \tag{3.19}$$

$$S_{jk} = S_{ads\_jk} + S_{cop\_jk} \tag{3.20}$$

where S_{ads_jk} is the adsorbed concentration, S_{cop_jk} is the coprecipitated concentration on k^{th} site of sorbent j and S_{jk} is the total sorbed concentration including adsorbed and coprecipitated pools. P is the number of distinct sorbent phases, and M is the number of sorption site types. Based on this formulation, total pools of $P \times M$ sorbed sites are distinguishable. Equations (3.18) and (3.19) thus express adsorption and coprecipitation pathways, respectively, according to general appropriate equilibrium isotherm and kinetic rate laws. They relate the concentrations of dissolved species in aqueous phase to the sorbed concentrations on solid phase.

Coprecipitation rate law is lumped along with other rate controlled reactions such as dissolution, precipitation and microbially-mediated ones, in the chemical rate expression of the generic equation ($\sum r_m$) as follow:

$$\sum r'_m = \varepsilon \sum r_m + (1-\varepsilon)\rho_b g(C, C', S', A, B, K, \dots) \tag{3.21}$$

where $\sum r'_m$ is the modified rate term. The isotherm Equation (3.18) applies to all times and depths and its differentiation with respect to these variables results in Equations (3.22) and (3.23), respectively:

$$\frac{\partial S_{ads\_jk}}{\partial t} = \frac{\partial S_{ads\_jk}}{\partial C}\frac{\partial C}{\partial t} + M \tag{3.22}$$

$$\frac{\partial S_{ads\_jk}}{\partial x} = \frac{\partial S_{ads\_jk}}{\partial C}\frac{\partial C}{\partial x} + N \tag{3.23}$$

where:

$$M = \sum_{\propto} \frac{\partial S_{ads\_jk}}{\partial h_{\propto}}\frac{\partial h_{\propto}}{\partial t} \tag{3.24}$$

$$N = \sum_{\propto} \frac{\partial S_{ads\_jk}}{\partial h_{\propto}}\frac{\partial h_{\propto}}{\partial x} \tag{3.25}$$

and $h_{\propto}$ represents all other parameters upon which S_{ads_jk} depends, as shown in equation (3.18). It should be noted that $M = N = 0$ in an environment where constant surface properties with respect to depth and time are assumed. Furthermore, in the mixed kinetic-equilibrium approaches, Equations (3.18) and (3.19) are solved simultaneously with Equation (3.17).

In aqueous sediment application (ASA) two PDEs (one for dissolved species and one for the adsorbed component) and the Equations (3.18) and/or (3.19) are solved simultaneously. These two PDEs can be coupled in a unique general diagenesis equation to represent the spatial and temporal changes in the distribution of dissolved species due

to diffusion, pore water advection, burial, compaction and slow chemical kinetic reactions (Berner, 1976):

$$I\frac{\partial(\varphi C)}{\partial t} = \left[\frac{\partial\left(\varphi D_{dif}\frac{\partial C}{\partial x}\right)}{\partial x} + \frac{\partial\left(\varphi F D_b\frac{\partial S}{\partial x}\right)}{\partial x}\right] - \varphi\left(V_{flow} + \omega F\frac{\partial S}{\partial C}\right)\frac{\partial C}{\partial x} - IC\frac{\partial(\varphi V_f)}{\partial x} - \varphi F(M + \omega N) + \sum r'_m \quad (3.26)$$

where I is the retardation factor equals to $1 + F\frac{\partial S}{\partial C}$.

For the special case of single-*K*d, where constant surface properties with depth and time are assumed (*M=0*, *N=0*), there is no compaction or externally impressed flow ($\omega = V_f, \frac{\partial\omega}{\partial x} = 0$) and no porosity change with depth or time ($\frac{\partial\varphi}{\partial x} = \frac{\partial\varphi}{\partial t} = 0, D_{dif} = \text{constant}, F_{con} = \text{constant}$), equation (12) reduces to:

$$I\frac{\partial C}{\partial t} = D_{dif}\frac{\partial\left(\frac{\partial C}{\partial x}\right)}{\partial x} + D_b\frac{\partial\left[(I-1)\frac{\partial C}{\partial x}\right]}{\partial x} - wI\frac{\partial C}{\partial x} + \sum r'_m \quad (3.27)$$

3.4.4.4. ***Results***

Modeling results show that a purely equilibrium description of the partitioning of As between pore water and solids fails to reproduce the depth profiles of of As measured in the lake sediments. This is because the concentration gradients in the depth pore water profiles cannot be captured by equilibrium approach. Both the kinetic and mixed kinetic-equilibrium descriptions capture the observed features of the pore water and solid-bound As profiles (see Figure 3.6). However the mixed kinetic-equilibrium approach, which includes fast, reversible adsorption, followed by slow As coprecipitation plus stoichiometric dissolution of the sorbent phases (ferric iron oxyhydroxides and iron sulfides), allows us to compare fitted adsorption parameters with values obtained in controlled laboratory experiments. By describing fast As adsorption with the surface

complexation model, the effects on As partitioning of variations in the nature of the sorbents and variations in pore water pH and ionic strength are explicitly accounted for.

It is important to have an estimation of adsorbed versus coprecipitated As simulated by different approaches. For this purpose, we plot the coprecipitated fraction of the As versus depth which is shown in Figure 3.7. As it expected fully kinetic approach predicts the 100% of the sorbed As on the solid phase is in the coprecipitated form. The consecutive and concurrent approaches show a decrease in the fraction of coprecipitated As till depth of 3 cm and then increase of this fraction to 100%. The minimum of the coprecipitated As profile coincides with As release as a result of reductive dissolution ferric iron oxyhydroxides. However, consecutive model predicts higher concentration of adsorbed As with respect to the concurrent one at this depth. This is because in consecutive model the whole sites of the solid phase are considered as equilibrium sites which are equilibrated by the released As in pore water. In concurrent approach fraction of the solids sorbing sites are available as equilibrium ones while the remaining sites sorb As through slow and rate controlled reactions. This proves that, truly adsorbed As is a minor fraction of the solid phase As pool in the sediment.

3.5 Applications

The sections below present three MATSEDLAB applications. The corresponding m-files are provided for some scenarios have been provided and listed in Table 3.5 and are supplied in the Supplementary Materials. The applications illustrate how the code can be adapted to address a wide variety of early diagenetic problems and scenarios. All the figures accompanying the applications have been generated directly in MATLAB by accessing the array *sol*, which stores the results at the end of a simulation.

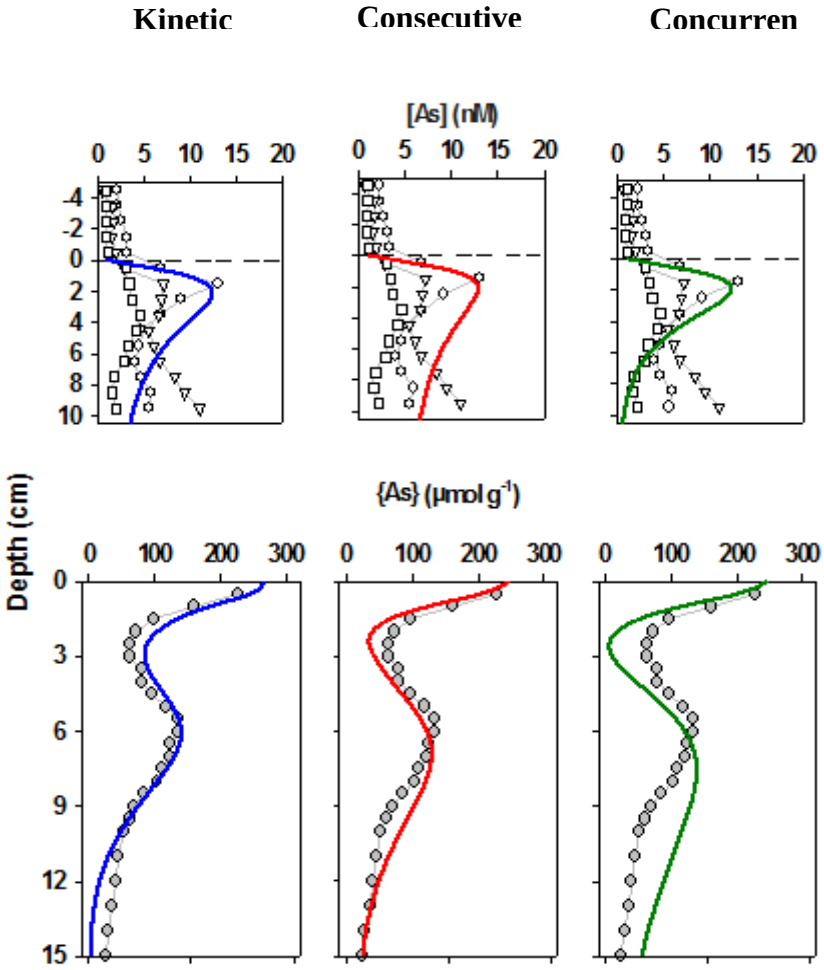

Figure 3-6: Sorbed As profiles versus depth simulated with different modeling approaches

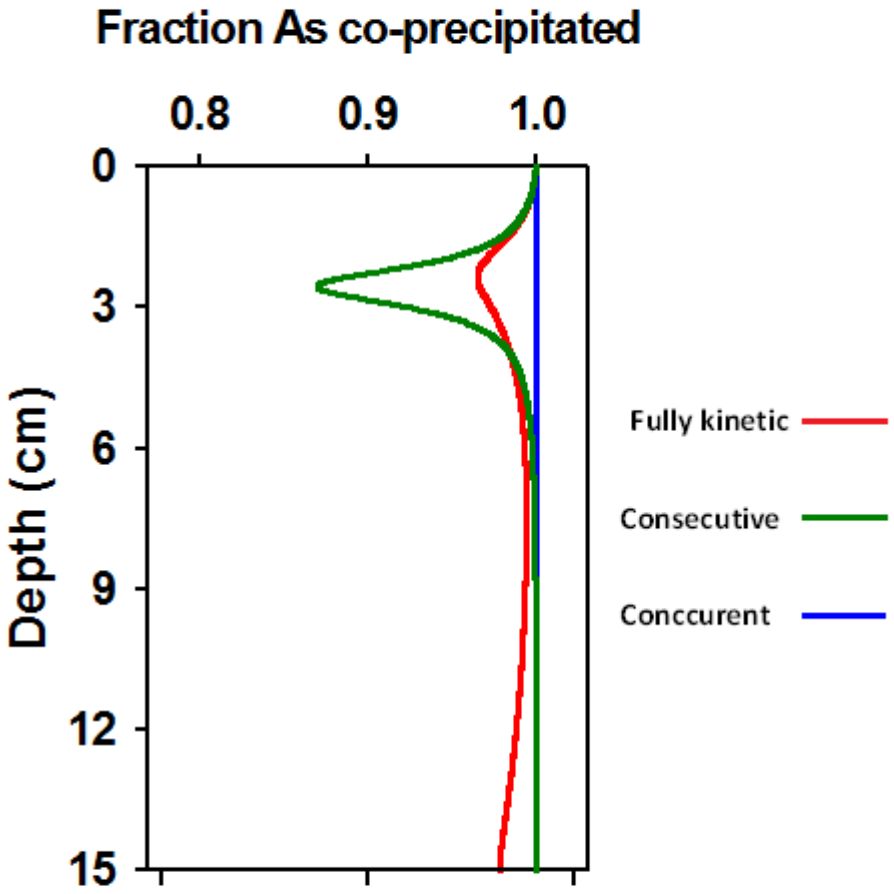

Figure 3-7: Coprecipitated fraction of As on solid phase predicted by different modeling approaches.

3.5.1. Seasonal Organic Carbon Deposition

In *MATSEDLAB_00.m*, the organic carbon oxidation rate is assumed to follow a fixed, exponentially decaying depth distribution, $R_C = R_C^0 e^{(-0.183x)}$ (where x is depth in cm, Table 3.2). The distribution derived from direct rate measurements obtained in sediment incubation experiments (Couture et al., 2010b). Alternative descriptions of organic carbon oxidation may be more appropriate when such measurements are not available, however. The script *MATSEDLAB_app_02.m*, for example, computes the distribution of R_C using the classic G-model description for organic matter degradation (Westrich and Berner, 1984). Degradable organic matter is assumed to be supplied as two distinct pools: a highly labile pool and a less labile pool to which the first-order degradation constants k_{OM1} (0.1 yr^{-1}) and k_{OM2} (0.001 yr^{-1}) are assigned (Canavan et al., 2006). The deposition fluxes of the two types of organic carbon, J_{OM1} and J_{OM2}, are then specified as upper boundary conditions (Note that in *MATSEDLAB_app_02.m* the reactions involving As have been removed). The *MATSEDLAB_app_02.m* script presents two options for J_{OM1} and J_{OM2}, which can be turned on or off by the user (see lines 122-126). In the first option, J_{OM1} and J_{OM2} are assigned constant values of 300 and 150 µmol C cm^{-2} yr^{-1}, respectively. In the second option, the deposition fluxes J_{OM1} and J_{OM2} are assumed to vary seasonally, according to $J_{OM1} = 300[\cos(2\pi t) + 1]$ and $J_{OM2} = 150[\cos(2\pi t) + 1]$, where time is expressed in years and t=0 corresponds to July 1. The deposition fluxes J_{OM1} and J_{OM2} peak in early summer, with maximum values of 600 and 300 µmol C cm^{-2} yr^{-1}, respectively, and drop to zero on January 1 (Figure3.8). (Note: the seasonal functions are inspired from Dittrich et al., 2009.) Integrated over one year, the deposition fluxes are the same in the constant and variable deposition scenarios. Again, the user can

Table 3-5: List of m.files included in the MATSEDLAB package

General functions	**Corresponding m.files**
- Main file	*MATSEDLAB_00.m*
- Write results	*MATSEDLAB_01.m*
- Read measured data	*MATSEDLAB_02.m*
- Plot results and data	*MATSEDLAB_03.m*
Applications	**Corresponding m.files**
Arsenic early diagenesis in lake sediment	*MATSEDLAB_app_01.m*
Seasonality in organic matter benthic fluxes	*MATSEDLAB_app_02.m*
Fe oxides phase transformation	*MADSEDLAB_app_03.m*

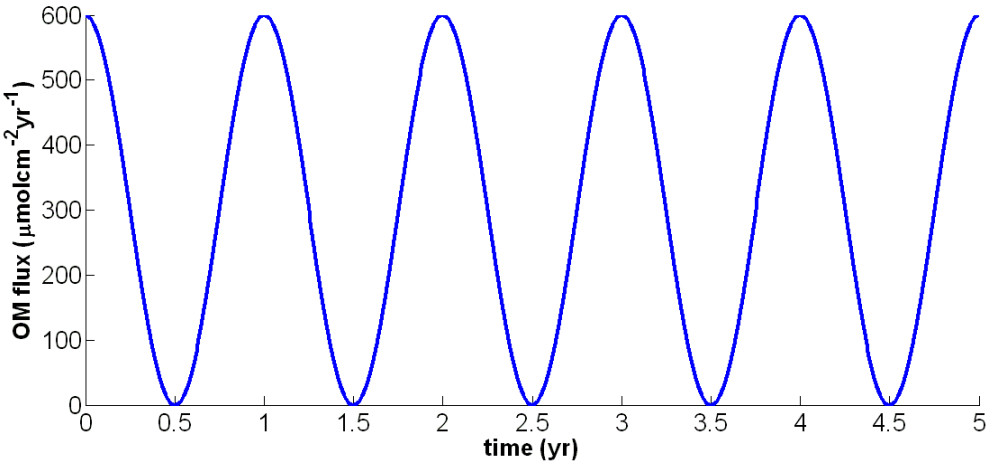

Figure 3-8: Seasonally variable organic carbon deposition flux imposed as boundary conditions. (Note: for clarity only the deposition flux of the most labile organic carbon fraction, J_{OM1}, is shown.)

replace the example descriptions of J_{OM1} and J_{OM2} by those of her choice. Examples of the output of *MATSEDLAB_app_02.m* are presented in Figures 3.9 and 3.10, for the first 20 years of simulation, using the built-in plotting capabilities of MATLAB. Figure 3.9 shows the time evolution of the concentrations of ferric iron (oxy)hydroxides and ferrous iron monosulfides at 4 different depths in the sediment, for the seasonally varying organic carbon deposition fluxes. Note that all the pore water and solid sediment concentrations are initially set to zero in the simulation. The results in Figure 3.9 therefore also illustrate the time scale required for the solid-bound sediment composition to relax from the imposed initial conditions. In the particular case simulated, this requires on the order of 20 years. The depth-dependent patterns in Figure 3.9 reflect the interplay between the depositional supply of reactive Fe(III) (oxy)hydroxides at the SWI, the redistribution of iron phases by sediment advection and bioturbation, and the progressive transformation of the Fe(III) oxyhydroxides into iron sulfides as a result of Fe(III) and sulfate reduction. The temporal patterns in Figure 3.9 are indistinguishable from those computed when the constant values of J_{OM1} and J_{OM2} are imposed, except for the concentrations very near the SWI. As can be seen, at $x = 0$, the concentrations of iron (oxy)hydroxides and monosulfides show seasonal oscillations as a result of the periodic supply of organic carbon. The fluctuations in the concentrations are very small, however, and completely vanish deeper in the sediment. In other words, the solid-state iron profiles primarily record the yearly averaged organic carbon deposition. The situation is very different for the pore water profiles, as shown in Figure 3.10 where the depth profiles of sulfate, free sulfide and aqueous ferrous iron exhibit distinct differences between summer and winter. In other words, the pore water profiles resolve the seasonal variations in the externally

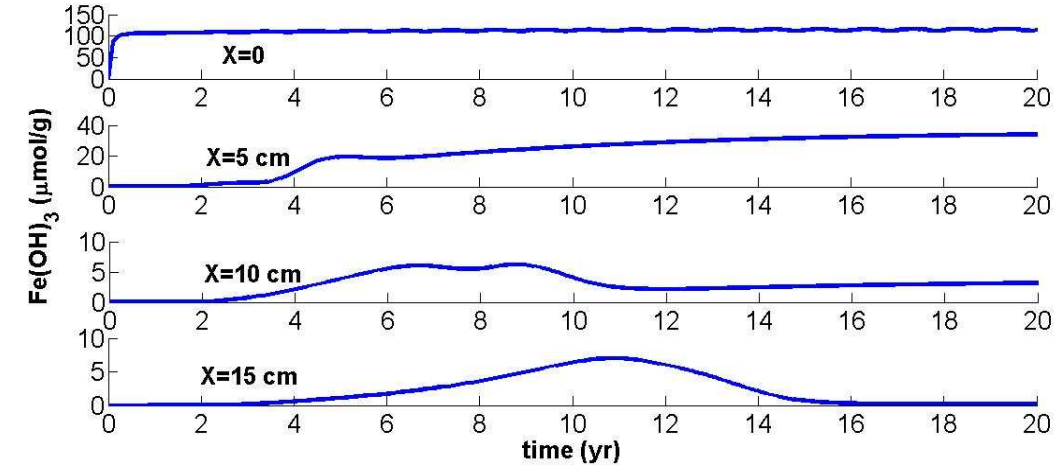

(a)

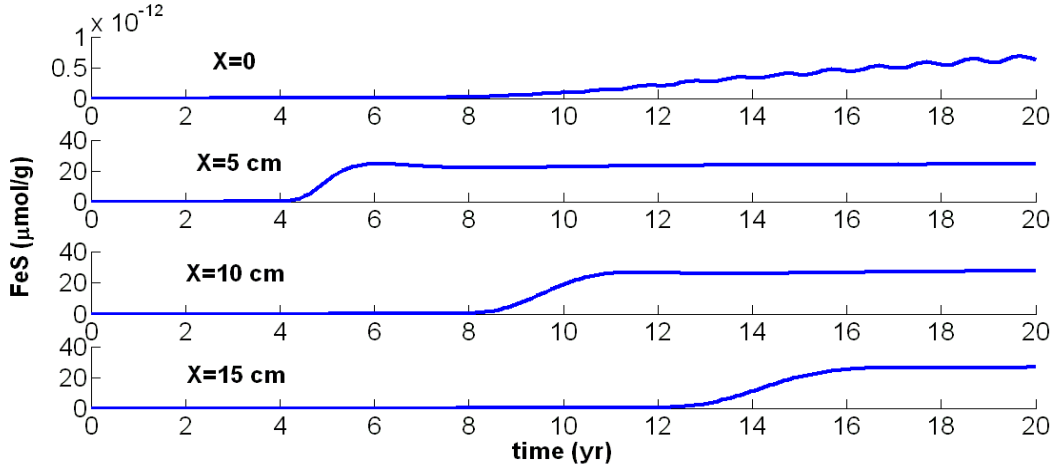

(b)

Figure 3-9: Time evolution of (a) $Fe(OH)_3$ and (b) FeS concentrations over the first 20 yr in Application 2, under seasonally variable organic carbon deposition.

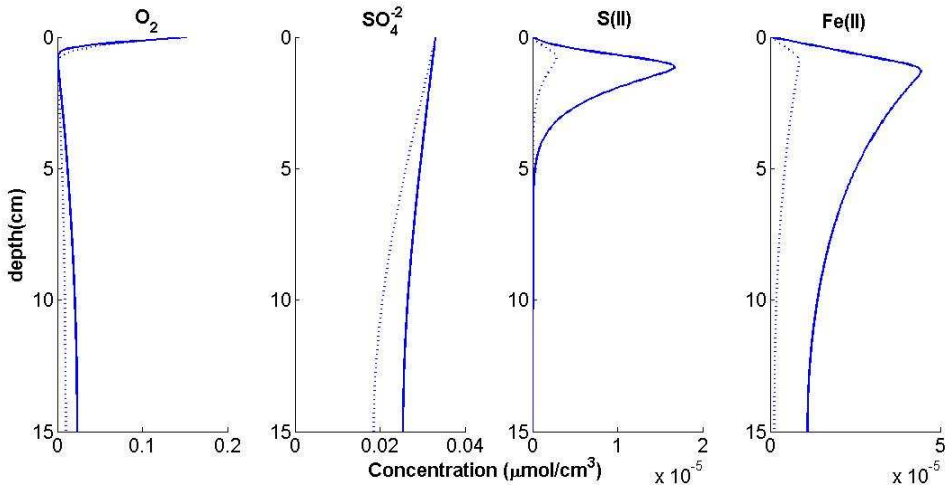

Figure 3-10: Snapshots of the concentration depth profiles of pore water O_2 (panel a), sulfate (panel b), sulfide (panel c) and ferrous iron (panel d) in the month of January (dark line) and July (light line) in Application 2, under seasonally variable organic carbon deposition.

forced input of degradable organic carbon, while solid-state profiles are sensitive to changes at longer time scales.

3.5.2. Iron Phase Transformations

Iron mineral transformations play a key role in biogeochemistry and contaminant mobility (Borch et al., 2010). In most early diagenetic models, reactive Fe(III) phases are lumped together in a single pool, loosely represented by the chemical formula $Fe(OH)_3$ (e.g., Table 3.2). This pool is assumed to exhibit properties resembling those of poorly crystalline hydrous ferric oxides such as ferrihydrite(Hyacinthe et al., 2006). These phases are ubiquitous in soils and sediments, particularly under fluctuating redox conditions (Cornell, 2003), and they are among the most bioavailable Fe(III) phases used by dissimilatory iron reducing bacteria (Lovley and Phillips, 1986). They are, however, notoriously short-lived and rapidly transform into other Fe-bearing phases, such as goethite (α-$Fe^{III}OOH$), lepidocrocite (γ-$Fe^{III}OOH$) and magnetite ($Fe^{II}OFe^{III}{}_2O_3$) (Hansel et al., 2003; Tronc et al., 1992). That is, solid state Fe(III) in sediments is typically made up of an assemblage of mineral phases of variable properties. The transformations of Fe(III) minerals may markedly impact the uptake and release of contaminants (Pedersen et al., 2006). They also affect the activity of iron reducing microorganisms and the conversion of Fe(III) into Fe(II) sulfide phases under sulfate reducing conditions.

Here, we expand the representation of Fe(III)-bearing mineral phases used in the scripts discussed earlier by including 3 pools in the *MATSEDLAB_app_03.m* script: 1) highly reactive ferric hydrous oxides, $Fe(OH)_3$, 2) magnetite and 3) goethite (lepidocrocite is lumped into this pool). The system of reactions involving the Fe(III) minerals are summarized in Table 3.6: it is inspired by the work of Pallud et al., (2010).

who studied the reductive dissolution of ferrihydrite and the accompanying formation of secondary Fe minerals in soil aggregates. Both $Fe(OH)_3$ and magnetite are potential electron acceptors for dissimilatory iron reduction, while goethite is assumed to be a stable end-product. (Note: the user can easily relax the latter assumption if needed.) Goethite is assumed to form directly through the dehydration of $Fe(OH)_3$, while magnetite forms through the translocation of an electron from Fe(II) into $Fe(OH)_3$ (Table 3.6). Following (Pallud et al., 2010), we also include the passivation of $Fe(OH)_3$ by sorbed Fe(II). The rate of dissimilatory reduction of $Fe(OH)_3$ is then given by:

$$R_2 = R_c f_{Fe(OH)3} \tag{3.28}$$

with

$$f_{Fe(OH)3} = \left(\frac{\{Fe(OH)3\}}{K_{m\_Fe(OH)3}+\{Fe(OH)3\}}\right)\frac{K_{in\_O2}}{K_{in\_O2}+[O2]}p \tag{3.29}$$

and

$$p = \frac{S_{Fe(OH)3}-[Fe_{sorbed}]}{S_{Fe(OH)3}} \tag{3.30}$$

The term $f_{Fe(OH)3}$ is the fraction of organic carbon oxidation that is coupled to $Fe(OH)_3$ reduction, $K_{m\_Fe(OH)3}$ is the half-saturation constant for $Fe(OH)_3$ utilization, and K_{in_O2} accounts for the inhibitory effect of molecular oxygen on dissimilatory iron reduction (VanCappellen and Wang, 1996). Equation (3.29) differs from the formulation for dissimilatory iron reduction used in the earlier MATLAB scripts through the term *p*, which corresponds to the surface passivation of ferrihydrite by adsorbed Fe(II). The latter lowers the reducibility of $Fe(OH)_3$ by changing its electron density (Yang et al., 2010). Note that *p* varies dynamically between 0 and 1, depending on the fraction of surface sites $S_{Fe(OH)3}$ that is occupied by adsorbed Fe(II). The total concentration of ferrihydrite

Table 3-6: Reaction network and kinetic formulations for Fe oxides phase transformation.

Description	Reaction	Kinetic formulation	Parameter	Value*	Unit
Fe oxide reduction	$CH_2O + 4Fe(OH)_{3(s)} + 7CO_2 + H_2O \rightarrow 4Fe(II) + 8HCO_3^- + 3H_2O$	$R_{resp\_fer} = Rc\ f_{Fe(OH)3}$			
Magnetite reduction	$CH_2O + 2Fe^{II}Fe^{III}{}_2O_4 + 11CO_2 + 5H_2O \rightarrow 6Fe(II) + 12HCO_3^-$	$R_{resp\_mag} = Rc\ f_{mag}$			
Goethite formation	$Fe(OH)_{3(s)} \rightarrow \alpha\text{-}FeOOH + H_2O$	$R_{FeOOH} = k_{FeOOH}[Fe(II)]\{Fe(OH)_3\}$	k_{FeOOH}	50	yr^{-1}
Magnetite formation	$\frac{1}{3}Fe(II) + \frac{2}{3}Fe(OH)_{3(s)} \rightarrow \frac{1}{3}Fe^{II}Fe^{III}{}_2O_4 + \frac{2}{3}H_2O + \frac{2}{3}H^+$	$R_{mag} = k_{mag}[Fe(II)]\{Fe(OH)_3\}$	k_{magn}	15.5	yr^{-1}
Fe(II) sorption	$Fe(II) \leftrightarrow Fe_{sorbed} + H_2O$	$[Fe_{sorbed}] = K_{sorp}S_{Fe(OH)3} \times \frac{[Fe(II)]}{[H+] + Ksorp[Fe(II)]}$	K_{sorp}	$10^{-2.5}$	-

*Parameters values from (Pallud et al., 2010)

surface sites (in mol per gram sediment) is calculated as:

$$S_{Fe(OH)3} = \{Fe(OH)3\} \times SA \times SD \times MW_{Fe(OH)3} \quad (3.31)$$

where SA is the specific surface area of ferrihydrite (m^2 g^{-1}), SD the site density of ferrihydrite (mol m^{-2}), $MW_{Fe(OH)3}$ the molecular weight (g mol^{-1}), and $[Fe_{sorbed}]$ is the concentration of the adsorbed iron on ferrihydrite (mol g^{-1}). Sorption of Fe(II) to ferrihydrite is assumed to follow a Langmuir isotherm (Table 3.6, see line 173 in *MATSEDLAB_app_03.m*). No passivation is included for magnetite.

Final (near-steady state) depth distributions of the fractions of the individual oxides computed with *MADSEDLAB_app_03.m* are shown in Figure 3.11. The simulations correspond to the same boundary conditions as those in Application 1. Note further that all reactive Fe(III) deposited at the SWI is assumed to be under the form of $Fe(OH)_3$. That is, magnetite and goethite are all formed during early diagenesis. Obviously, different scenarios can be implemented, for instance, where the deposition of Fe(III) occurs as a mix of oxides. For the early diagenetic scenario simulated here, goethite replaces ferrihydrite as the dominant iron oxide below 10 cm. The magnetite concentration remains about two orders of magnitude smaller than that of goethite.

The time scale over which the transformation of $Fe(OH)_3$ into more stable oxide phases takes place is illustrated in Figure 3.12, where the relative abundances of the different iron oxides are plotted versus time at a fixed depth of 15 cm. As can be seen, it takes several decades for the secondary iron oxides (goethite and magnetite) to reach their final concentrations. That is, the stabilization of reactive Fe(III) through transformation into stable iron oxides is a relatively long-term process. This may help

explain why the simple representation of a single reactive Fe(III) sediment pool may in many cases be sufficient to capture the rapid redox cycling of iron close to the SWI.

3.5.3. Non Steady-State Modeling Of Early Diagenesis Following A Flood Event

Coastal areas are of major importance when looking at the carbon and nutrients fate in the ocean as they represent the transition between terrestrial and marine environments. They are subjected to anthropic and natural perturbations that can have a great impact on the physical, biological and chemical processes occurring in the water and the sedimentary column. The processes controlling organic matter (OM) cycling in coastal sediments are important as it contributes to the CO_2 balance of the coastal area and it is the source of nutrients to the water column (Chen and Borges, 2009; Pratihary et al., 2009).

In this application, a major flood event of the Rhône River occurred in June 2008 is simulated while several stations close to the mouth of the river were sampled (Pastor et al., 2011). As a result a major disruption of the normal sedimentation regime was occurred, and followed by the quick accumulation of thick new sediment with less concentration of labile compounds associated to fine material and richer in inorganic carbon. It has also been shown that during the flood deposition the oxygen demand in the prodelta decreases by 20-30% which is the indicator of deposition of a large quantity of low reactivity material originating from soils in the drainage basin near the outlet of the Rhone River (Cathalot et al., 2010). We focus here on one of the stations that received 32 cm of flood deposit during the event. The transient biogeochemical model MATSEDLAB is used to: 1) understand and quantify the impact of this deposit on biogeochemical processes and 2) simulate the relaxation of the sediments if we suppose that the processes

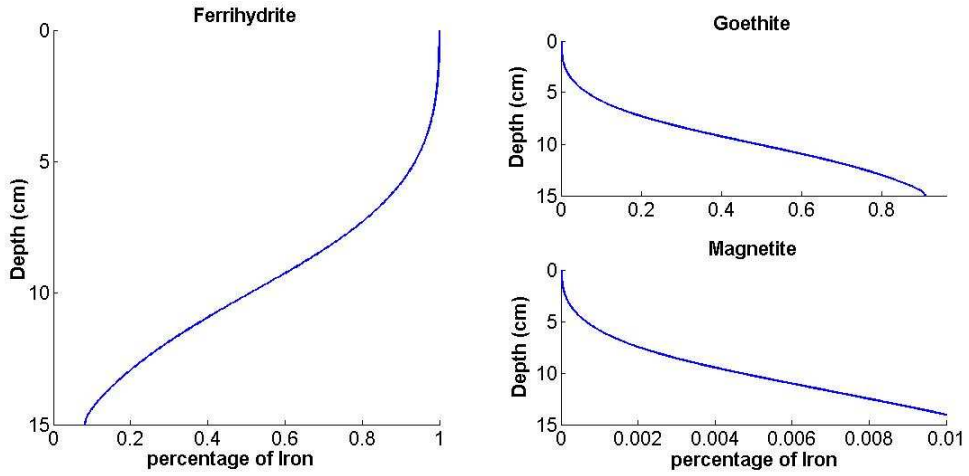

Figure 3-11: Depth profiles of the fractions of solid-phase iron oxides (hydrous ferric (hydr)oxides, goethite and magnetite). (Note: the results plotted correspond to a simulation run-time of 100 years.)

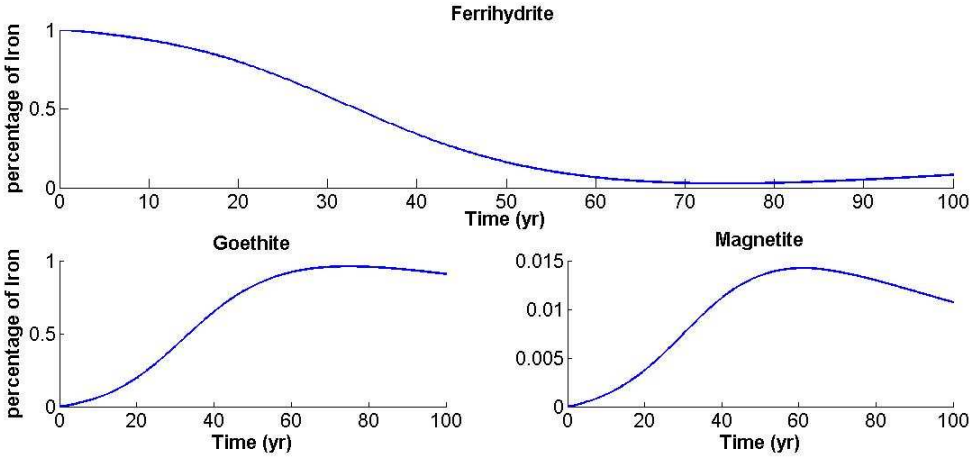

Figure 3-12: Fractions of solid-phase iron (ferrihydrite, goethite, magnetite) as a function of time at a depth of 15 cm.

and boundary conditions went back to “preflood” conditions after the event. The challenge in this study was to simultaneously change multiple boundary conditions through time to simulate the quick deposition of a new thick layer with different characteristics. Apart from the biogeochemical understanding of each process, this was led to many numerical issues that were successfully resolved at each step of the modeling work. The proposed reaction network includes:

- 18 species and 19 reaction pathways.
- 3 pools of OM (fast, slow and refractory, with different C/N and degradation constants)
- 1 pool of MnO_2 and 2 pools of $Fe(OH)_3$ (biotic and abiotic reactions)
- 6 primary reactions (O_2, NO_3^-, MnO_2, $Fe(OH)_3$, SO_4^{-2}, OM) that yield to the production of reduced species (Mn^{2+}, Fe^{2+}, NH_4^+, $\sum H_2S$, CH_4)
- 13 secondary reactions: reoxidation by O_2, MnO_2, $Fe(OH)_3$ and SO_4^{-2}, FeS and FeS_2 formation (linked to pH profile), OM sulfizidation
- Transport processes are represented by sedimentation, advection, bioturbation (mixing process), irrigation and diffusion.
- Molecular diffusion coefficients of dissolved species are corrected for temperature and porewater viscosity and for sediment porosity.
- The formulations used to describe porosity and $[H^+]$ concentrations are derived from data while bioturbation and irrigation are derived from literature.

Difference between preflood and flood conditions include:

- The bioturbation rate was set to 50 cm^2 yr^{-1} during the flood (vs. 1 and less in

preflood conditions) to allow for the mixing of the deposit

- No irrigation during the flood
- pH and porosity constant during the flood
- No nitrification during the flood
- Enhancement of manganese reduction at the surface (×2) and precipitation term added during the 11 days
- No iron reduction in the top 15 cm during the 11 days
- No sulfate reduction in the top 10 cm during the 6 days of deposition
- Enhancement of sulfate reduction below the flood deposit (×4) and（×60) for fast and slow OM pools respectively)

The quick deposition of thick sediment could be responsible for the enhancement of the iron and sulfate reduction below the flood deposition due to the new source of fresh OM. After the flood event, the boundary conditions were back to preflood conditions. From the modeling results (see Figure 3.13) on four pore water species (Mn^{2+}, Fe^{2+}, SO_4^{-2} and DIC) we can observe two different features:

- SO_4^{-2} and DIC profiles are correlated while sulfate reduction being the major OM mineralization pathway at this station. The relaxation of these two species is thus highly similar, with a profile close to the preflood profile around 60 days after the flood event. The profiles still reflect the flood deposition with a slightly different shape than preflood.
- Mn^{2+} and Fe^{2+} profiles do not re-equilibrate as fast as the other species presented

here. In the surface layer, the $Fe(OH)_3$ reduction is visible with Fe^{2+} starting to accumulate. In lower depth, as no more MnO_2 or ΣH_2S are available to react, the Fe^{2+} peak formed during the flood is slowly diffused. Mn^{2+} diffuses very quickly toward the oxic zone following the first days of the flood (MnO_2 increases, at the sediment surface) and then stabilizes with a slight accumulation at the surface due to MnO_2 reduction.

3.5.4. Sediment Diagenesis Modelling In An AMD Contaminated Reservoir

The Sancho water reservoir is located in the Odiel Basin, Huelva (SW Spain) in the Iberian Pyrite Belt. The Basin has been mined intensively during the last century. While the mines are now abandoned, the Basin is still heavily contaminated by acid mine drainage (AMD). The reservoir has a pH of ~4, with high SO_4^{-2} (200 ppm) and heavy metal concentrations in the water column. A monomictic behaviour forces the reservoir to mix in winter, which oxigenates the bottom waters. Solid and aqueous phases analyses were done by Torres et al. (2011). The results showed that the sediment acts as a sink of trace elements (e.g. As, Cd, Pb) during oxic conditions and as a source for them during anoxic conditions at the bottom (Torres E., 2011).

Quantitative transport-reaction modeling of sediment diagenesis has been performed by MATSEDLAB. The model has been modified by including: $FeCO_3$ as a new phase, pH and porosity functions with depth, and two organic matter (OM) pools. Due to the monomictic behavior of the reservoir non-steady-state boundary conditions were imposed as a function of time for O_2, as an error function, and for the $Fe(OH)_3$ (s) flux, because of its dependence on the O_2 concentration (Figures 3.14 and 3.15). The reaction network includes three primary reactions describing the degradation of OM via

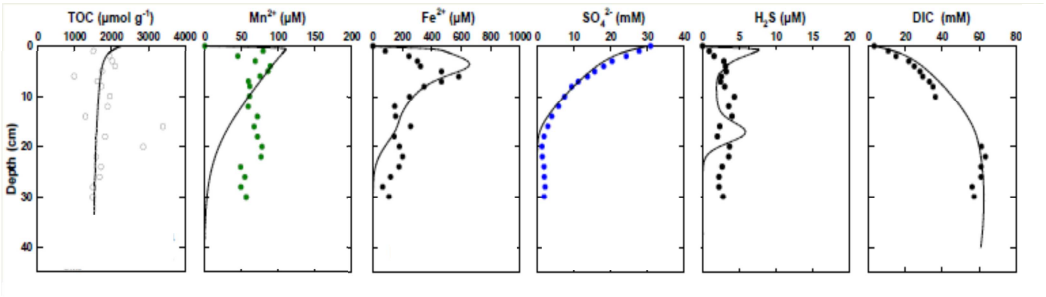

(a)

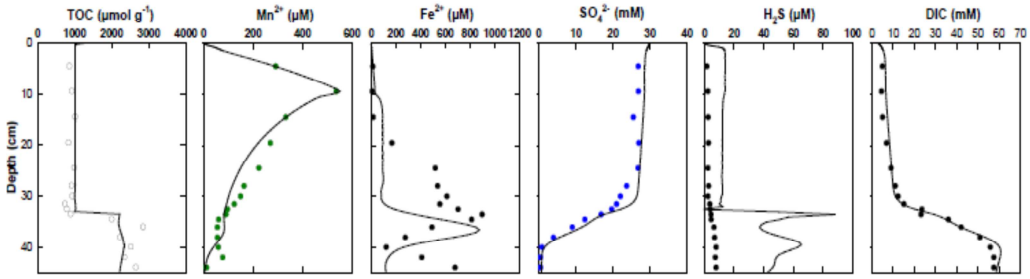

(b)

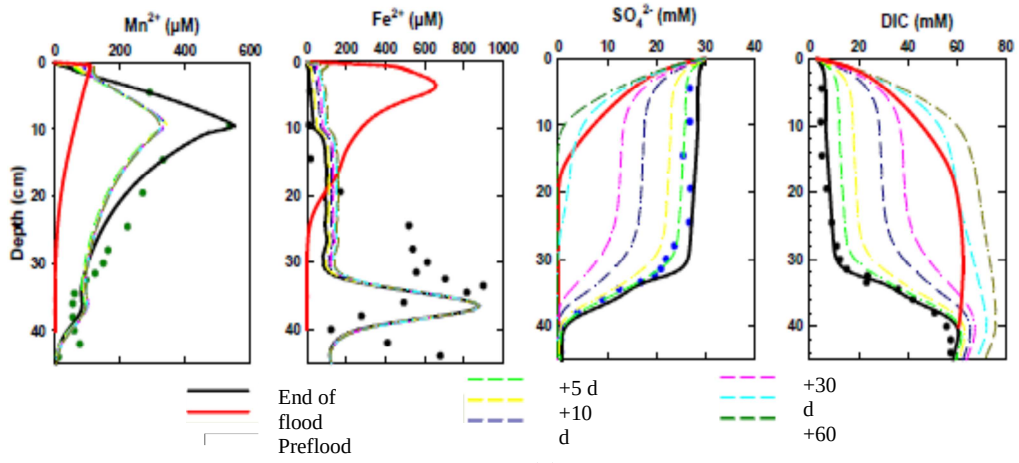

(c)

Figure 3-13: Modeled and measured sediment profiles: (a) preflood profiles, (b) flood profiles and (c) sediment relaxation

oxic respiration, iron and SO_4^{-2} reduction. The secondary reactions considered are the oxidation of pore water Fe(II) by O_2, and of H_2S by O_2 and Fe $(OH)_3$ (s).

The Fe $(OH)_3$ (s) and SO_4^{-2} are reduced in the upper few cm, releasing Fe^{2+} and H_2S which precipitate as FeS and pyrite. Excess of Fe^{2+} precipitates as $FeCO_3$. Under anoxic conditions solute concentrations on sediment pore water increase due to the absence of oxygen. The model predicts a flux of 60 µmol Fe(II)/cm^2/y from the sediment to the overlying water during the stratified period (anoxic) and no flux during the turnover (oxic). Owing to the time- dependent O_2 function implemented in the model, we obtain a periodic response for the years simulated which allow us to reproduce the complex features of the measured sedimentary profiles.

Arsenic follows the same pattern as it is co-precipitated within the iron oxides minerals and its concentration in the solid phase decreases with depth while in pore water increases, due to Fe(III)- hydroxide dissolution, where As is a minor constituent. Sulfide-linked trace metals (Cd, Pb, Cu, Zn) undergo opposite behavior: during the stratified period the flux goes from the water column to the sediment. The flux is reverted during the turnover due to the oxidation of the sulfides that have precipitated during the stratified period.

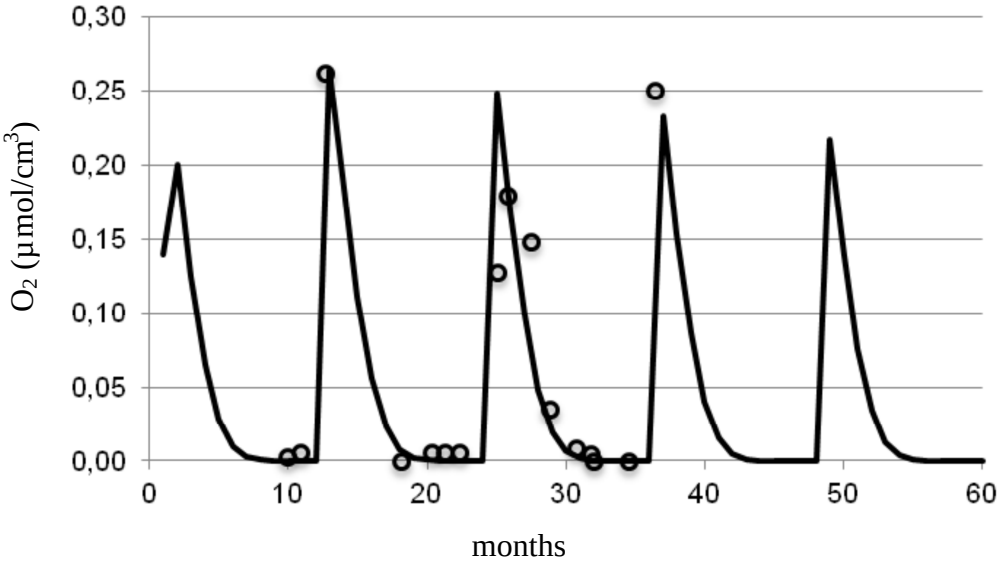

Figure 3-14: Oxygen concentration in the upper part of the sediment versus time. The points correspond to analytical data and the line to the model results.

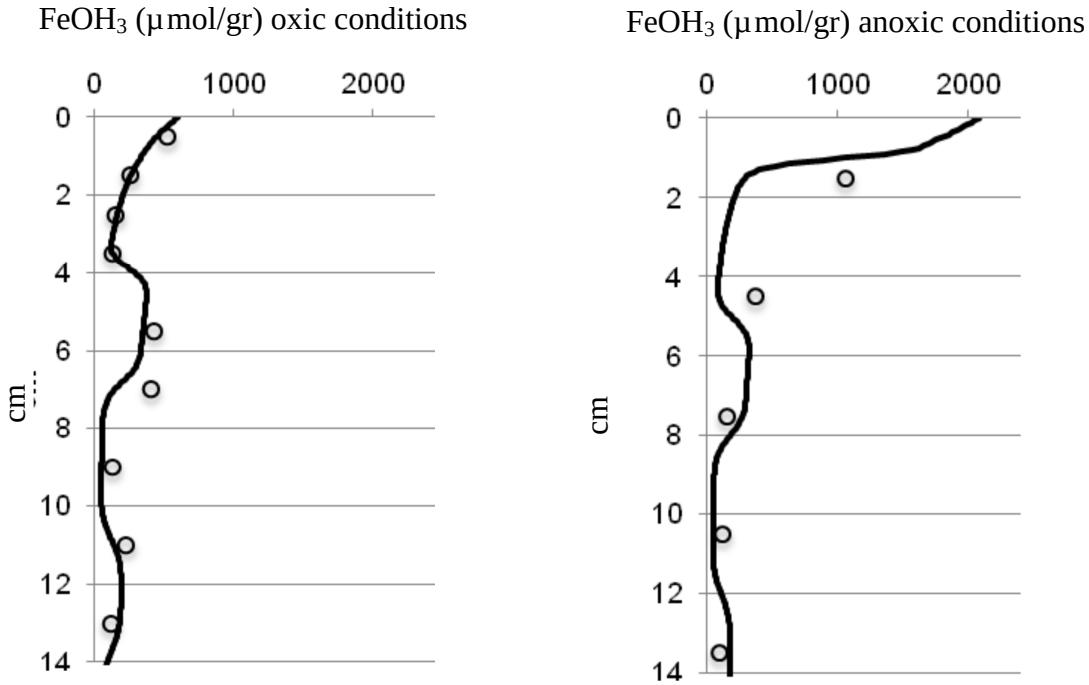

Figure 3-15: Fe(III)-amorphous concentration in µmol/g under oxic (turnover, on the left) and anoxic (termocline, on the right) conditions versus depth (cm). The points correspond to analytical data and the line to the model results.

CHAPTER 4: PORE-SCALE MODELING OF HETERGENEOUS REACTIONS

4.1 Introduction

The scale dependence of reactive transport observed in natural samples has led to the development of reactive transport models across a wide range of spatial scales (Steefel et al., 2005). Field-scale models represent, for example, the natural length scale over which we would like to describe and understand the evolution of natural systems over long timescales (Pruess, 1991; Xu, 2003). However, a significant number of pore-scale parameterizations are involved in these models. For instance, dispersion tensors (and how they vary over space) and the correlation between porosity and permeability are constrained with simple empirical relationships or using a few available samples measured in the lab. The implicit spatial averaging in these large scale models (use of continuum descriptions, Darcy equation) smooth out any heterogeneity of a scale comparable or smaller than the representative elementary volume (grid-spacing) used in those models. Moreover, the averaging procedure can only be justified over at least hundreds to thousands of pore volumes to yield some significant statistics. Any heterogeneity and non-linear feedbacks that take place at the pore-scale is therefore lost in these descriptions, even though they are known to have an important role on the transport of reactant at much greater spatial scales, as exemplified by the disagreement between laboratory and field-site effective reaction rates.

As an alternative to these field-scale models, pore-network models were developed to include a better representation of pore-scale processes at the cost of simplified porous

media topologies (Blunt, 2001). Although these models have allowed us to gain a better perspective on the importance of spatial heterogeneities at a scale greater or equal to a single pore, they assume a regular geometric solid-fluid interface and they do not resolve chemical gradients within pores. Pore-scale reactions are therefore limited to assume batch reaction kinetics (Raoof and Hassanizadeh, 2010).

The complex interplay and non-linear coupling between surface reactions, flow and diffusive transport in an evolving porous medium (dissolution-precipitation) requires a pore-scale description and the ability to solve for the distribution of reactant inside pores. The advances in both computational power and the development of new numerical algorithms, have made possible pore-scale calculations including advection and diffusion of reactant in a solid matrix with a complex topology (Ginzburg, 2005; Huber et al., 2008; Kang et al., 2010; Kang et al., 2002). One of such numerical paradigm is the lattice Boltzmann method (LBM) that was developed as an extension to cellular automata models for fluid flows(Chen and Doolen, 1998; Frisch, 1987; Higuera and Jimenez, 1989; Qian et al., 1992). The LBM approaches mass and momentum conservation equations from a kinetic theory standpoint, where the macroscopic variables of interest, the local density (or pressure with an equation of state) and momentum of the fluid are retrieved from the statistical moments of particle distribution functions that follow the evolution of a discrete set of Boltzmann kinetic equations (see section 4.2 for more details). A number of studies have presented reactive transport models using the LBM, focusing on crystallization processes (Kang et al., 2004; Lu et al., 2009; Miller and Succi, 2002) and dissolution (Huber et al., 2008; Kang et al., 2002; Kelemen et al., 1995; Parmigiani et al., 2011; Walsh et al., 2009). Of direct interest to this study, Kang and co-

authors have presented, in a series of publications, a pore-scale transport model that allowed them to study heterogeneous and homogeneous chemical reactions (in both kinetic and equilibrium limits) and the dissolution of the solid matrix in response to these reactions (Kang et al., 2006, 2007; Kang et al., 2003; Kang et al., 2002). Their seminal work has highlighted, for example, the importance of the competition between diffusive and advective transport and the evolution of permeability during the dissolution of fracture walls of different sizes (Kang et al., 2006). The model we present here is losely inspired from the model of Kang et al., (2002) but is based on different approaches for the reactant transport (advection-diffusion model) and chemical reactions as well as a different algorithm for the update of the porous medium during dissolution and precipitation. Some of the novelties of our model are that the treatment of surface reaction is independent of the fluid-rock interface topology and orientation. The numerical model uses an iterative scheme for the chemical transport-reaction part and is therefore more accurate and stable for high reaction rates, moreover, it uses recent advances in the development of optimal advection-diffusion solvers within the lattice Boltzmann method framework.

4.2 Lattice Boltzmann Model For Pore-Scale Reactive Transport

4.2.1 Fluid Dynamics Solver

We use a traditional lattice Botzmann scheme for fluid dynamics in 2 dimensions (Chen and Doolen, 1998; Chopard, 1998; Succi, 2001). The flow of a single aqueous fluid phase in the pore space of a porous medium can be formulated by the following streaming equation:

$$f_{\propto}(\boldsymbol{x}+\boldsymbol{e}_{\propto}\delta t, t+\delta t) = f_{\propto}(\boldsymbol{x}, t) - \frac{f_{\propto}(\boldsymbol{x},t) - f_{\propto}^{eq}(\boldsymbol{x},t)}{\tau} \tag{4.1}$$

In this equation, δt is the time increment, $f_{\propto}$ the distribution function along the $\propto$ direction, $f_{\propto}^{eq}$ the equilibrium distribution function and τ the dimensionless relaxation time. The second term on the right had side of the equation is known as the collision term which is usually formulated by a single relaxation time operator (SRT or BGK collision). The distribution function $f_{\propto}(x,t)$ is updated using a discretized version of Boltzmann's kinetic equation. For the two-dimensional simulations, the distribution function is discretized in space and velocity domains where the motion of a particle is confined to 9 different velocity vectors (D2Q9). The discrete velocities $\boldsymbol{e}_{\propto}$ are shown in Figure 4.1b and have the following form:

$$\boldsymbol{e}_{\propto} = \begin{cases} 0, & \propto = 0 \\ \left(cos\frac{(\propto-1)\pi}{2}, sin\frac{(\propto-1)\pi}{2}\right)c, & \propto = 1-4 \\ \sqrt{2}\left[cos\left(\frac{(\propto-5)\pi}{2}+\frac{\pi}{4}\right), sin\left(\frac{(\propto-5)\pi}{2}+\frac{\pi}{4}\right)\right]c, & \propto = 5-8 \end{cases} \tag{4.2}$$

and $f_{\propto}^{eq}$ is given by

$$f_{\propto}^{eq}(\rho, \boldsymbol{u}) = w_{\propto}\rho + \rho s_{\propto}(\boldsymbol{u}) \tag{4.3}$$

where

$$s_{\propto}(\boldsymbol{u}) = w_{\propto}\left(\frac{3\boldsymbol{e}_{\propto}.\boldsymbol{u}}{c^2} + \frac{9(\boldsymbol{e}_{\propto}.\boldsymbol{u})^2}{2c^4} - \frac{3\boldsymbol{u}.\boldsymbol{u}}{2c^2}\right) \tag{4.4}$$

In the above equations,

$$c = \frac{\delta x}{\delta t} \tag{4.5}$$

where δx is the space increment and $w_{\propto}$ are weight coefficients with w_0=4/9, $w_{\propto}$=1/9 for $\propto$=1-4 and $w_{\propto}$=1/36 for $\propto$=5- 8. The macro properties of the fluid such as fluid density and velocity are calculated as:

$$\rho = \sum_{\propto} f_{\propto} \tag{4.6}$$

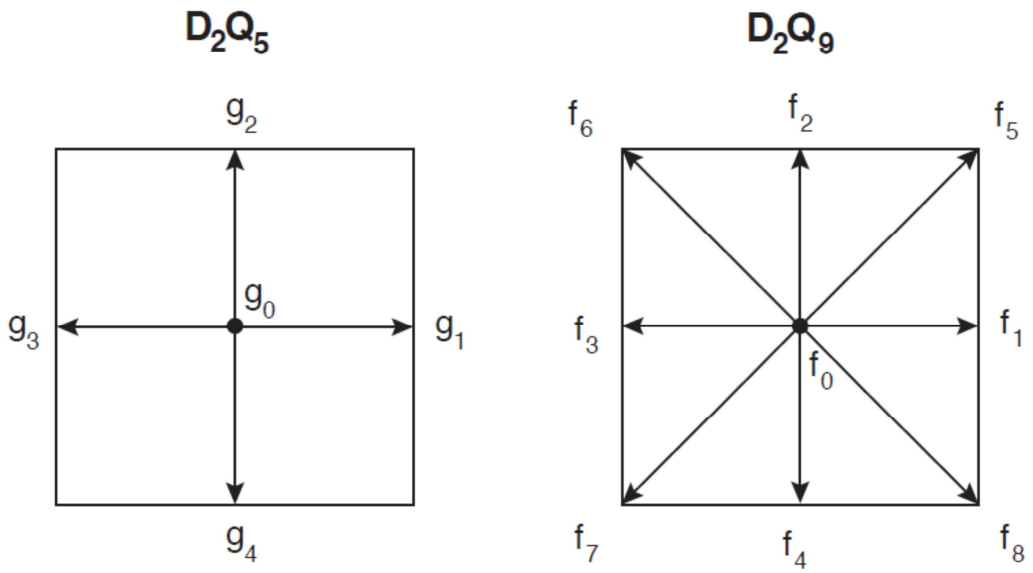

Figure 4-1: Lattice topologies and lattice velocity indexing for the D2Q5 (a) and D2Q9 (b) lattices.

$$\rho u = \sum_{\propto} \boldsymbol{e}_{\propto} f_{\propto} \tag{4.7}$$

In general representation of homogeneous chemical reactions in an aqueous phase we can have:

$$0 \leftrightarrow \sum_{k=1}^{N} \nu_{kr} A_k \,, \quad r = 1, \dots, N_R \tag{4.8}$$

where N is the total number of solute species, N_R is the number of reactions, A_k is the *kth* species and ν_{kr} is the stoichiometric coefficient. If the effect of concentrations of the aqueous species on the density and velocity of the solution is negligible, then another set of distribution functions, $g_{\propto k}$, can be used to describe the reactive transport of solute species which is similar to the streaming equation of $f_{\propto}$

$$g_{\propto k}(\boldsymbol{x}+\boldsymbol{e}_{\propto}\delta t, t+\delta t) = g_{\propto k}(\boldsymbol{x}, t) - \frac{g_{\propto k}(\boldsymbol{x},t) - g_{\propto k}^{eq}(C_k,\boldsymbol{u})}{\tau_k} + w_{\propto}\sum_{k=1}^{N_R}\nu_{kr}I_r \; k = 1, \ldots, N \quad (4.9)$$

where I_r is the rate of the *r*-th reaction, C_k is the solute concentration of the *k*-th species, τ_k is the relaxation time dependent on the diffusivity by

$$D_k = \frac{(\tau_k - 1/2)(\delta x)^2}{3\delta t} \quad (4.10)$$

for the D2Q9 lattice. $g_{\propto k}^{eq}$is the equilibrium distribution function of the *kth* species, written as:

$$g_{\propto}^{eq}(\rho, \boldsymbol{u}) = w_{\propto}C_k + C_k s_{\propto}(\boldsymbol{u}) \quad (4.11)$$

the concentration C_k is calculated in terms of the distribution function by the following equation:

$$C_k = \sum_{\propto} g_{\propto k} \quad (4.12)$$

Assuming the homogeneous reactions are fast enough that instantaneous equilibrium is reached, we apply the following mass action equations

$$C_i = (\gamma_i)^{-1}K_i\prod_{j=1}^{N_c}(\gamma_j C_j)^{\nu_{ji}} \quad (4.13)$$

where ν_{ji} are the stoichiometric coefficients, K_i is the equilibrium constant of the *i*-th homogeneous reaction, $\gamma_i$is the activity coefficient of the *i*-th secondary species and C_j and C_i are solute concentrations for primary and secondary species, respectively. They are related to Ψ_j, the total concentration of the *j*-th primary species by:

$$\Psi_j = C_j + \sum_{k=1}^{N_R}\nu_{ji}C_i \quad (4.14)$$

where N_R is the number of independent homogeneous reactions. By applying the canonical form of the homogeneous reactions as below

$$G_{\propto j}(\boldsymbol{x}+\boldsymbol{e}_{\propto}, t+\delta t) = G_{\propto j}(\boldsymbol{x}, t) - \frac{G_{\propto j}(\boldsymbol{x},t) - G_{\propto j}^{eq}(\Psi_j,\boldsymbol{u})}{\tau_{aq}} \quad (4.15)$$

and formulating a LB equation for total concentration Ψ_j and replacing the rates of these reactions with mass action equations, the number of unknowns and streaming equations is reduced from $N_C + N_R$ to N_C. In the above equation $j = 1, \dots, N_C$, and $G_{\propto j}$ is the corresponding distribution function along the $\propto$ direction, $G_{\propto j}^{eq}$ is its equilibrium distribution function and τ_{aq} is the dimensionless relaxation time used for all the aqueous species. For the D2Q5 model (see Figure 4.1a) where 5 different velocities are assigned for fluid particles, the equilibrium distribution defined as the following linear form:

$$G_{\propto j}^{eq} = \frac{\Psi_j}{4} + \frac{\Psi_j}{2c^2}(\boldsymbol{e}_{\propto}.\boldsymbol{u}) \tag{4.16}$$

with

$$\boldsymbol{e}_{\propto} = \left(cos\frac{(\propto-1)\pi}{2}, sin\frac{(\propto-1)\pi}{2}\right)c, \qquad \propto = 1-4 \tag{4.17}$$

The simplicity of the lattice Boltzmann algorithm for fluid dynamics offers a simple and elegant way to handle no-slip solid-fluid boundary conditions on complex geometries. This proves to be extremely useful for solving fluid flows at the pore-scale in porous media (Huber et al., 2008; Kang et al., 2002; Parmigiani et al., 2011; Succi, 2001).

We use the standard method to implement no-slip interfaces, the bounce-back of the distribution at a solid wall. The method is illustrated in Figure 4.2a, and although it is only 1st order in space it offers a great flexibility, especially when dealing with a solid matrix that can evolve with time (dissolution or precipitation). In the bounce-back method, the local distribution functions are reflected in opposite direction:

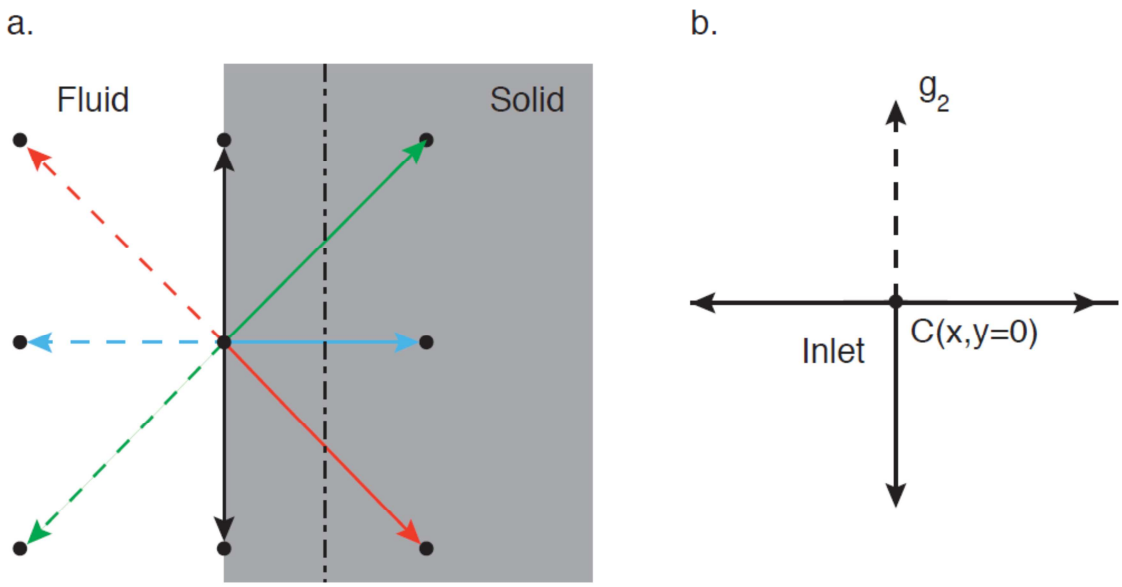

Figure 4-2: (a) Schematic illustration of the bounce-back boundary condition at fluid-solid interfaces. The real and effective (numerical) boundaries are shifted by half a node for a straight interface (1st order accuracy). (b) Dirichlet boundary condition (imposed con- centration) at the south margin of the domain, the missing distribution g_2 is represented with a dashed line.

$$f_{\propto} = f_{\overline{\propto}}$$

where $\overline{\propto}$ is the direction opposed to $\propto$, for example $f_4 = f_{\overline{2}}$. The final requirement to solve for a fluid flow in the porous medium is to impose external flow boundary conditions, here we will use a gravity-driven flow, but pressure-driven flows could have been implemented as easily by using the proper boundary condition (Zou and He, 1997). We assume periodic boundary conditions around the porous medium and the body force (gravity) is added as a source term in the collision term of Equation (4.1). The fluid dynamics scheme presented here is equivalent to the flow model of Kang et al., (2002).

The two models differ with respect to the advection-diffusion scheme for chemical species and the model for heterogeneous reactions at fluid-solid interfaces.

4.2.2 Advection-Diffusion Scheme For Chemical Species

Similarly to Kang et al., (2002) we introduce the advection-diffusion (and reaction see below) equation for solute transport through the addition of a second particle distribution function g. Using a similar approach as for the fluid solver, the evolution of the particle distribution function g is discretized in time and over space and velocity domains, using, this time, a five velocity lattice (D2Q5, see Figure 4.1a). The lattice direction vectors $\boldsymbol{e}_{\propto}$ are given by Equation (4.17).

We use a different lattice for the advection-diffusion scheme, because of the difference in number of conservation equations between the fluid solver (three in 2-D) and the chemical transport solver (one, mass of the chemical component), the latter requires less symmetry. Kang et al. (2002) used a four velocity lattice (no rest velocity), and as will be discussed below, the two approaches for both chemical transport and reactions are very different. For instance, Kang et al. (2002) implemented the advection-diffusion equation with the distribution g similarly to what we implement for Navier-Stokes equations. In other words they introduced another discrete Boltzmann equation with a single relaxation time operator (SRT or BGK) that, with the proper set of equilibrium distribution and using $C(x,t) = \sum_{\propto} g_{\propto}(x,t)$, leads to, after a Chapmamn-Enskog expansion:

$$\frac{\partial C}{\partial t} + u.\nabla C = \nabla.(D\nabla C) \tag{4.18}$$

where D is described by Equation (4.10). This model has been used extensively by several authors for advection-diffusion equations (Ginzburg, 2005; Ginzburg et al., 2010;

Huber et al., 2008; Parmigiani et al., 2011; Servan-Camas and Tsai, 2008; Suga, 2006; Wolf-Gladrow, 2000). The stability of the SRT model depends on the value of the grid Peclet number $Pe_g = u\delta x/D$ and on the geometry of the porous medium (i.e. gradients in Pe_g) (Ginzburg, 2005; Ginzburg et al., 2010; Stiebler et al., 2008). They have shown that a multiple relaxation time (here two relaxation times or TRT) approach for the collision operator yields a better stability and accuracy, especially when the grid Peclet number increases to values of the order of one or above. For this reason, we decided to use the optimal TRT collision operator defined by Ginzburg (2005) and used successfully by Stiebler et al. (2008) over a wide range of Peclet numbers. Detailed information on the optimal TRT model for the advection-diffusion equation has been described in the literature (Ginzburg, 2005; Ginzburg et al., 2010). The advantage of the method is that two free parameters are available to tune the performance of the advection-diffusion solver, instead of a single one with the SRT. As discussed by Ginzburg et al. (2010), there is an optimal choice for these two parameters λ_1 and λ_2

$$(\lambda_1, \lambda_2) = \left(3 - \sqrt{3}, \frac{6\sqrt{3}D}{c^2\delta t} - 1\right) \tag{4.19}$$

with $c = \frac{\delta x}{\delta t}$ and D the diffusion coefficient of the chemical species of interest. With this optimal TRT model, the collision reduces to a similar description as for the SRT

$$g_\alpha(x + e_\alpha\delta t, t + \delta t) = g_\alpha(x,t) - \lambda_1\left(g_\alpha(x,t) - g_\alpha^0(x,t)\right) + \Psi(x,t)_\alpha \tag{4.20}$$

where Ψ is a source/sink term associated with chemical reactions (see next section) and the equilibrium distribution is

$$g_\alpha^0(x,t) = C(x,t)\left(t_\alpha + \frac{1}{3}\lambda_2 t_\alpha^e + E_\alpha^u + \frac{1}{2}\frac{\boldsymbol{u}.e_\alpha}{c^2}\right) \tag{4.21}$$

with

$$\boldsymbol{t}_{\propto} = \begin{cases} \frac{1}{3} & \alpha = 0 \\ \frac{1}{6} & \alpha \neq 0 \end{cases} \tag{4.22}$$

$$t_{\alpha}^{e} = \begin{cases} -2 & \alpha = 0 \\ \frac{1}{2} & \alpha \neq 0 \end{cases} \tag{4.23}$$

And finally

$$E_{\alpha}^{u} = \begin{cases} -\frac{\boldsymbol{u}.\boldsymbol{u}}{c^2} & \alpha = 0 \\ \frac{1}{2}\frac{(\boldsymbol{u}.e_{\alpha})^2}{c^4} & \alpha \neq 0 \end{cases} \tag{4.24}$$

In all the calculations above, Dirichlet (fixed concentration), Neumann(fixed flux) or periodic boundary conditions are applied at the edges of the computational domain. We fix a concentration at the inlet of the domain *y = 0* (see Fig 4.2b) by adjusting the missing part of the distribution function *g* (here g_2) so as to impose a concentration C_{inlet}

$$g_2(x, y = 0, t) = C_{inlet} - [g_0(x, y = 0, t) + g_1(x, y = 0, t) + g_3(x, y = 0, t) + g_4(x, y = 0, t)] \tag{4.25}$$

For Neumann boundary conditions of the type $\frac{\partial C}{\partial y} = 0$ (here at the outlet *y = L*), we use a second order finite difference scheme to determine the missing distribution

$$g_4(x, y = L, t) = \frac{4}{3}C(x, L - \delta x, t) - \frac{1}{3}C(x, L - 2\delta x, t) - [g_0(x, y = L, t) + g_1(x, y = L, t) + g_2(x, y = L, t) + g_3(x, y = L, t)] \tag{4.26}$$

4.2.3 Heterogeneous Reactions

In the pore-scale model of Kang et al. 2002, heterogeneous reactions are introduced as internal boundary conditions. In other words, the solid-fluid interfaces are not part of the computational domain explicitly, but different set of rules is implemented at each interface depending on the geometry of the interface (e.g. orientation of the normal to the

plane of the interface pointing in different directions, corner versus flat interface). This approach is intuitive in that the microscopic mass balance is described explicitly at each interface but requires an important amount of book-keeping or additional calculations to (1) classify each type of fluid-solid interface in terms of the unknown distribution g_α coming from the solid site and (2) update fluid or solid sites during dissolution or precipitation.

We present a new model of heterogeneous reactions based on the phase-field method to overcome the two issues listed above. Our approach is to treat the internal interfaces (solid-fluid boundaries) as part of the computational domain and solve a similar TRT-LB scheme at these particular sites. The phase-field method we propose allows us to treat any type of internal boundary identically (corner or flat, with normal pointing to any direction) and in a similar way as any fluid site (advection-diffusion equation) in the computational domain. It will also prove convenient when dealing with time-dependent changes in matrix topology associated with precipitation and dissolution (discussed below).

The main conceptual idea in the phase-field method is to add a scalar variable (continuous) $\epsilon(x,t)$ that becomes a flag variable for the advection diffusion and reaction scheme. For instance, we decide to define $\epsilon(x,t)$ to be the local fluid fraction at each site, initially ϵ is a binary variable with values 0 for solid sites and 1 for fluid sites. We will first discuss the method for surface reactions that do not involve any change in porosity (no precipitation nor dissolution), i.e. $\epsilon(x,t) = \epsilon(x,0)$. The reaction term in equation for the TRT collision model becomes

$$\Psi(x,t)_\alpha = w_{G;\alpha} M k C_0 \left(\frac{C}{C_0} - 1\right)^m \frac{S(x,t)}{v} \tag{4.27}$$

where $w_{G;\alpha}$are the lattice weights along each direction e_α. $M = w_f\rho_f/w_s\rho_s$ is the mass ratio with the w_α and ρ_α respectively the mass fraction of the chemical species *C* in and the density of phase $\alpha =$ fluid and solid. The reaction rate is k, C_0 is the equilibrium concentration(here assumed to be different than 0) and m is the order of the reaction. The last term $\frac{S(x,t)}{v}$ is the surface area of the interface to volume ratio of the lattice node considered. This ratio is defined at the pore-scale to be

$$\frac{S(x,t)}{v} = \begin{cases} \delta x^{-1} & \text{if } \epsilon(x,t) = 0 \text{ and there is one or more } \alpha \text{ such that } \epsilon(x+e_\alpha,t) = 1 \\ 0 & \text{otherwise} \end{cases} \quad (4.28)$$

We note that, although not within the scope of the present study, it is easy to introduce surface roughness (even a time-dependent evolution of roughness) in the scope of our reaction model. After a Chapman-Enskog expansion, our model yields the advection-diffusion-reaction model of Equation (4.18) with the following mass balance at the solid-fluid interface:

$$D\nabla_n C = MkC_0\left(\frac{C}{C_0} - 1\right)^m \quad (4.29)$$

Note that although the advection-diffusion-reaction equations are identical to Kang et al. (2002), the solid-fluid interfaces are not treated as boundary conditions in our model and our algorithm involves the exact same treatment at all points in the computational domain, irrespective to the presence of internal boundaries and especially irrespective to their orientation and shape. In this new model, there is, at this stage, nothing to prevent *C* from diffusing in the solid. Two simple options can be used to tune the rate of solid diffusion: (1) if a finite amount of solid diffusion is expected, λ_2 can be

varied spatially to a different value on solid nodes ($\epsilon(x) = 0$) so as to obtain a different diffusion coefficient or (2), when diffusion in the solid is negligible, the bounce-back condition for all g_α can be used for all sites such that $\epsilon(x) = 0$ and $\epsilon(x + e_\alpha) = 0$ for all lattice directions e_α.

When treating solid-fluid internal interfaces as boundary conditions, time-dependent interface topologies become challenging and requires solving for the mass conservation of solid phases that are not part of the computational domain. For instance during dissolution, a solid node is removed and it is converted to a fluid node, the change in internal boundary condition needs to properly account for mass balance at subsequent iterations. The complexity of the solid-fluid node update is more obvious in the case of precipitation. Kang et al. (2002) developed a scheme where once the mass of solid at a pre-existing solid node (an internal boundary node) exceeds a threshold value (they typically used a value that corresponds to twice the mass of a solid node), then a neighbor fluid node is randomly selected and precipitates, i.e. becomes a new solid node-new boundary node that is no longer part of the computational domain. The stochastic process they propose consists of adding a node in the North-South-East-West direction with a probability significantly greater than along a diagonal of the square lattice Kang et al. (2006). In that sense, the precipitation is transported randomly from a boundary node to a neighbor node as an update of the structure of the porous medium.

We propose to use the phase-field method to our advantage and consider that the reaction takes place at the solid side of a solid-fluid interface for dissolution and the fluid side for precipitation (see Figure 4.3). The approach proposed for precipitation and dissolution is purely local and does not require external decision or random selection of

adjacent nodes during the reaction process and, again, does not depend on the topology of the interface. The dissolution-precipitation algorithm follows the reaction model discussed above and becomes for all sites in the computational domain (solid or fluid nodes)

$$g_\alpha(x + e_\alpha \delta t, t + \delta t) = g_\alpha(x,t) - \lambda_1\big(g_\alpha(x,t) - g_\alpha^0(x,t)\big) + \xi(x,t)\Psi(x,t)_\alpha \qquad (4.30)$$

where

$$\xi(x,t) = \begin{cases} -1 & \epsilon(x,t) < 1 \text{ and there is one or more } \alpha \text{ such that } \epsilon(x + e_\alpha, t) = 1 \\ -1 & \epsilon(x,t) > 0 \text{ and there is one or more } \alpha \text{ such that } \epsilon(x + e_\alpha, t) = 0 \\ 0 & \text{otherwise} \end{cases} \qquad (4.31)$$

The first choice above accounts for dissolution and the second for precipitation, the sign of the source/sink term in Equation (4.30) changes from positive for dissolution (undersaturated) to negative for precipitation (supersatured solution) because of the sign of (C/C_0-1) in Ψ. The local fluid fraction ϵ is updated at each time step

$$\epsilon(x,t) = \epsilon(x, t - \Delta t) + \Delta t \xi(x,t)\Psi(x,t)_\alpha \qquad (4.32)$$

because $0 \leq \epsilon \leq 1$, we make sure that local changes in fluid fraction do not overshoot these bounds during calculations. During dissolution, some solid sites are switched to fluid site and we initialize them in the flow calculation with the equilibrium distribution $f_\alpha^{eq}(\rho = \rho_f, \boldsymbol{u} = 0)$. Similarly new solid sites become bounce-back boundaries in the flow calculations.

The presence of heterogeneous reactions (linear or non-linear) into an explicit advection-diffusion model like Kang et al. (2006) or the one proposed here can lead to limited accuracy and numerical instabilities. We therefor introduce an iterative procedure to solve accurately the mass balance between chemical transport and surface reactions. In

the present model, the coupling between dissolution/precipitation and the changing flow field is considered slow enough to keep the flow solver out of the iterative procedure. Figure 4.4 shows a flow-chart diagram to illustrate how the proposed numerical model works and how the different parts (flow field and chemical transport and reaction) are coupled. We refer the readers interested in the iterative procedure with a (different) phase-field approach to the advection-diffusion LB model to Huber et al. (2008) for more details on the solution procedure. In this model, convergence of the local dissolved concentration field and the new local fluid fraction are both required to proceed to the next time-step. The iterative procedure offers stability and accuracy over a wider range of Damkohler number $Da = k\delta/D$, where δ is a characteristic length scale (here we will use the average pore-diameter) as well as a wider range of Pe_g.

One particular type of reactions of interest for this study are surface sorption reactions (here sorption is used for both adsorption and desorption). This particular type of surface reactions are non-linear, as they depend both on the availability of sorption sites and concentration of reactant on the surfaces (noted F^i, for p solid phases here) and the concentration of dissolved species that can be adsorbed next to the interface (here will keep C for the dissolved species). We assume a simple set of p forward and backward sorption reactions of the type

$$C_{(aq)} + F^i_{[s]} \underset{k_{d1}}{\overset{k_1}{\leftrightarrows}} CF^i_{[s]} \qquad i = 1,2,\dots p \tag{4.33}$$

Here the concentrations of solid species are given in moles per gram and for the dissolved species in moles per volume. We use a Langmuir model to describe each of the p sorption reaction where the evolution of the solid phase concentration on sorption sites follows:

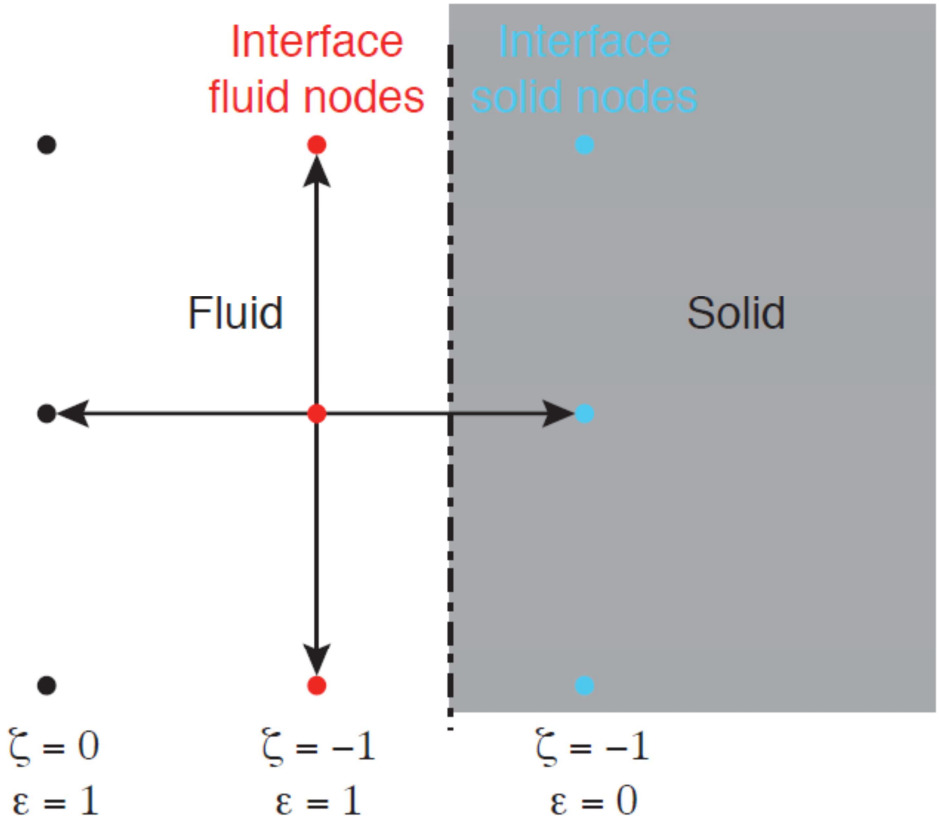

Figure 4-3: Phase-field approach to surface reactions. Interface fluid nodes are considered for precipitation and interface solid nodes for dissolution. We use two flag variables, the first one is ϵ which corresponds to the type of nodes (solid or fluid dominated) and the second ξ which is null for all site but interface nodes where they can be ±1 depending on the location with respect to the fluid-solid interface.

$$\frac{\partial CF_{[s]}^{i}}{\partial t} = \frac{k_i}{\rho_s}\left(CF_{[s]}^{i,max} - CF_{[s]}^{i}\right)C_{(aq)} - k_{dj}CF_{[s]}^{i} \tag{4.34}$$

with

$$CF_{[s]}^{i,max}(x,t) = CF_{[s]}^{i}(x,t=0)S_A S_D M_{w,F^i} \tag{4.35}$$

where S_A is the initial surface area per grams of solid species F^i, S_D is the site density (in mol/m^2) and finally M_{w,F^i} is the molecular weight of the solid species F^i. Equation (4.34) describes a non-linear heterogeneous reaction. Empirical sorption conceptual models such as Langmuir equation are easy to implement in reactive transport models and provide straightforward tools to compare the experimental results with simulated ones. However, it has been shown that empirical laws are not as robust as surface complexation models (SCMs) and do not describe ion sorption processes in a mechanistic way. In fact surface complexation models are chemical models that account for electrostatic effects arising from changes in charge on sorbing surface and based on different assumption of surface charge potential, various types of SCMs have been developed (Goldberg et al., 2007; Zhang and Selim, 2008). SCMs can account for factors such as ion strength and fluid pH. Therefore in order to apply SCM a multi-species reactive transport model should be used which will be the focus of a future study. During the sorption process, we neglect the changes in porous geometry and the porosity remains the same throughout all calculations. Our reaction model can easily be applied to sorption reactions.

In summary, the model we propose for heterogeneous reactions during the pore-scale transport of reactant is inspired from the seminal work of Kang et al. (2002). However, the design of the advection-diffusion solver and the surface reactions are handled with significant differences. First of all, the advection-diffusion scheme we developed is based on the optimal two relaxation times (TRT) model proposed by

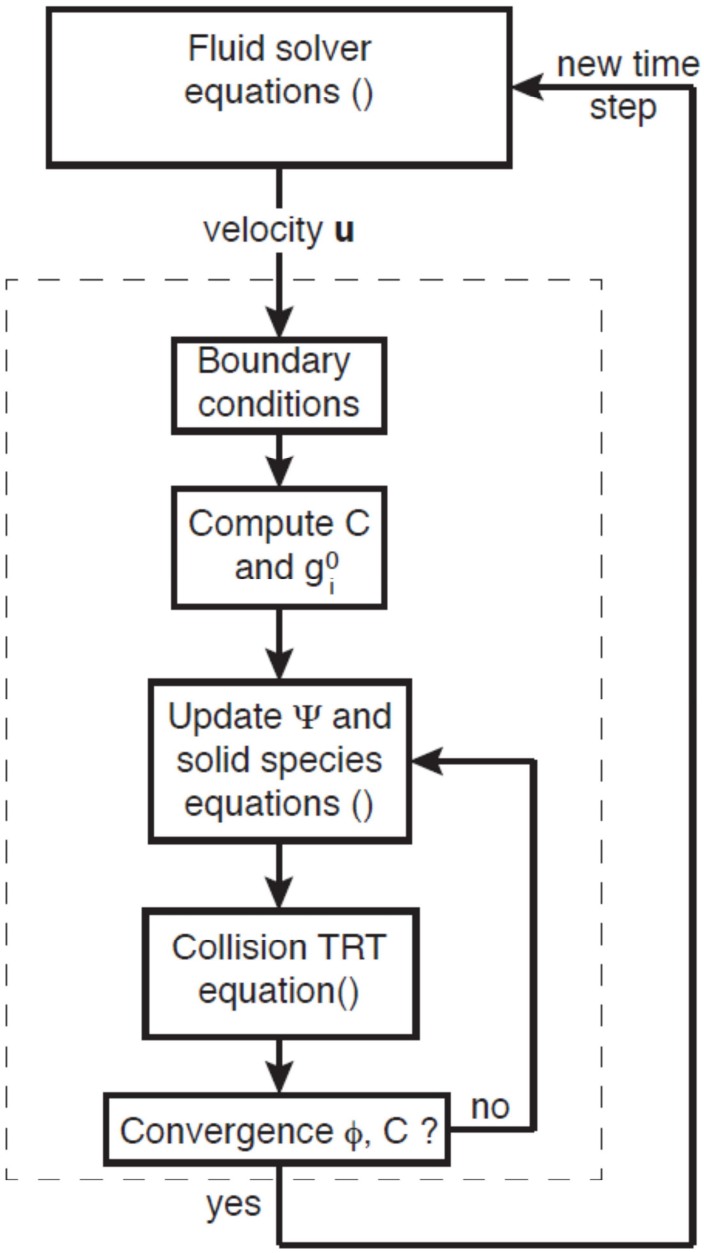

Figure 4-4: Flow chart for the reactive model algorithm.

Ginzburg (2005), whereas a single relaxation time model (SRT) was used by Kang and co-authors. Although both models have been shown to yield accurate results in most circumstances, the TRT model offers more flexibility (two tuning parameters instead of a single one). Ginzburg et al. (2010) showed that the presence of the extra free parameter can be used to find an optimal solution in terms of accuracy and stability of the advection-diffusion scheme over a greater range of Pe_g. The second major difference concerns the heterogeneous reactions. In Kang's model they are treated as internal boundary conditions, i.e. solid interfaces are not part of the computational domain, this causes the treatment of surface reaction to be (1) site specific (depends on the orientation of the surface, if it is a corner) and (2) as solid sites are not part of the computational domain, during precipitation the evolution of fluid site is not local (depends on the mass balance of neighbor solid sites) and introduces a stochastic updating procedure. We propose a model where solid-fluid interface sites are part of computational domain and follow a similar evolution rule to the other fluid sites. The reaction is introduced as a source-sink in the collision operator, this allows the model to remain local, even for dissolution or precipitation reactions, and the implementation of the reaction is independent of the topology of the solid-fluid interface. Lastly, lattice-Boltzmann models are intrinsically explicit, we introduced an iterative solution procedure for the transport and reaction of the dissolved reactant to extend the range of stable and accurate conditions under which to model can be used. The model of Kang et al. (2002) has been highly successful, the major modifications discussed here are motivated by the desire to extend the applicability and flexibility of the model with a different approach. We note that although they also treat homogeneous reactions, these are not part of the present

study, but an approach similar to theirs for homogeneous reactions can be introduced easily in our model. The differences between the two models are summarized in Table 4.1.

4.3 Validation

The choice of an optimal TRT model for the solute transport is different from standard multiphysics lattice Boltzmann approaches (Kang et al., 2002; Zhang et al., 2008a). In this section, we proceed with three tests to validate the method for (1) the transport of solutes (in 1-D) and (2) the coupled diffusion-reaction part of the model in 2-D. We first test the TRT solute transport model against an analytical solution for a purely 1-D diffusive transport problem with no chemical reaction. We assume that the concentration of solute is $C = 0$ initially and impose $C = 1$ at the left boundary for $t > 0$. The analytical solution for this problem is given by

$$C(x,t) = erfc\left(\frac{x}{2\sqrt{Dt}}\right) \tag{4.36}$$

and it is plotted against the results from the numerical model in panel (a) of Figure 4.5.

Table 4-1: Comparison between the model of Kang et al. and the model presented by Huber et al. (2012). *a*: AD=advection-diffusion. *b*: BC=boundary condition.

	Kang et al. (2002)	Huber et al. (2012)
Flow solver	SRT-LB	Same
AD solver [a]	SRT-explicit	TRT model-iterative
Reaction solver	Site specific BC [b]	Independent of site

An advantage of the optimal TRT model over standard SRT models is its ability to model advection-diffusion processes with greater accuracy and stability especially for high grid Peclet number. We illustrate the ability of our transport model to accurately solve for a 1-D advection-diffusion of a gaussian concentration distribution for conditions in which Pe_g = 200 and compare the numerical results with the analytical solution (Figure 4.5b)

$$C(x,t) = exp\left(-\frac{(x-Ut)^2}{2(\sigma^2+Dt)}\right)\frac{\sigma^2}{2(\sigma^2+Dt)} \tag{4.37}$$

where σ is the initial width of the gaussian distribution, U the velocity and D the diffusion coefficient. We observe a very good agreement in terms of the position and spread of the distribution, as well as the amplitude of the peak in concentration. Analytical solutions are difficult to find for 2-D advection-diffusion equations with reactions. We use the same benchmark problem as Kang et al. (2006) to test our reactive transport model. In this example, the transport of the chemical species is due to diffusion alone. A rectangle enclosure with an initial uniform concentration C_{eq} = 1 is subjected to a fixed concentration C_b = 10 left boundary (at x = 0, see Figure 4.6a) and no flux conditions at the bottom (y = 0) and right ($x = L_x$) boundaries. At the upper boundary $y = L_y$, a linear reaction is imposed with reaction rate k

$$-D\frac{\partial C}{\partial y} = k\left(C_b - C_{eq}\right) \tag{4.38}$$

with $C_b = C(x; y = L_y)$. The analytical solution to this problem is given by (Carlsaw, 1959; Kang et al., 2006):

$$C(x,y) = \left(C_0 - C_{eq}\right)\sum_{n=1}^{\infty}\frac{\sin(\beta_n L_y)}{N_n^2\beta_n}\frac{\cosh[\beta_n(x-L_x)]}{\cosh(\beta_n L_x)}\cos(\beta_n y) + C_{eq} \tag{4.39}$$

with

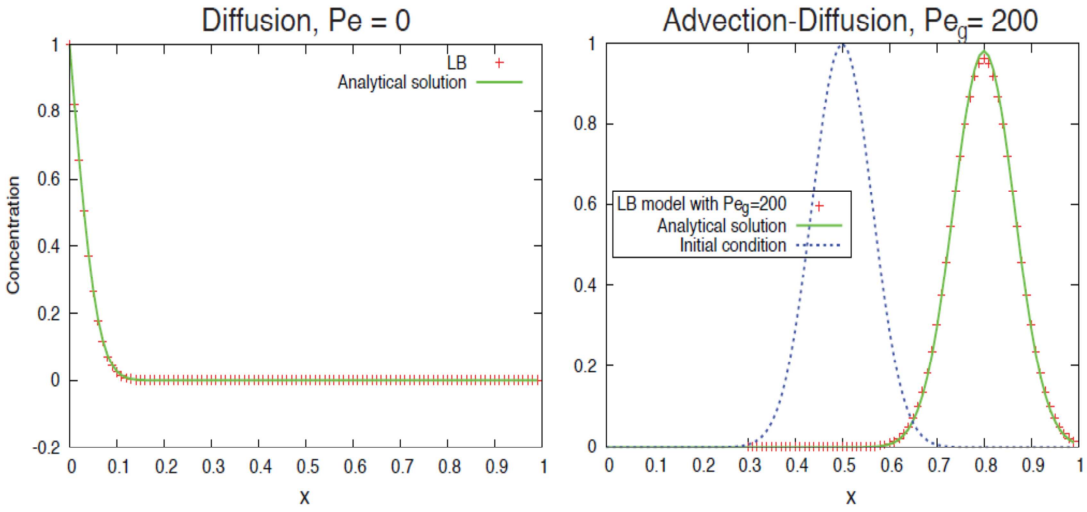

Figure 4-5: Comparison between our LB model for solute transport and analytical solutions for (a) diffusion only and (b) advection and diffusion with $Pe_g = U\Delta x/D$

$$N_n^2 = \frac{b}{2}\left(1 + \frac{\sin(2\beta_n L_y)}{2\beta_n L_y}\right) \tag{4.40}$$

And the β_n's are the solution of

$$(\beta_n L_y)\tan(\beta_n L_y) = \frac{kL_y}{D} \tag{4.41}$$

We truncated the infinite sum of the analytical solution to the 10th term, which explains the oscillations of the contours at low x and high *y* in Figure 4.6b. We fixed L_x = 100 and L_y = 80 in our calculations and the ratio $\frac{kL_y}{D}$ was fixed to 48 similarly to Kang et al. (2006). Even with a low spatial resolution and after truncating the analytical solution to the first 10 terms, there is an excellent agreement between the numerical and analytical results.

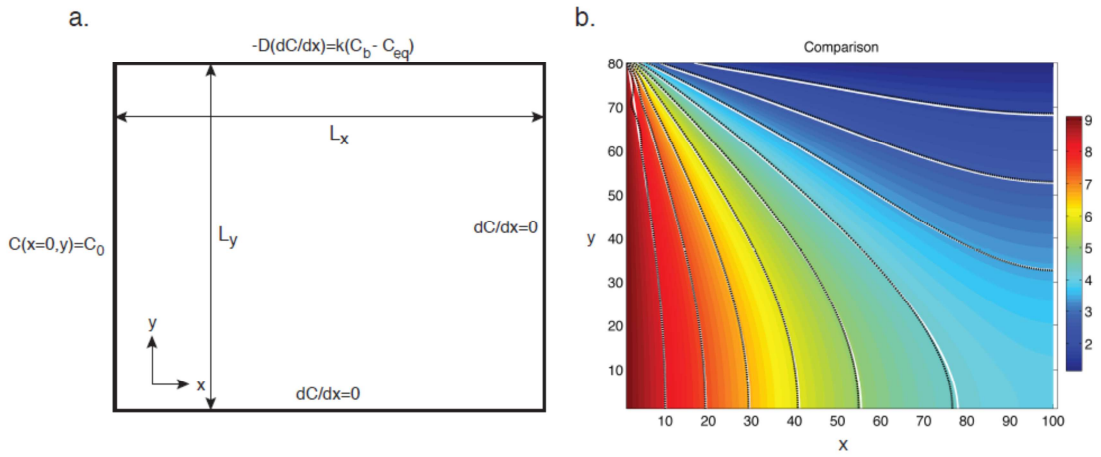

Figure 4-6: Reaction-diffusion benchmark used for the validation of the reactive model. A rectangular enclosure with initial concentration C_{eq} is subjected to a fixed concentration $C_b > C_{eq}$, the south and east borders are zero flux boundaries and the north border is a linear reaction (sink). (a) The geometry and notation for the benchmark calculation. (b) Steady-state results compared with the analytical solution.

4.4 Results

The calculations conducted in this study are divided into two separate sections. We present results for the dissolution and precipitation of a porous medium under different dynamical conditions, varying reaction rates and the ratio of advective to diffusive transport (Peclet number) for linear reactions. We focus on the effect of a given porosity change on the permeability of an identical porous structure subjected to different dissolution and precipitation conditions. We also compare the results for linear reactions to second order dissolution or precipitation reactions. The final set of calculations considers sorption reactions on a heterogeneous porous medium. We used our model to investigate the effect of heterogeneity on the pore-scale distribution of sorption sites and the competition between three different sorption reactions ($p = 3$ in Equation 4.33).

4.4.1 Precipitation And Dissolution

Dissolution and precipitation during reactive transport feeds back into the reactive transport process by changing the flow boundary conditions and affecting the mass exchange of chemical components at the solid-fluid interface at the pore-scale. Significant temporal changes in porosity are expected to take place in coastal aquifers, resulting from the mixing of fresh and seawater, or in hydrothermal regions (Rezaei et al., 2005; Sanford and Konikow, 1989; White and Mroczek, 1998). Macroscale models, based on Darcy transport equations, have been developed to study more explicitly the feedback between advective transport of reactants and heterogeneous porosity changes (Bolton et al., 1996, 1997; Chen and Ortoleva, 1990; Le Gallo et al., 1998; Steefel and Lasaga, 1990, 1994; Steefel and Maher, 2009; Walsh et al., 2008).

A famous example of such positive feedback between flow and dissolution is the development of wormhole structures that enhances the flow and therefore yield a greater flux of reactant to regions affected by dissolution (Liu et al., 1997; Ormond and Ortoleva, 2000). As Kang et al. (2003) showed, there is an important dynamical control on how a change in porosity translated into a change in permeability during dissolution or precipitation. Pore-scale calculations are necessary to investigate the non-linear permeability response to porosity changes, and even if several pore network models have been designed to address this question, their inability to solve for chemical gradients inside pores and their simplified pore and throat geometry does not provide a realistic treatment of the process. Pore-scale calculations are therefore required to gain a better and more quantitative insight into the porosity-permeability correlation under a range of dynamical conditions (different reaction rates and ratio of advective to diffusive transport), similarly to the study of Kang and co-workers, we investigate the feedback between porosity change and permeability as function of two dimensionless numbers, the Peclet number *Pe* and the Damkholer number *Da*

$$Pe = \frac{u_d \delta}{D} \tag{4.42}$$

and

$$Da = \frac{k\delta}{D} \tag{4.43}$$

where u_d is the discharge through the porous medium (Darcy velocity), D the molecular diffusivity of the dissolved reactant in the fluid, k the reaction rate (either dissolution or precipitation). Finally, δ is the characteristic length scale we select to represent the competition between the different transport modes and reaction. We fixed δ to be the

average initial pore diameter in the sample. This decision is motivated by the pore-scale nature of our calculation and justified by the fact that the transient behavior of the problem is controlled by the geometry of the pores rather than the length of the porous media slab that is used in the calculation. We note however that this definition is different from most studies. The porous medium we used for all the precipitation and dissolution calculations was constructed numerically from a nucleation and growth algorithm based on Avrami's model (Avrami, 1941; Hersum and Marsh, 2006; Parmigiani et al., 2011). It allows us to build a porous medium out of a heterogeneous and polydisperse distribution of pseudo-cuboid particles. In a first time, the texture is fully crystallized (porosity = 0) and we remove the latest crystallized phases to obtain the desired porosity, see Figure 4.7.We started with a (high) porosity of 0.7989 in our sample; the dimension of the computational domain is 320 nodes along the flow direction and 250 nodes perpendicular values of grid Peclet numbers (see below). The flow is again buoyancy-driven (body force), but could have been set with a prescribed pressure gradient similarly. A test on the effect of buoyancy versus pressure-driven flow on dissolution-precipitation is beyond the scope of this study, but we plan on exploring it in the near future. At the bottom of the domain (see Figure 4.7), a fixed concentration C_b is prescribed and the top boundary is a no-flux boundary condition, lateral boundaries are assumed periodic. We conducted 140 different calculations, 70 each for dissolution and precipitation. The first calculations focused on the evolution of the porous medium under different sets of (*Pe*;*Da*) for first order dissolution or precipitation reactions. We used $Pe \in \{01; 0:02; 0:05; 0:1; 0:3\}$ and $Da \in \{0:2; 0:5; 1; 2; 5; 10; 20\}$. We note that, although the maximum imposed $Pe = 0.3 < 1$ in these calculations, the maximum grid Peclet number Pe_g is of the order of 10, which

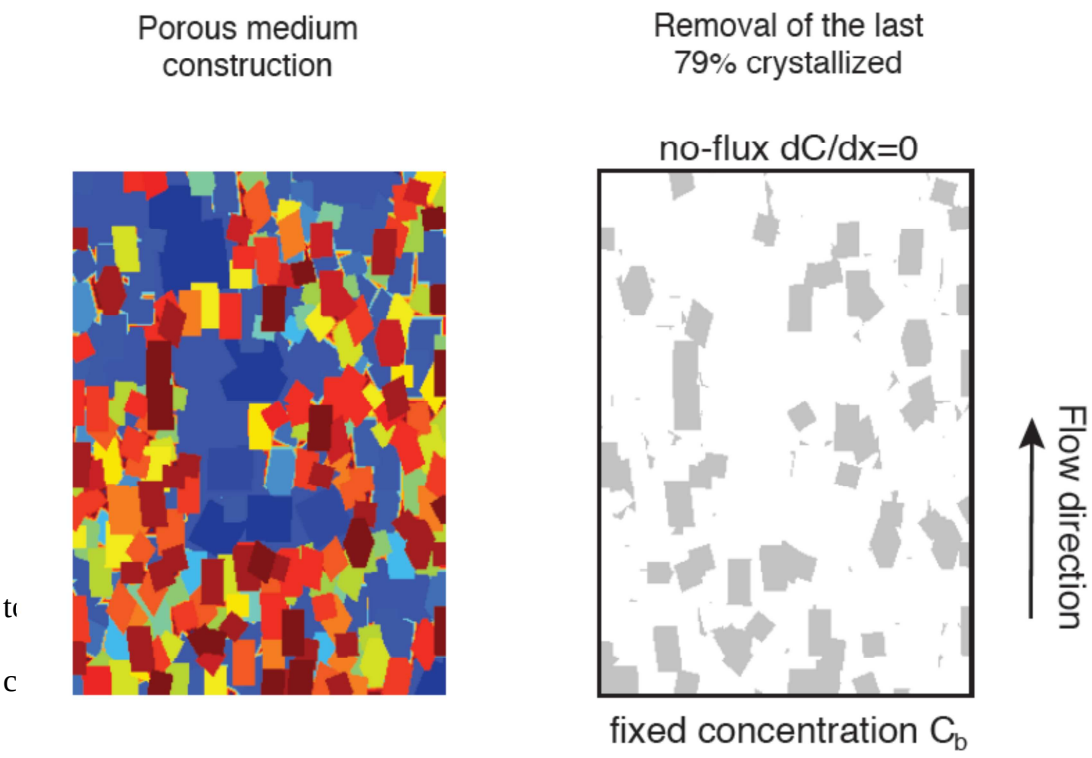

Figure 4-7: The topology of the porous medium used for all dissolution and precipitation calculations. On the right side panel, the gray shaded areas correspond to the solid fraction of the porous medium.

is large and requires an efficient advection-diffusion (and reaction) solver and justifies our choice of algorithm for the complex geometries studied here. Snapshots of evolution of the flow and chemical transport are shown in Figure 4.8, for different *Pe* and *Da* numbers using first order reactions. Each set of two columns represents a few snapshots over time of the evolution of the advective transport (magnitude of the velocity field) on the left and concentration of dissolved reactant on the right. The solid fraction is shown in grey and the changes in porosity can be clearly observed next to the bottom boundary (inlet). Each snapshot was taken at times where the change of overall porosity $\Delta\varphi$ reached 1, 2 or 5%.

In each calculation, the choice of (*Pe;Da*) controls the time it takes to reach a given $\Delta\varphi$. In order to remove this effect, we decided to consider how permeability varies with porosity, rather than with time. This puts all calculations on equal footing and allows us to compare the efficiency of the positive (dissolution) or negative (precipitation) feedback between flow and reaction. In Figure 4.9, we show some examples of calculations for dissolution and precipitation. The effect of the Peclet number at fixed *Da*= 2, is shown in Figure 4.9a-b, we observe that a more efficient advective transport (greater *Pe*) translates into a greater effect on permeability than diffusion dominated regimes. This is not surprising as advection tends to increase the flux of reactant to the main flow pathways, as a result most of the reaction will affect the region that is the most sensitive to the flow discharge, and hence to the porous medium permeability. We observe that for first-order reactions, over the range of *Pe* studied, here an increase in porosity of 2%, leads to up to a 50 % increase in permeability. What is more remarkable, is that precipitation is much more sensitive to porosity changes, after a few percents, the

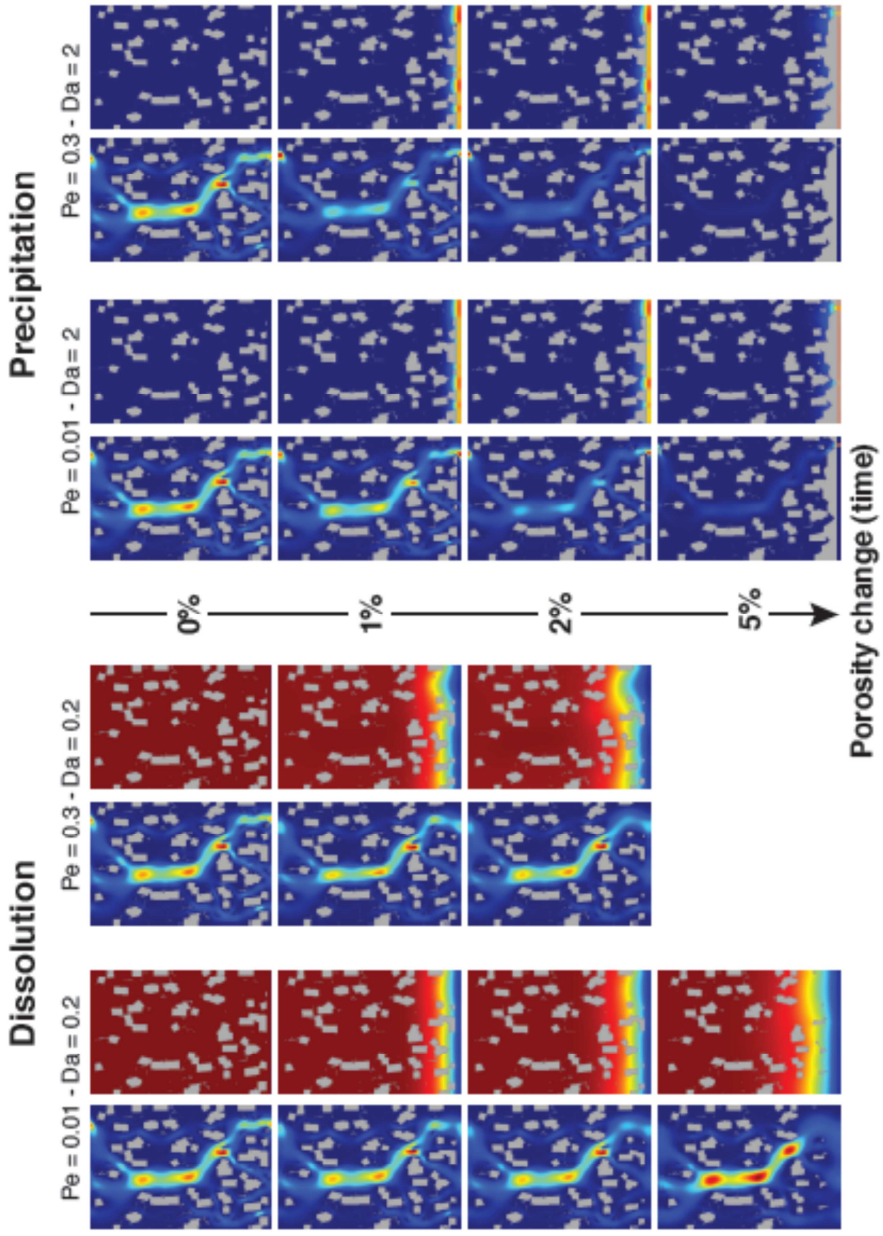

Figure 4-8: Snapshots of four different calculations with different sets of *Pe* and *Da* numbers. For each calculation, we show two columns, the first represent the flow field in the porous medium and the second the normalized (max=1) concentration of reactant dissolved in the aqueous solution. The two calculations on the left show dissolution calculations (each line represents a different change in porosity) with the same reaction rates but different ratios of advective to diffusive flux of reactant. Similarly, on the right, two precipitation calculations with the same choices of Peclet and Damkohler number as for dissolution are provided for reference.

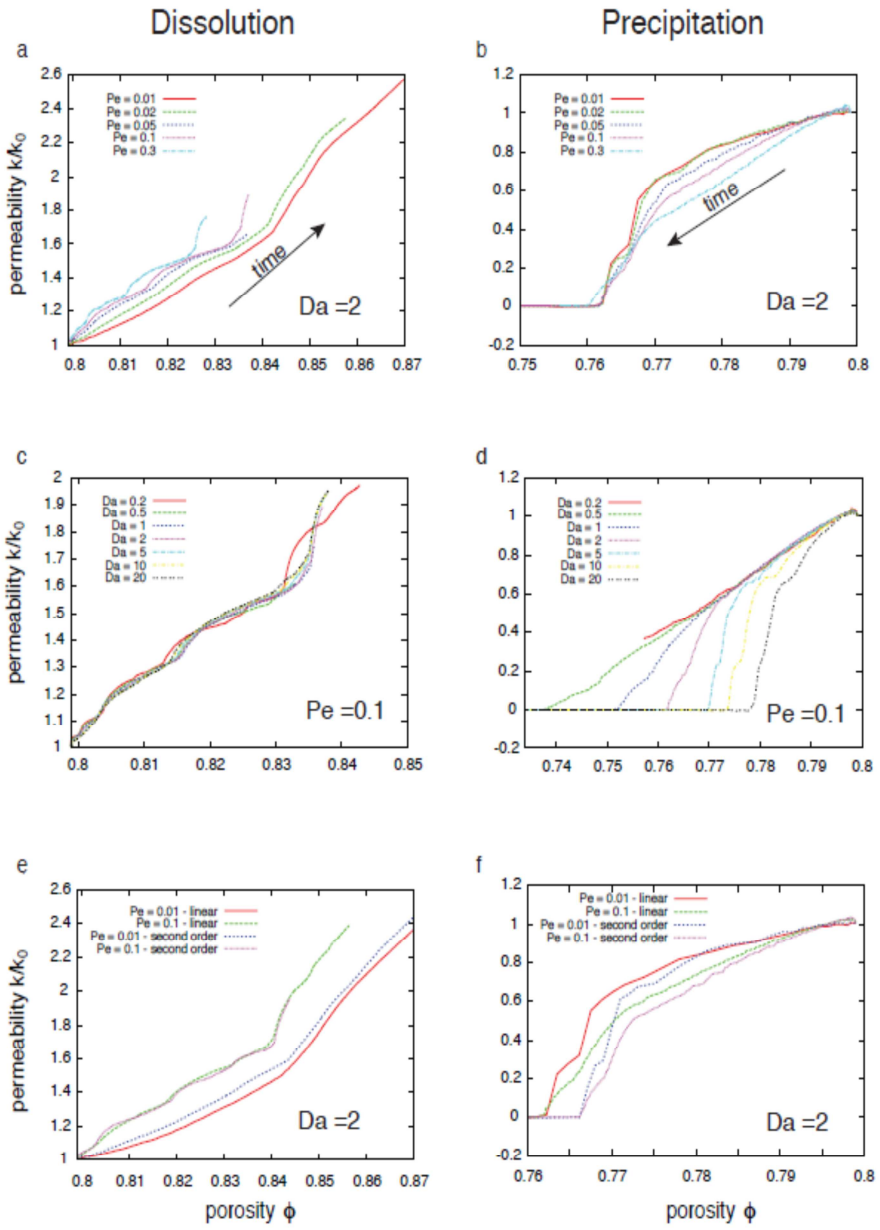

Figure 4-9: Evolution of the permeability-porosity correlation for dissolution and precipita- tion under different transport regimes and reaction rates. Panels a-c-e show dissolution calculations and the relative increase in permeability associated with the increasing porosity. We observe that the dependence on the Peclet number (panel a) is significantly more important than the dependence on the Damkohler number (panel c). The choice of linear or second order dissolution reaction (panel e) has only a minor effect on the porosity-permeability correlation. For precipitation (panels b-d-f), the effect is reversed, i.e. transport as a limited impact compared to reaction rate on the porosity-permeability relationship. We therefore expect a greater influence of the order of the reaction on the correlation as observed in panel f.

flow pathways can be clogged next to the inlet (see Figure 4.8) and the medium becomes impermeable. Panels c-d of Figure 4.9 focus on the evolution of the permeability for a fixed *Pe* = 0:1 under different reaction rates (*Da*). We see that *Da* has limited effect in this case on the evolution of the permeability during dissolution calculations, but exerts a primary control on permeability during precipitation. A faster reaction rate translates into a more substantial amount of precipitation next to the inlet blocking efficiently all the flow pathways in the system, on the other hand, permeability changes under dissolution conditions seem to be more transport-controlled.

A summary of the permeability response to a porosity change of 2% for both first order dissolution and precipitation is shown as contour plots in Figure 4.10. We observe that the permeability changes during dissolution are transport-dominated whereas the reaction rate seems to control permeability during precipitation calculations. This behavior suggest the presence of an hysteresis in the permeability-porosity relationship during cycles of dissolution-precipitation as suggested by Kang et al. (2003), we plan on addressing this issue in a future study. For all *Pe* investigated, at *Da* $\geq$1, 5% precipitation was enough to shut the medium permeability down.

We conducted another series of 70 calculations (identical) to study the difference between first and second order (*m* = 2 in equation 21) dissolution or precipitation reactions. In Figure 4.9, panels e-f, we compare how permeability evolves with porosity for *Da* = 2 and first and second order reactions with two different Peclet numbers. Our results suggest that non-linear reaction kinetics has little effect on dissolution, but the effect is more important for precipitation. This observation is consistent with the permeability evolution during dissolution being controlled primarily by transport and

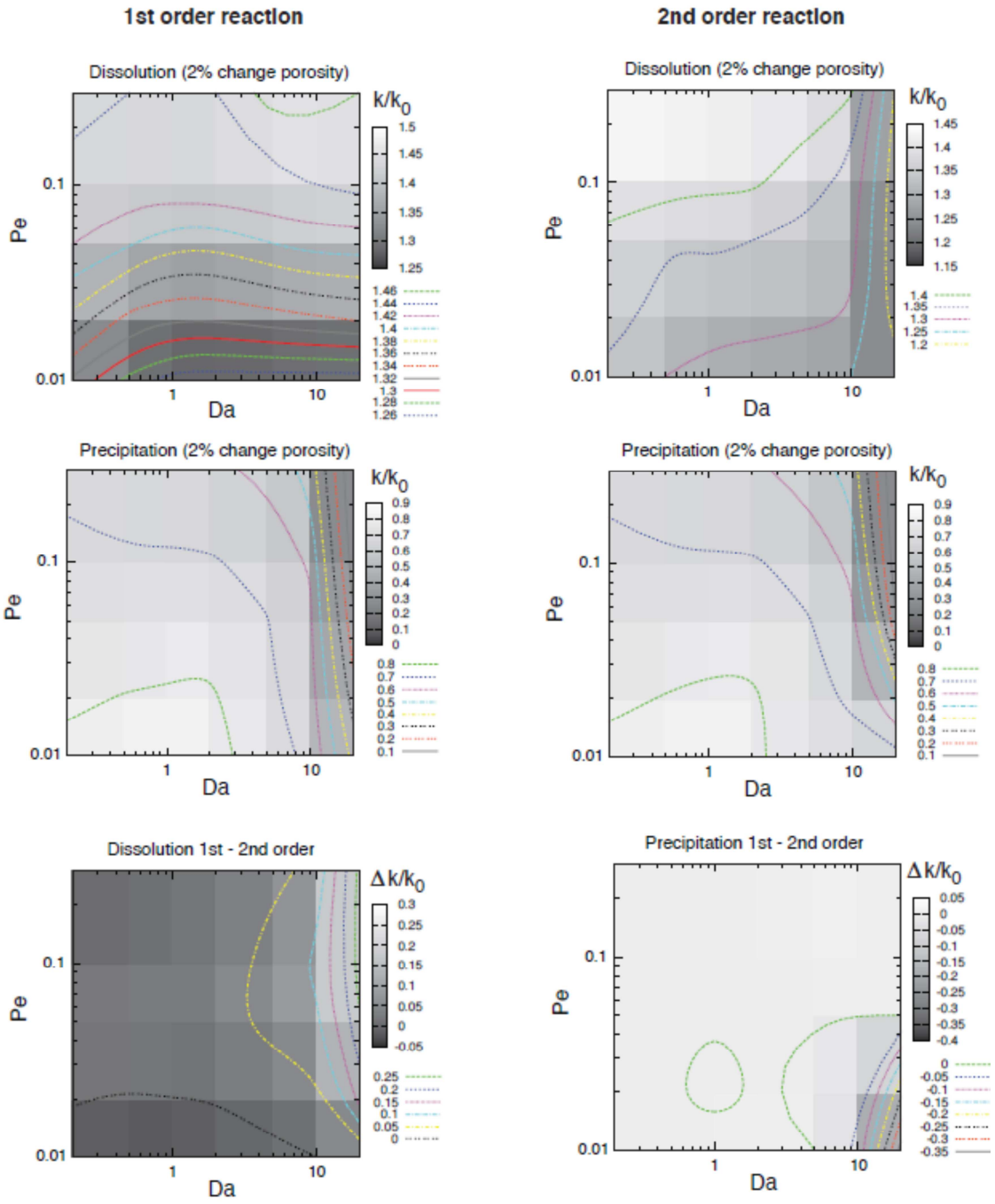

Figure 4-10: Comparison between first and second order dissolution and precipitation. The change in relative permeability plotted here corresponds to a change in porosity of 2%.

precipitation by the reaction rate. Figure 4.10 shows a summary of the 140 runs and compares the changes in permeability calculated for a change in porosity of 2% for first and second order dissolution and precipitation reactions. We observe however that the main control on the correlation between porosity and permeability during dissolution seems to depends on *Da* for non-linear kinetics (transport dominated at $Da < 5$ versus reaction-dominated for $Da \geq 5$). For precipitation, the order of the reaction does not affect qualitatively the dependence of the permeability on porosity changes for porosity changes as low as 2% in our calculations, although the effect seems more pronounced for changes greater than 2% (see Figure 9f).

An empirical rate law for the kinetics of crystal growth and dissolution has been used (Steefel and Vancappellen, 1990). In general the proposed rate law is *n*th order with respect to the saturation ratio. Steefel et al. (1990) discuss that the overall effect of the order of dissolution rate is relatively small, although the same is not applicable for changes in the formulation of the precipitation. This is consistent with our simulation results as it shows that the order of the reaction has limited impact on the permeability evolution during dissolution.

It has been shown that the relative magnitude of the reaction rate constants (*Da*) in relation to the flow rate (*Pe*) affects the evolution of the permeability-porosity relationship which is consistent with our results (Molins, 2009). As a result of dissolution, pores become wider, flow paths become less tortuous, and permeability increases non-linearly with porosity. For a given reaction rate constant, this process is more pronounced for faster flow rates. This is consistent with our results, for example in Figure 9a, a change of porosity from 0.79 to 0.84 corresponds to an increase in effective

permeability of 40% for a flow under the condition of *Pe*=0.01. If the Peclet number increases to *Pe*=0.1, for the same value of porosity change (=5%) the permeability increase by 60% instead. We emphasize that, due to the high initial porosity of the porous medium used in our calculations (in two dimensions the porosity needs to be higher to guaranty sufficient pore connectivity to allows for efficient flow pathways), the changes of permeability associated with a given porosity change during dissolution are small compared to what they can be at lower porosity and high Peclet number. In a future study, we plan on expanding the study of the permeability-porosity correlation during dissolution and precipitation reactions involving multiple dissolved species and test hysteresis behavior as the chemical conditions (oxidation state, pH) change during the course of a calculation.

4.4.2 Sorption Of Contaminant On Three Types Of Reactive Surfaces

Sorption reactions are one of the key processes that regulate the fate of dissolved chemical species in natural porous media. In natural environment, surface site heterogeneity arises from the variable chemical composition and structure of the different solid phases present in the porous medium. The spatial distribution of various types of sorption sites with different geometry and chemical affinity have a profound impact on sorption processes. Chemical heterogeneities result in spatially varying chemical characteristics such as reaction rates and site densities at the pore-scale during reactive flows. Reaction rates and site densities are generally determined from batch experiments lasting a few hours to a few days (Li et al., 2007). While these short timescales can adequately account for near equilibrium conditions for fast adsorption kinetics, it is likely that the system will approach equilibrium at a slower rate in natural field conditions.

Moreover, experimental results have indicated that the reactive parameters measured from these types of experiments are not sufficient to describe solute transport-reaction. Numerical reactive transport modeling provide a useful tool to study sorption processes in heterogeneous porous media, while experiments have limitations with regards to measuring pore-scale processes. In order to capture the effect of chemical heterogeneity, the concept of heterogeneous reaction rate (multi-rate) has been developed.

Within this approach, the reaction rates are treated as spatial random variables (Chen and Wagenet, 1995; Haggerty et al., 2000). In another approach, the heterogeneous sorption reactions have been studied in a stochastic framework using a set of stochastic differential equations (Dentz and Berkowitz, 2005; Lichtner and Tartakovsky, 2003; Zavala-Sanchez et al., 2007). The reaction kinetics of an adsorptive solute in a porous medium with a simple pore-scale geometry has been studied using a lattice Boltzmann model (Zhang et al., 2008; Zhang et al., 2002). They modeled the adsorption as linear first order kinetics. Then, based on the calculated spatio-temporal distribution of dissolved and adsorbed reactant at the pore-scale under different flow rates, volumetric-average reaction parameters were calculated to show the effect of the pore-water velocity on sorption processes.

We apply our new LB model to investigate the effect of chemical heterogeneities on the kinetics of solute adsorption. It differs from the method of Zhang et al. (2008a) in that (1) we consider the chemical heterogeneity by defining explicitely three different solid phase sorbents, (2) the sorption kinetics is non-linear, and (3) the numerical model is significantly different. We choose Arsenic as the sorbing solute because of its impact in terms of groundwater and soil contamination resulting in toxicological and

carcinogenic effect worldwide (Smedley and Kinniburgh, 2002). The aim is to capture the effect of heterogeneities on As sorption on Fe-bearing mineral phases.

Arsenic sorption is here defined by a non-linear Langmuir kinetic equation for each solid sorbent, with a maximum sorption site availability that limits the uptake of As on the solid surfaces. The availability and competition between the different solid sorbents introduces another non-linear behavior in our model. The presence of finite (maximum) site availability on the mineral surfaces is more likely to be consistent with the actual sorption process than a simple unbounded linear kinetic law.

The retention of arsenic in natural subsurface environments depends on the oxidation state of As (i.e. As(III) or As(V)), the concentration of As in solution, the pH, the availability of competing ligands and the mineralogy of the solid phases (Zhang and Selim, 2008b). Among these controlling factors, this preliminary study focuses on the effect of the initial spatial heterogeneity of sorbent sites and the competition between different types of sorbents. (Borch et al., 2010; Zhang and Selim, 2008). It has been shown that biogeochemical cycling of iron and arsenic are coupled in both oxidized and reduced environments. Solid state Fe(III) in natural porous media is typically made of an assemblage of mineral phases with variable properties. Nevertheless, in most reactive transport models, reactive Fe(III) phases are lumped together as a single species that is assumed to exhibit properties resembling those of poorly crystalline hydrous ferric oxides (HFO) such as ferrihydrite which are notoriously short-lived (Hyacinthe et al., 2006). These HFO rapidly transform into other Fe-bearing phases, such as goethite (α-$Fe^{III}OOH$) and magnetite ($Fe^{II}OFe^{III}_2O_3$) (Tronc et al., 1992; Hansel et al., 2003). In previous studies, goethite was shown to be formed directly through the dehydration of $Fe(OH)_3$ while

magnetite formed through the translocation of an electron from Fe(II) into $Fe(OH)_3$. The transformations of Fe(III) minerals may deeply influence the uptake and release of arsenic, as shown for example by Petersen et al. (2006); Tufano et al. (2008). We assume that three phases of iron minerals including (1) highly reactive ferric hydrous oxides $Fe(OH)_3$, (2) goethite and (3) magnetite are present initially, but the effect of phase transformation is not considered here since it requires a multi-species reactive transport model and coupling reaction-transport processes to Fe(II) as the driver of iron phase transformation. The LB model presented here can easily be extended to multiple species and this will be the focus of future work.

In general, the sorption reaction of As on any of the iron solid phases can be written as

$$As_{(aq)} + Fe - OH_{[s]} \leftrightarrows Fe - As_{[s]} \tag{4.44}$$

where $As_{(aq)}$is the arsenic concentration in the aqueous phase, $Fe - OH_{[s]}$ is the concentration of the solid phase iron (i.e. adsorption sites), $Fe - As_{[s]}$ is the concentration of arsenic in the solid phase, and, finally, k_{ads} and k_{des} are the adsorption and desorption reaction rate constants. Non-equilibrium reversible sorption models have been applied widely to describe the kinetics of arsenic adsorption-desorption (Darland and Inskeep, 1997; Elkhatib et al., 1984). We use a Langmuir kinetic rate law for each three types of sorbent, where an adsorbed As concentration maximum is assumed for each sorbent on the basis of the local sorption site availability. The sorption reaction becomes (see Equation 4.34)

$$\frac{\partial As^i_{[s]}}{\partial x} = \frac{k_i}{\rho_s}\left(As^{i,max}_{[s]} - As^i_{[s]}\right)As_{(aq)} - k_{dj}As^i_{[s]} \tag{4.45}$$

with i is an index refering to the Fe-bearing solid phase (Ferrihydrite, Goethite or Magnetite), $As^{i}_{[s]}$ is the concentration of arsenic sorbed on phase i (in units of mol/gr), $As_{(aq)}$ is the concentration of arsenic in solution (in units of mol/L) and ρ_s is the density of the solid phase. Using Equation 4.35, the local maximum sorption capacity of site i is computed with

$$As^{i,max}_{[s]}(x,t) = FeOH^{i}_{[s]}(x,t=0) S_A S_D M_{w,FeOH^i} \tag{4.46}$$

where $FeOH^{i}_{[s]}$ is the local initial concentration of Fe-bearing phase i (in mol/gr). The values used in the calculations are listed in Table 5.2. These values are obtained from Dixit and Hering (2003) where the combined effect of As(V) and As(III) sorption on HFO, goethite and magnetite in various solution compositions was studied using a diffusive double layer surface complexation model. The surface site densities of the solid phases were calculated from sorption isotherms while surface area was measured by N2 BET. We assumed the site density for magnetite to be intermediate between the site density for HFO and goethite. It is known that both arsenate and arsenite form inner-sphere and/or outer-sphere complexes with iron minerals and are adsorbed through ligand exchange (Dixit and Hering, 2003; Zhang and Selim, 2008b). As stated before, in the current study we will focus solely on physical and chemical heterogeneity effects on arsenic sorption and the detailed description of the mechanism of sorption processes through SCM will be postponed to a future study.

In summary, there are three different solid phases in our model including ferrihydrite (F), goethite (G) and magnetite (M) where As sorption on each of these phases will be defined by distinct adsorption rates and a maximum local number of available sorption sites. Because of the heterogeneous initial concentration of Fe-bearing

phases at the pore-scale, $As_{[s]}^{i,max}$ is heterogeneous as well. The desorption rate is assumed to be identical for all phases in order to reduce the parameter space in our calculations. We define a set of four Damkohler numbers to describe the kinetics for each calculation, the first three consists of the adsorption reaction for each $As_{[s]}^{i}$ (with i =F, G or M) and the last corresponds to the desorption reaction (identical for all phases).

The spatial distribution of each phases (F, G and M) is set randomly but the geometry of the porous medium stays the same for all 32 calculations. We define four sets of calculations with different kinetic rates (or set of Damkohler numbers). In the first set of calculations, the Damkohler number for the adsorption on ferrihydrite is set to 1 while the three other *Da* are set to 0.1.

In the second set of calculations, all *Da* are set to 0.1 except for the adsorption on goethite, while for the third set of calculations it is Da associated with the adsorption on magnetite that is set to 1. In the last set of calculations, all adsorption reactions are set with *Da*=1, while desorption remains fixed with *Da*=0.1. For each of these four set of calculations, eight realizations are run with different random initial spatial distribution of

Table 4-2: Constants used in the arsenic sorption calculations (from Dixit and Hering, 2003).

	Surface area S_A	Site density S_D	Molecular weight $M_{w,FeOH^i}$
Ferrihydrite	600	3.5×10^{-6}	168.6
Goethite	54	3.84×10^{-6}	88.85
Magnetite	60	3.6×10^{-6}	231.54

sorption site for each Fe-bearing phase to study the separate effect of the reaction rate and variable heterogeneous distribution of the different sorption sites on the uptake of As from the solution. Once a steady flow is established in the porous medium (non-reactive, no arsenic in solution initially), the concentration of As in solution at the inlet is set to 1 (normalized).

Arsenic sorption isotherms for the eight realization with Da_F = 1 and Da_G =Da_M=Da_{des}=0.1 are plotted in Figure 4.11. For each mineral phase, the average concentration of As in solution (normalized with respect to the inlet boundary concentration) and As sorbed on each phase (normalized by the integrated initial concentration of all Fe-bearing phases) are computed as function of time. The results we obtained are compatible with the general behavior expected for isotherms computed with a Langmuir sorption model, i.e. the adsorbed quantity of As increases with the dissolved amount of As and reached a plateau (maximum adsorption that is controlled by the values $As_{[s]}^{i,max}$). The total amount of As sorbed on all phases is also computed and is very close to the concentration of As sorbed on HFO (ferrihydrite). This demonstrates that HFO, which has the largest sorption site density (surface area SA about an order of magnitude greater than the two other phases) dominates the fluid-rock As exchange. In this particular test, the initial differences in spatial distribution and concentration of Fe-bearing phases does not play a primary role on the As uptake, although we would expect that a less isotropic geometrical structure for the porous medium such as flow focused in fractures would yield a more important control of the distribution of spatial heterogeneties than we observe here.

Figure 4.12 shows four snapshots taken at different times and showing the spatial distribution of As in solution as well as the concentration of As sorbed on the solid surface for ferrihydrite, goethite and magnetite. As time evolves, the dissolved arsenic is removed from the aqueous fluid and adsorbed on the different mineral phases. The spatial distribution of adsorbed arsenic depends on the initial distribution of sorbent and their local maximum sorption capacity. Figure 4.13 shows pie charts to illustrate the effect of the set of Damkohler numbers on the proportion of As uptake for each sorbent at the end of the calculations ($\tau = Dt/\delta^2$ = 1:32, where D is the diffusion coefficient for As in the solution). In all calculations ferrihydrite is the most potent sorbent of all three Fe-bearing minerals, this is because of its large effective surface area relative to the other two phases. The site density and maximum sorption capacity is therefore about an order of magnitude greater for ferrihydrite than for goethite or magnetite. We can study the competition between the different phases in terms of As uptake when Da=1 for all adsorption reactions, we observe that ferrihydrite accounts for 84% of the adsorbed As while magnetite and goethite retain respectively 12% and 4%. When the adsorption rate constants are set so that $Da_F < Da_G$ or Da_M, the As uptake remains dominated by ferrihydrite, but the proportion decreases from 84 to 64%. The proportion of adsorbed As reaches however 95 % when the reaction rate for ferrihydrite is 10 times greater than for goethite and magnetite. We observe that the competition among the different phases for the arsenic in solution plays a significant role on the proportion of arsenic sorbed on each type of reactive surface. It is important to note that the total amount of As uptake (at the end of the runs) depends obviously on the integrated capacity of sorbed surface site, but also on the set of Damkohler numbers (reaction rates) for the sorption reactions. In figure

14, we plot the spread in As uptake found for the eight realizations with different initial sorption site distribution (vertical error bars) and the ensemble average value (red dot) for the four different reaction rates sets. We note that the largest amount of As uptake is observed when $Da_F = 1$ and $Da_G=Da_M=Da_{des} = 0{:}1$, and not when all the adsorption rates are maximal (equal to 1), which means that the competition for sorption among different phases may lead to suboptimal uptake when the phases with lower sorption capacity react at a rate comparable to the phase with the highest sorption capacity. Our calculations show that chemically and physically heterogeneous environments affect the retention of As on the solid phase. The competition between the different sorption reactions and the spatial heterogeneities require a pore-scale treatment of the reactive process. We observed that these heterogeneities and competing reaction rates can yield significant differences in the mass exchange between the aqueous and solid phases during the transport of As in porous media. Our results point to the specific surface area as a major control on the uptake of arsenic, which is limited by the availability of surface sorption sites. A decrease in specific surface area associated with phase transformations from HFO to either goethite or magnetite is expected to limit the As sorption capacity of the porous medium and hence increase the mobility of As. In the future, we plan on considering the effect of As speciation and solution chemical composition (such as pH for example) on the mobility of arsenic in groundwater systems. Previous studies have shown that the transformation of HFO to goethite or magnetite should not decrease the affinity of the solid phase for As(III) and As(V), however, a decrease in specific reactive surface area can potentially increase the mobility of As (Dixit and Hering,2003). A pore-

scale study of As sorption considering solid phase transformation should shed some light on the controls of As sorption in natural systems.

4.5 Conclusion

We developed a new pore-scale reactive transport model based on the lattice Boltzmann method. The model is based on a phase-field method and therefore surface reactions are treated as sources or sinks in the computational domain which offers the great advantage that the reactive part of the algorithm is independent of the topology and orientation of the solid-fluid interface. To improve the accuracy of the method, we developed an iterative solver for the advection-diffusion of reactant and reactions that ensure a great accuracy even for high reaction rates.

In this preliminary study, we used the model to study the influence of the reactant transport regime (parameterized in terms of a Peclet number) and the reaction rate (parameterized using the Damkohler number) on the permeability evolution of a porous medium during dissolution and precipitation for linear and non-linear reactions. We found that for dissolution, the transport regime exerts the main control on the evolution of the permeability, whereas the reaction rate controls permeability during precipitation. Because of that, precipitation seems more sensitive to the order of the reaction than dissolution.

The model has also been modified to study sorption reactions and specifically the uptake of arsenic by three competing Fe-bearing phases (ferrihydrite, goethite and magnetite) using a (non-linear) Langmuir reaction equation. We studied the effect of the spatial distribution of sorption sites for each solid phase and the different reaction rates on the uptake of As by each phase. Our model clearly showed that an increase in the

adsorption rate does not necessarily translates into an increased uptake of As, because of the competition between the different sorbent. Ferrihydrite is controlling the largest portion of the removal of As from the aqueous solution because of its greater sorption capacity, but increasing the adsorption rate for the two other phases may lead to a reduction of As removal because goethite and magnetite compete with ferrihydrite for the dissolved As.

In future studies, we plan on expanding our model (1) to introduce multiple solute species, (2) to test precipitation-dissolution hysteresis problems (for single and multiple species) and (3) to introduce various surface complexation models for sorption processes. These extensions will allow us, for example, to expand on the As sorption model by including the effect of the aqueous solution chemistry on the speciation of As and to include phase transformation from ferrihydrite to either magnetite or goethite as a function of time.

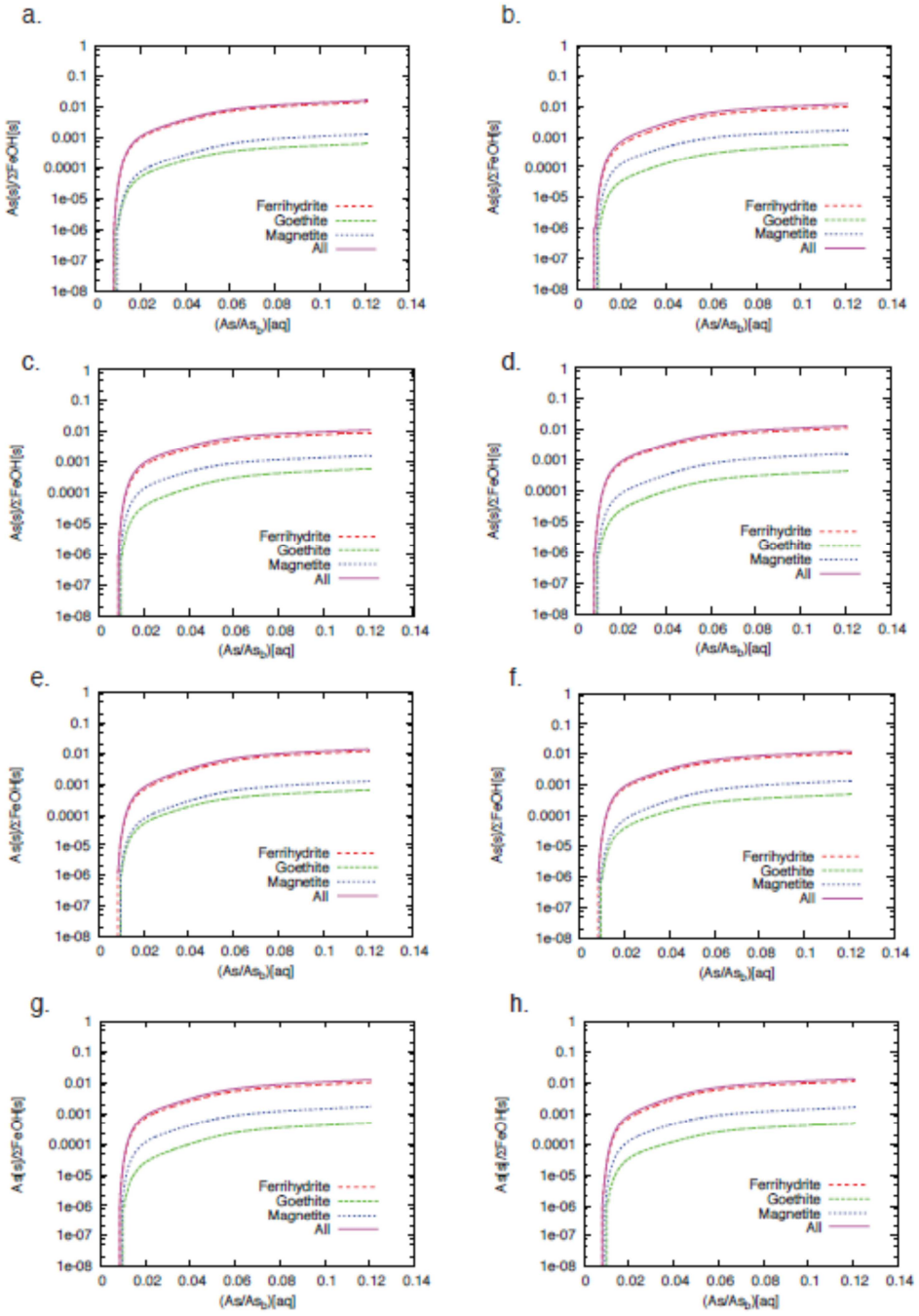

Figure 4-11: Sorption isotherms for As with *Pe* fixed to 0.1, Da_F =1, $DaG = Da_M = Da_{des}$=0.1. Eight realizations with different initial spatial distribution of sorbent concentration on the different surfaces of the same porous medium are shown in the different panels. Most of the uptake of As is done through the adsorption on ferrihydrite surfaces (greater effective surface area).

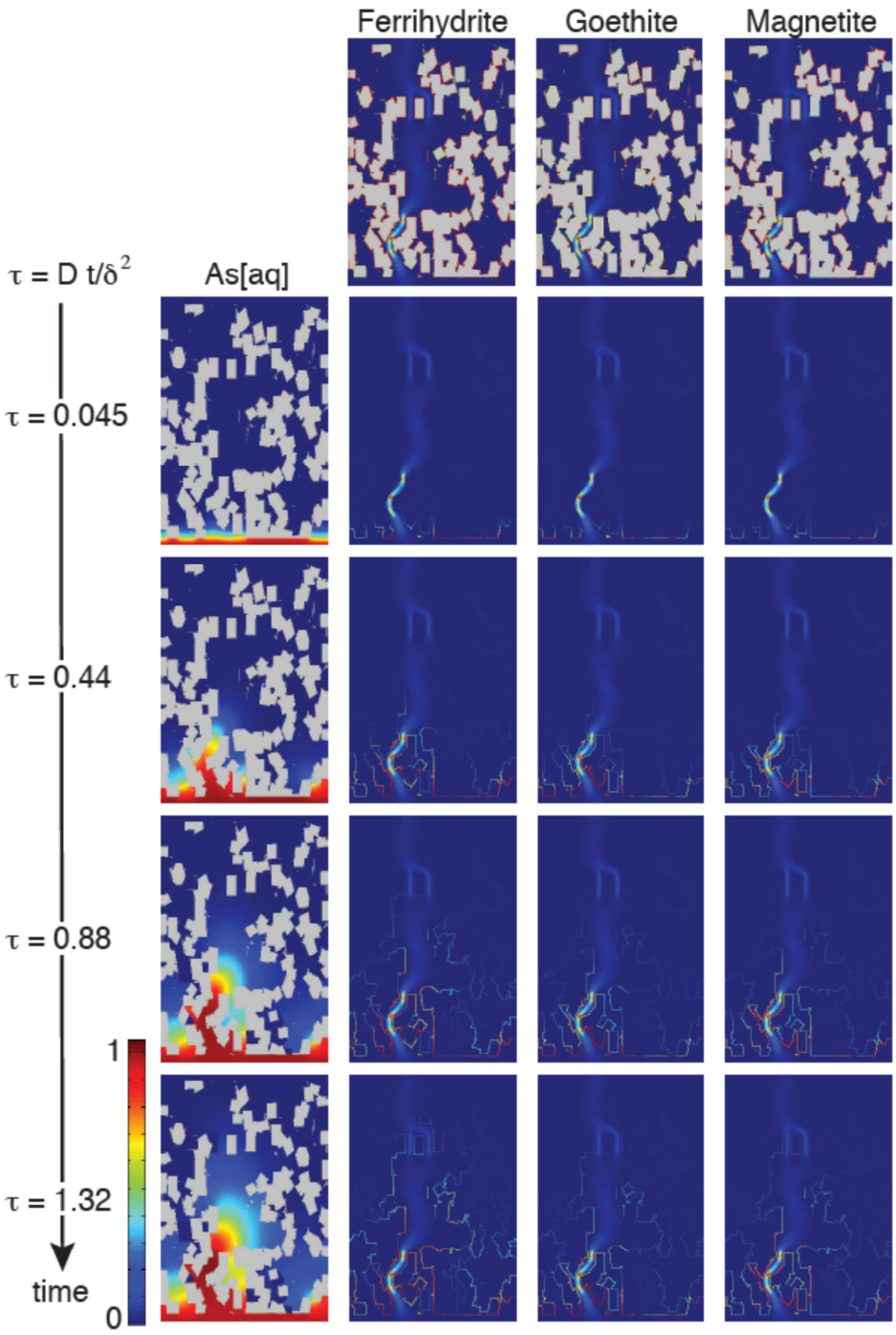

Figure 4-12: Snapshots taken at four different times for the calculation with *Pe* fixed to 0.1, $Da_F = 1$, $Da_G = Da_M = Da_{des} = 0.1$. The first column shows the As in solution, while the other columns show a superposition of the flow field and the grain surface concentration in $As^{i}_{[s]}$.

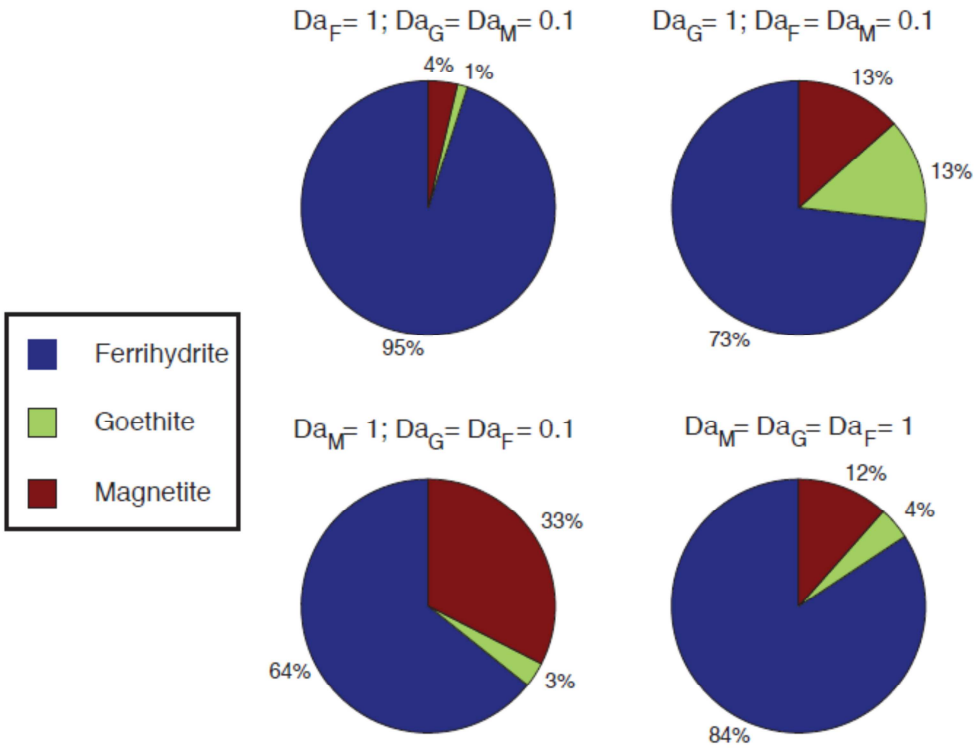

Figure 4-13: Proportion of As uptake by the three different reactive mineral phases for thedifferent sets of Damkohler numbers. The ensemble average for the eight realizations are plotted here. In all cases, ferrihydrite dominates the exchange of As because of its greaterspecific surface area available for sorption.

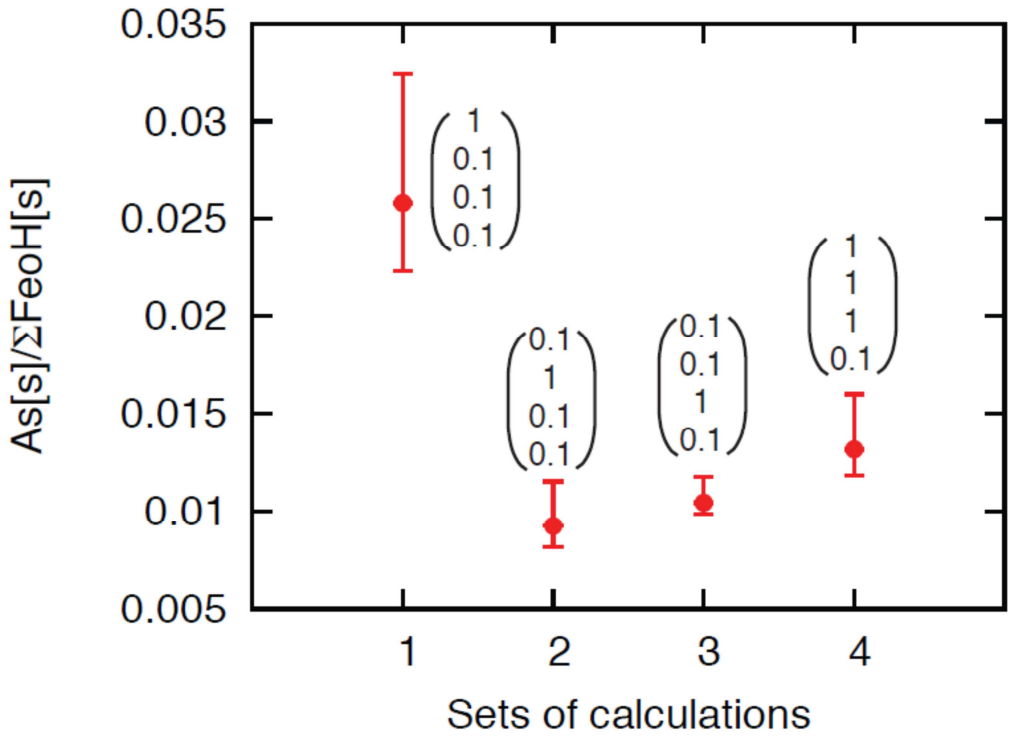

Figure 4-14: Range and ensemble average amount of As uptake for the four different scenarios tested in this study. The four numbers listed in parenthesis next to the data correspond to Da_F , Da_G;Da_M, and Da_{des} respectively. The range and ensemble average of the uptake of As when the rate of adsorption of As is equal to 1 for ferrihydrite and 0.1 for the other phases is greater than for the case where the adsorption is the most rapid (*Da* for all phases equal to 1), which confirms that the competition between phases with different sorption capacity may be suboptimal for As removal.

CHAPTER 5: CONCLUSION AND SUGGESTIONS

In this study first we developed a quantitative, though approximate, criteria on the range of validity of LEA in aquatic sediments with irreversible heterogeneous sorption reactions. Applying LEA simplifies the thermodynamics, mathematics and numerical analysis. Unfortunately, LEA is applied intuitively and many hypothesizes are made. Using the newly developed mathematical approach in Chapter 2 leads to parallel derivations of LEA and non-equilibrium (SKIT) diagenesis formulations. The form of the SKIT equation indicates the equivalence of the error associated with the use of an LEA and the error of neglecting the kinetically influenced terms. For sufficiently small kinetic term, LEA is an applicable assumption. The two formulations for a given transport problem are easily comparable because they consist of the same variables. The simulation results demonstrate that dimensionless prefix dominator (P_D) and reaction transport parameters such as *Pe*, *Da* and γ conveniently determine the criteria for applicability of LEA diagenesis models. Knowledge of rate laws and rate constants as well as information on the physical transport parameters and boundary conditions are required to evaluate the dimensionless parameters for a given problem. It is concluded that kinetic data are necessary in order to make an appropriate choice of model-LEA or kinetic based- for simulating transport under a given set of conditions.

This approach can be extended in future to:

1. include multi-species reactive transport systems to study various solid phase sorbants.

2. define sorption kinetics through various sorption isotherms such as Langmuir or diffusion-limited kinetics.
3. investigate LEA application in multi-dimensional problems.

In Chapter3, we presented a 1-D early diagenetic module developed in MATLAB. The module, MATSEDLAB, provides templates for representing the reaction network, boundary conditions and transport regime, which the user can then modify to fit the particular early diagenetic model configuration of interest. The choice of MATLAB over other mathematical software packages reflects its prevalence in the biogeosciences community. As an interactive programming environment, MATLAB provides a range of tools for solving systems of coupled differential equations. In particular, the module presented here relies on the computationally efficient MATLAB *pdepe* solver, which allows complex early diagenetic scenarios to be simulated and analyzed on a personal computer. The capabilities of the model was shown through various theoretical and practical applications.

We applied MATSEDLAB to describe the non-steady state dynamics of arsenic and major redox elements in water-saturated sediments of Lake Tantaré in Canada that has experienced variations in atmospheric deposition of As and SO_4^{2-} over the last century. The simulation results showed that about 10% of As currently deposited at the SWI is buried in the form of $FeS_{(s)}$-bound As whereas 75% is transported to the overlying water, suggesting that the remaining 15% of is trapped in the redox loop associated with the $Fe(OH)_{3(s)}$ recycling. Modeling As sorption using kinetic and mixed kinetic-equilibrium approaches revealed that fully kinetic approach predicts the 100% of the sorbed As on the solid phase in the coprecipitated form. Consecutive model predicted

higher concentration of adsorbed As with respect to the concurrent one at each depth. The results proved that truly adsorbed As is a minor fraction of the solid phase As pool in the sediment.

The results of simulations of seasonal organic carbon deposition illustrated that the time scale required for the solid-bound sediment composition to relax from the imposed initial conditions is on the order of 20 years. It was demonestrated that at SWI the concentrations of iron (oxy)hydroxides and monosulfides show seasonal oscillations as a result of the periodic supply of organic carbon. The pore water profiles resolved the seasonal variations in the externally forced input of degradable organic carbon, while solid-state profiles were sensitive to changes at longer time scales.

Iron phase transformation modeling results showed that it takes several decades for the secondary iron oxides (goethite and magnetite) to reach their final concentrations. That is, the stabilization of reactive Fe(III) through transformation into stable iron oxides is a relatively long-term process. This may help explain why the simple representation of a single reactive Fe(III) sediment pool may in many cases be sufficient to capture the rapid redox cycling of iron close to the SWI.

MATSEDLAB successfully was applied to capture the features of two real-world non-steady state scenarios. In the first application MATSEDLAB provided a tool to reproduce the measured profiles of early diagenesis following a flood event in Rhône River. Also it was used to: 1) understand and quantify the impact of sediment deposition on biogeochemical processes and 2) simulate the relaxation of the sediments if we suppose that the processes and boundary conditions went back to “preflood” conditions after the event.

In second application sediment diagenesis in an AMD contaminated reservoir in the Odiel Basin, Huelva (SW Spain) was simulated. Due to the monomictic behavior of the reservoir non-steady-state boundary conditions were imposed as a function of time for O_2, as an error function, and for the $Fe(OH)_3$ (s) flux, because of its dependence on the O_2 concentration.

For future applications, there are so many features that can be added to MATSEDLAB such as:

1. adding acid-base equilibration reactions
2. incorporating carbonate system within the reaction network
3. pH calculation
4. providing GUI for more user-friendly experience
5. adding an automatic optimization routine for estimating the transport-reaction parameters for the calibration purposes
6. multi-dimensional simulation
7. parallelization of MATSEDLAB for the efficient CPU usage
8. surface complexation modeling for sorption problems

In Chapter 4, we presented a new pore-scale model for the advection and diffusion of reactants in porous media with complex topologies. The model is based on the lattice Boltzmann method and couples a fluid flow solver to an optimal advection-diffusion transport model where transport and reactions between chemical species are solved iteratively. Internal solid-fluid boundaries (grain boundaries) are explicitly part of the numerical domain which allows the algorithm to solve for surface reactions independently from the surface shape and orientation. We presented two reactive

transport applications with the model. In the first application we studied the permeability change of a porous medium associated with a given porosity change during dissolution and precipitation using linear and second order reaction kinetics. We showed that, for a given porous medium, the correlation between porosity and permeability changes depends on the transport regime (the ratio of advective to diffusive transport) and the reaction rate. For instance, the change in permeability during dissolution is more sensitive to the transport conditions than the reaction rate, whereas we observe the opposite behavior for precipitation. The second application of our model was for arsenic sorption on Fe-bearing minerals. We studied the effect of spatial heterogeneities and the efficacy of different Fe-bearing sorbents phases competing for the uptake of arsenic from the aqueous solution. We showed that the sorption capacity is controlled by the effective surface area of the mineral phase and impacts significantly the competition for the partitioning of dissolved As between the different sorbent and the amount of As removed from the aqueous solution.

In future studies, we plan on expanding our model to:

1. introduce multi-component reactive transport systems
2. incorporate complex reaction network such as biogeochemical redox reaction, secondary reaction and acid-base equilibration reactions
3. test precipitation-dissolution hysteresis problems (for single and multiple species)
4. introduce various surface complexation models for sorption processes
5. simulate multi-dimensional pore-scale effects

6. couple the fluid flow and solute transport with geochemical softwares such as PHREEQC

These extensions will allow us, for example, to expand on the As sorption model by including the effect of the aqueous solution chemistry on the speciation of As and to include phase transformation from ferrihydrite to either magnetite or goethite as a function of time.

APPENDIX A: GETTING STARTED WITH MATSEDLAB

Execution of MATSEDLAB requires a Windows PC with an active installation of MATLAB® (Version 7.6 release R2008a or later) and MS Excel (Version 2007 of later). It is recommended to allow at least 1GB of space on the hard drive for the model output and 4GB of contiguous read-only memory for the initialization routine. MATSEDLAB was developed in and tested up to release R2011b. MATSEDLAB is executed through the MATLAB home screen. First make the MADSEDLAB folder visible in your workspace and save all the .pdf files starting their names by *shafei_babak_201212_phd_matsedlab* as MATLAB .m files. For example in order to run the first application, create a new .m file of *MATSEDLAB_app_00.m* using corresponding *shafei_babak_201212_phd_matsedlab_app_00.pdf* and type its name in workspace to launch the first application.

A.1. Preparing A Field Dataset

If the user has field data, the measured concentrations data can be saved in a MS EXCEL file named '**FIELD_DATA.xls**' placed in the MATSEDLAB directory (as an example we provided all the measured concentrations of the species in separate pdf files). The current format and layout must be respected for the file to be read accurately by MATSEDLAB, which include separate worksheets for each species with the depths and associated measured concentrations in the first and second columns.

A.2. Locating The MATSEDLAB Matrices

MATSELAB relies on the following matrices to solve the early diagenetic problem. The user is invited to locate them in *MATSEDLAB_00.m* before using the code. These matrices have to be edited to configure MATSEDLAB, especially when adding new reactions and species.

Number Of Species

```
c = ones(1,8);
```

Transport

```
f = [(D_bio+D_O2)*DuDx(1)-w*u(1);...
   D_bio*DuDx(2)-w*u(2);...
   (D_bio+D_SO4)*DuDx(3)-w*u(3);...
   (D_bio+D_Fe)*DuDx(4)-w*u(4);...
   (D_bio+D_H2S)*DuDx(5)-w*u(5);...
   D_bio*DuDx(6)-w*u(6);...
   (D_bio+D_AsO4)*DuDx(7)-w*u(7);...
   D_bio*DuDx(8)-w*u(8)];
```

Reaction

```
s = [(BC0_O2-u(1))*alfax-F*R1-.25*R5-2*R4;...
   -4*R2+R5/F-8*R6;...
   (BC0_SO4-u(3))*alfax+F*(R6-.5*R3)+R4;...
   (BC0_Fe-u(4))*alfax+F*(4*R2+8*R6+R7-R_7)-R5;...
   (BC0_H2S-u(5))*alfax+F*(.5*R3-R6+R7-R_7-R10);...
   -R7+R_7;...
   (-4*fAsFe*R2)+(-8*fAsFe*R6)+(R8+R9)/F;...
   (BC0_AsO4-u(8))*alfax+F*fAsFe*(4*R2+8*R6)-R8-R9];
```

Upper Boundary Conditions

```
pl = [ul(1)-BC0_O2;...
     BC0_FeOH3/F;...
     ul(3)-BC0_SO4;...
     ul(4)-BC0_Fe;...
     ul(5)-BC0_H2S;...
     BC0_FeS/F;...
     BC0_AsFeOx/F;...
     ul(8)-BC0_AsO4];
```

```
ql = [0;1;0;0;0;1;1;0];
```

Lower Boundary Conditions

```
pr = [w*ur(1);...
      w*ur(2);...
      w*ur(3);...
      w*ur(4);...
      w*ur(5);...
      w*ur(6);...
      w*ur(7);...
      w*ur(8)];

qr = ones(1,8);
```

A.3. Examples And Applications

MATSEDLAB is in effect a series of examples that the user can choose and adapt to his/her particular problem. The core m-files (*MATSEDLAB*_00, 01, 02 and 03.m) are corresponds to the biogeochemical simulation module and can be used as is. Three other examples are also provided to show how MATSEDLAB can be modified and adapted to various scenarios.

A.4. MATSEDLAB_00.m

MATSEDLAB_00.m corresponds to the early diagenetic system described in detail by the authors for a transient modeling study of arsenic (As) cycling in the sediments of an oligotrophic lake in eastern Canada (Couture et al., 2010). This baseline simulation is based on an extensive dataset collected from the perennially oxygenated basin of an oligotrophic lake to describe the coupled cycling of As, C, O, Fe and S. Note that the parameters and boundary values are defined directly in the script that is provided, not through an input file.

A.5. Boundary Conditions : Steady State / Non-Steady State

There are switches in the code (e.g. 'commented' lines) that can be activated (e.g., 'uncommented') in order to use different formulations. For example, the time-dependant BC for the deposition of As and SO_4 depositions are stored in variables **BC0_AsFeOx** and **BC0_SO4**. In MATSEDLAB these variables are provided for non-steady state as well as for steady state formulations. The user must choose the appropriate formulation and comment/uncomment the desired lines. For example, steady state boundary conditions for sulfate and arsenic are defined as follows:

```
% BC0_SO4 = 0.022 + 0.06*exp(-0.5*((t-182)/10)^2);
% BC0_AsFeOx = 2.14e-3 + 1.9e-3*exp(-0.5*((t-152)/6)^2);
BC0_SO4=.033;
BC0_AsFeOx=BC0_FeOH3*0.32e-3;
```

If the user desires to use non steady-state boundary conditions, the lines can be switched as follows:

```
BC0_SO4 = 0.022 + 0.06*exp(-0.5*((t-182)/10)^2);
BC0_AsFeOx=2.14e-3 + 1.9e-3*exp(-0.5*((t-152)/6)^2);
% BC0_SO4=.033;
% BC0_AsFeOx=BC0_FeOH3*0.32e-3;
```

In this example, we assumed that the variation over time (t) in sulfate (SO_4^{2}) concentrations at the sediment-water interface of eastern North-American lakes was best described by the following bell function

A.6. Porosity : Fixed / Depth-Dependent

The default code is run for a constant porosity of 0.9, expressed as a conversion factor F equal to $\rho(1-\varphi)/\varphi$ (where ρ is the density of dry sediment (g cm^{-3}) and φ the

porosity) which allows MATSEDLAB to consider aqueous and solid-phase concentrations interchangeably. By default, it is implemented as follows:

```
F=.06;
```

Switching to depth-dependant porosity is not trivial since it changes also the tortuosity and hence affect the diffusion of the species considered (Boudreau, 1999). In MATSEDLAB, the following lines must be uncommented:

```
%uncomment if porosity is depth-dependant
phi=.9*exp(-0.2*x);
Dphi=-.18*exp(-.2*x);
```

In addition, modified versions of the matrices **c**, **f**, **s**, **pl** and **pr** must be activated as well. For instance:

```
c=ones(1,8);
%depth dependant porosity
```

becomes:

```
%depth dependant porosity
c = [ phi;...
     1-phi;...
     phi;...
     phi;...
     phi;...
     1-phi;...
     phi;...
     1-phi];
```

Note that modified versions of the matrices **c**, **f**, **s**,**pl** and **pr** are already present in MATSEDLAB.

A.7. Adding New Chemical Species

When adding a new species, the size of the all of the matrices must be updated by the number of new species. Depending on whether the new species is solutes or a solid, the matrices must be modified accordingly.

The *MATSEDLAB_00.m* script for the baseline simulation does not include nitrogen species and reactions. Let us suppose the user desires to add denitrification coupled to organic carbon oxidation to the existing reaction network. The user first supplies in *Block One* (see article) the additional initial and boundary conditions for nitrate, the kinetic reaction parameters for denitrification, and the diffusion coefficient of nitrate. In the current formulation of the reaction kinetics of primary redox reactions, two new reaction parameters must be introduced: the half-saturation constant for nitrate uptake during denitrification (K_m NO3) and the inhibition constant of dissimilatory iron reduction and sulfate reduction by nitrate NO_3^- (K_{in} NO_3). The following lines can thus be activated:

```
%adding nitrate to the reaction network
KNO3=10;%NO3 half saturation
kinNO3=10;
fNO3=u(10)/(KNO3+u(10))*kinO2/(kinO2+u(1));
R11=Rc*fNO3;  %OM oxiation by NO3 (denitrification)
finNO3=kinNO3/(kinNO3+u(10)); % inhibition factor of NO3
R12=knh4ox*u(1)*u(11); %Nitrification
```

The introduction of the new species and reaction also requires the expansion of matrices *c*, *f*, *s*, *pl* and *pr* in *Blocks Two, Three* and *Four*, by including NO_3^- as the 9th species. Because nitrate is a dissolved species, transport terms and boundary conditions for solutes are used when updating the matrices. Note that besides introducing a new rate equation for denitrification, the existing rate equations for dissimilatory iron and sulfate reduction (R2 and R3 in *MATSEDLAB_00.m*) must be modified to account for the inhibition of these respiratory pathways by nitrate.

A.8. MATSEDLAB_01.m

MATSEDLAB transfers simulated concentration values at each time and depth into a Microsoft Excel file and saves it as ‘simulation_results.xls’ in the current directory. Note that this file is not used for plotting purposes in MATSEDLAB.

A.9. MATSEDLAB_02.m

Depth-concentration profiles of the pore water and solid-bound species can be plotted versus measured filed data for any time step of the simulation. First, the measured concentrations and depths in excel file (‘FIELD_DATA.xls’) in the current directory is read by *MATSEDLAB_02.pdf*. This file includes 8 worksheets which corresponds to the 8 species included with the examples provided.

A.10. MATSEDLAB _03.m

Then script *MATSEDLAB_03.pdf*. produces depth-concentration plots on which measured concentrations are displayed together with the computed profiles in separated figures. Also the associated file with each figure is created in the current directory with the name of each species. In case field data are not available, only simulated profiles will be plotted.

A.11. MATSEDLAB _app_01.m

The *MATSEDLAB_app_01.m* script corresponds to the reactive transport model used by Couture et al. (2010) to simulate the early diagenesis of arsenic (As) in a lake in eastern Canada. Here, the sensitivity of the model-computed benthic efflux of dissolved As, J_{As}, to each of the reaction and transport parameter is quantitatively assessed. The sensitivity analysis is performed under steady state conditions, by keeping

the particulate As deposition rate and bottom water sulfate concentration constant (see lines 108-116 in *MATSEDLAB_app_01.m*). The sensitivity, *S(x,y)*, of model outcome *x* (= J_{As}) to changes in the parameter *y* is defined as Equation (3.16). To obtain the values in Table 6 (see article) associated with each parameter, the script is first run for the initial value of the parameter. The variable '**fT**' which stores the values of the total flux (bioirrigation+diffusion) of As through SWI, must be retrieved by using the **global** command (see section 5) after the simulation. The code must be run again for the new value of the studied parameter and saving the value of **fT**. Two **fT** values are replaced in equation above to calculate the corresponding sensitivity value.

A.12. MATSEDLAB_app_02.m

In script *MATSEDLAB_app_02.m*, the description of organic matter degradation is based on the classic G-model. We assume that there are two reactive pools of organic carbon: the more and less reactive pools are assigned first-order degradation constants kOM1 and kOM2 of 0.1 and 0.001 yr^{-1}, respectively. The deposition fluxes of the two types of organic carbon, J_{OM1} and J_{OM2}, are specified as upper boundary conditions. (Note: in *MATSEDLAB_app_02.m* the reactions involving As have been removed)

The *MATSEDLAB_app_02.pdf* script presents two options for J_{OM1} and J_{OM2}, which can be turned on or off by the user (see lines 122-126). In the first option, J_{OM1} and J_{OM2} are assigned constant values of 300 and 150 µmol C cm^{-2} yr^{-1}. In the second option, the deposition fluxes JOM1 J_{OM1} and J_{OM2} are assumed to peak in early summer with the maximum value of 600 and 300 µmol C cm^{-2} yr^{-1} respectively, according to the sinusoidal boundary conditions, $J_{OM1} = 300[\cos(2\pi t) + 1]$ and $J_{OM2} = 150[\cos(2\pi t) + 1]$, where t=0 corresponds to July 1, and the depositional fluxes drop to zero in January.

A.13. MATSEDLAB _app_03.m

Here, we expand the representation of Fe(III)-bearing mineral phases used in the scripts discussed earlier by explicitly including goethite/lepidocrocite (both lumped in one phase) and magnetite, in addition to HFO, into the MATSEDLAB_app_03.m script. The system of reactions involving the Fe(III) minerals, summarized in Table 7, is inspired by the work of Pallud et al. (2010), who studied the reductive dissolution of ferrihydrite and the accompanying formation of secondary Fe minerals in soil aggregates. The reaction stoichiometry and rate expressions are implemented in *MATSEDLAB _app_03.m* on lines 208-212, respectively.

A.14. MATLAB Keywords

MATSEDLAB relies on MATLAB core functions to operate. The user is invited to familiarize him/herself with MATLAB first through the extensive MATLAB help or using the following get-going sheets available online at:

www.mathworks.com/help/pdf_doc/matlab/getstart.pdf

Below, we define briefly some of the MATLAB formulation encountered in the MATSEDLAB code files. The definition of the each MATLAB command is written in Italics.

>> global

Declaring the variables as global will make them available in the base workspace. They can be retrieved later either for plotting purposes or to save them in a file.

>> y=linspace (a,b,n)

Generates a row vector **y** *of* **n** *points linearly spaced between* **a** *and* **b**.

>> VarNames = {'O2(aq)',...}

Generates an array of the species names.

>> NumVars = int16(length(VarNames))

Retrieves number of the species.

>> SimValues = cell(NumVars, 1)

Initializes an array of empty matrices whose dimensions corresponds to **NumVars**

>> sol = pdepe(m,@pdex14pde,@pdex1ic,@pdex1bc,x,t)

Calls the **pdepe** *solver by passing the geometry of the domain (***m***) as well as the spatial(***x***) and temporal (***t***) ranges. The solver is configured with the functions* **pdex14pde**, *which solves the transport-reaction problem in conjunction with* **pdex1ic** *(initial condition) and* **pdex1bc** *(boundary condition).*

>> [c,f,s] = pdex14pde(x,t,u,DuDx)

Computes the terms **c** *(a diagonal matrix which couples the partial derivatives with respect to time),* **f** *(the flux matrix), and* **s** *(the reaction matrix). The input arguments are scalars* **x** *and* **t** *and vectors* **u** *and* **dudx** *that approximate the solution* **u** *and its partial derivative with respect to* **x**, *respectively.* **c**, **f**, *and* **s** *are column vectors.*

>> u = icfun(x)

icfun *evaluates the initial conditions. When called with an argument x, it evaluates and returns the initial values of the solution components at x in the column vector u.*

>> [pl,ql,pr,qr] = bcfun(xl,ul,xr,ur,t)

bcfun *evaluates the terms* **p** *and* **q** *of the boundary conditions.* ***ul*** *and* ***ur*** *are the approximate solutions at the upper and lower boundaries* **xl** *and* **xr** respectively. **pl** *and* **ql** *are column vectors corresponding to* **p** *and* **q** *evaluated at* **xl**, *and* **pr** *and* **qr** *correspond the same vectors evaluated at* **xr**.

>> TimeStep = b

Defines the time at which the simulation must be stopped.

REFERENCES

Acharya, R., 2004. Upscaling of nonlinear reactive transport: from pore to core. Wageningen University'

Aguilera, D.R., Jourabchi, P., Spiteri, C., Regnier, P., 2005. A knowledge-based reactive transport approach for the simulation of biogeochemical dynamics in Earth systems. Geochemistry Geophysics Geosystems 6.

Appelo, C.A.J., 1994. Cation and Proton-Exchange, Ph Variations, and Carbonate Reactions in a Freshening Aquifer. Water Resources Research 30, 2793-2805.

Avrami, M., 1941. Granulation, Phase Change, and Microstructure - Kinetics of Phase Change. III. Journal of Chemical Physics 9, 177-184.

Bahr, J.M., Rubin, J., 1987. Direct Comparison of Kinetic and Local Equilibrium Formulations for Solute Transport Affected by Surface-Reactions. Water Resources Research 23, 438-452.

Bear, J., 1972. Dynamics of fluids in porous media. Elsevier: New York.

Belzile, N., Tessier, A., 1990. Interactions between Arsenic and Iron Oxyhydroxides in Lacustrine Sediments. Geochimica Et Cosmochimica Acta 54, 103-109.

Berner, R.A., 1964. An Idealized Model of Dissolved Sulfate Distribution in Recent Sediments. Geochimica Et Cosmochimica Acta 28, 1497-1503.

Berner, R.A., 1976. Inclusion of Adsorption in Modeling of Early Diagenesis. Earth and Planetary Science Letters 29, 333-340.

Berner, R.A., 1980. Early Diagenesis: A Theoretical Approach. Princeton University Press.

Bethke, C.M., Brady, P.V., 2000. How the K-d approach undermines ground water cleanup. Ground Water 38, 435-443.

Blunt, M.J., 2001. Flow in porous media - pore-network models and multiphase flow. Current Opinion in Colloid & Interface Science 6, 197-207.

Borch, T., Kretzschmar, R., Kappler, A., Van Cappellen, P., Ginder-Vogel, M., Voegelin, A., Campbell, K., 2010. Biogeochemical Redox Processes and their Impact on Contaminant Dynamics. Environmental science & technology 44, 15-23.

Bostick, B.C., Chen, C., Fendorf, S., 2004. Arsenite retention mechanisms within estuarine sediments of Pescadero, CA. Environmental science & technology 38, 3299-3304.

Bostick, B.C., Fendorf, S., 2003. Arsenite sorption on troilite (FeS) and pyrite (FeS2). Geochimica Et Cosmochimica Acta 67, 909-921.

Boudreau, B.P., 1997. Diagenetic models and their implementations. Springer-Verlag, New York

Boudreau, B.P., 1999. Metals and models: Diagenetic modelling in freshwater lacustrine sediments. J. Paleolimnol. 22, 227-251.

Canavan, R.W., Slomp, C.P., Jourabchi, P., Van Cappellen, P., Laverman, A.M., Van den Berg, G.A., 2006. Organic matter mineralization in sediment of a coastal freshwater lake and response to salinization. Geochimica Et Cosmochimica Acta 70, 2836-2855.

Carlsaw, H.S., and Jaeger, J.C., 1959. Conduction of Heat in Solids, 2nd ed. Oxford University Press.

Cathalot, C., Rabouille, C., Pastor, L., Deflandre, B., Viollier, E., Buscail, R., Gremare, A., Treignier, C., Pruski, A., 2010. Temporal variability of carbon recycling in coastal sediments influenced by rivers: assessing the impact of flood inputs in the Rhone River prodelta. Biogeosciences 7, 1187-1205.

Chen, C.T.A., Borges, A.V., 2009. Reconciling opposing views on carbon cycling in the coastal ocean: Continental shelves as sinks and near-shore ecosystems as sources of atmospheric CO2. Deep-Sea Research Part Ii-Topical Studies in Oceanography 56, 578-590.

Chen, S., Doolen, G.D., 1998. Lattice Boltzmann method for fluid flows. Annual Review of Fluid Mechanics 30, 329-364.

Chen, W.L., Wagenet, R.J., 1995. Solute Transport in Porous-Media with Sorption-Site Heterogeneity. Environmental science & technology 29, 2725-2734.

Chopard, B., and Droz, M., 1998. Cellular Automata modeling of Physical systems. Cambridge University Press.

Cornell, R.M., Schwertmann, U., 2003. The Iron Oxides: Structure, Properties, Reactions, Occurrence and Uses, 2nd ed. Wiley VCH Publishers, New York.

Couture, R.M., Gobeil, C., Tessier, A., 2008. Chronology of atmospheric deposition of arsenic inferred from reconstructed sedimentary records. Environmental science & technology 42, 6508-6513.

Couture, R.M., Gobeil, C., Tessier, A., 2010a. Arsenic, iron and sulfur co-diagenesis in lake sediments. Geochimica Et Cosmochimica Acta 74, 1238-1255.

Couture, R.M., Shafei, B., Van Cappellen, P., Tessier, A., Gobeil, C., 2010b. Non-Steady State Modeling of Arsenic Diagenesis in Lake Sediments. Environmental science & technology 44, 197-203.

Cushman, J.H., Bennethum, L.S., Hu, B.X., 2002. A primer on upscaling tools for porous media. Advances in Water Resources 25, 1043-1067.

Dale, A.W., Bruchert, V., Alperin, M., Regnier, P., 2009. An integrated sulfur isotope model for Namibian shelf sediments. Geochimica Et Cosmochimica Acta 73, 1924-1944.
Darland, J.E., Inskeep, W.P., 1997. Effects of pore water velocity on the transport of arsenate. Environmental science & technology 31, 704-709.

Dentz, M., Berkowitz, B., 2005. Exact effective transport dynamics in a one-dimensional random environment. Physical Review E 72.

Dixit, S., Hering, J.G., 2003. Comparison of arsenic(V) and arsenic(III) sorption onto iron oxide minerals: Implications for arsenic mobility. Environmental science & technology 37, 4182-4189.

Elkhatib, E.A., Bennett, O.L., Wright, R.J., 1984. Kinetics of Arsenite Sorption in Soils. Soil Science Society of America Journal 48, 758-762.

Englert, A., Hubbard, S.S., Williams, K.H., Li, L., Steefel, C.I., 2009. Feedbacks Between Hydrological Heterogeneity and Bioremediation Induced Biogeochemical Transformations. Environmental science & technology 43, 5197-5204.

Fendorf, S., Eick, M.J., Grossl, P., Sparks, D.L., 1997. Arsenate and chromate retention mechanisms on goethite .1. Surface structure. Environmental science & technology 31, 315-320.

Frisch, U., d'Humieres, D., Hasslacher, B., Lallemand, P., Pomeau, Y., Rivet, J.P., 1987. Lattice gas hydrodynamics in two and three dimensions. Complex Systems 1, 649-707.

Ginzburg, I., 2005. Equilibrium-type and link-type lattice Boltzmann models for generic advection and anisotropic-dispersion equation. Advances in Water Resources 28, 1171-1195.

Ginzburg, I., d'Humieres, D., Kuzmin, A., 2010. Optimal Stability of Advection-Diffusion Lattice Boltzmann Models with Two Relaxation Times for Positive/Negative Equilibrium. Journal of Statistical Physics 139, 1090-1143.

Goldberg, S., Criscenti, L.J., Turner, D.R., Davis, J.A., Cantrell, K.J., 2007. Adsorption - Desorption processes in subsurface reactive transport modeling. Vadose Zone Journal 6, 407-435.

Haggerty, R., McKenna, S.A., Meigs, L.C., 2000. On the late-time behavior of tracer test breakthrough curves. Water Resources Research 36, 3467-3479.

Hansel, C.M., Benner, S.G., Neiss, J., Dohnalkova, A., Kukkadapu, R.K., Fendorf, S., 2003. Secondary mineralization pathways induced by dissimilatory iron reduction of ferrihydrite under advective flow. Geochimica Et Cosmochimica Acta 67, 2977-2992.

Hersum, T.G., Marsh, B.D., 2006. Igneous microstructures from kinetic models of crystallization. Journal of Volcanology and Geothermal Research 154, 34-47.

Hesse, F., Radu, F.A., Thullner, M., Attinger, S., 2009. Upscaling of the advection-diffusion-reaction equation with Monod reaction. Advances in Water Resources 32, 1336-1351.

Higuera, F.J., Jimenez, J., 1989. Boltzmann Approach to Lattice Gas Simulations. Europhysics Letters 9, 663-668.

Huber, C., Parmigiani, A., Chopard, B., Manga, M., Bachmann, O., 2008. Lattice Boltzmann model for melting with natural convection. International Journal of Heat and Fluid Flow 29, 1469-1480.

Hyacinthe, C., Bonneville, S., Van Cappellen, P., 2006. Reactive iron(III) in sediments: Chemical versus microbial extractions. Geochimica Et Cosmochimica Acta 70, 4166-4180.

Jennings, A.A., Kirkner, D.J., 1984. Instantaneous Equilibrium Approximation Analysis. Journal of Hydraulic Engineering-Asce 110, 1700-1717.

Jia, Y.F., Xu, L.Y., Fang, Z., Demopoulos, G.P., 2006. Observation of surface precipitation of arsenate on ferrihydrite. Environmental science & technology 40, 3248-3253.

Jung, H.B., Charette, M.A., Zheng, Y., 2009. Field, Laboratory, and Modeling Study of Reactive Transport of Groundwater Arsenic in a Coastal Aquifer. Environmental science & technology 43, 5333-5338.

Kang, Q.J., Lichtner, P.C., Janecky, D.R., 2010. Lattice Boltzmann Method for Reacting Flows in Porous Media. Advances in Applied Mathematics and Mechanics 2, 545-563.

Kang, Q.J., Lichtner, P.C., Zhang, D.X., 2006. Lattice Boltzmann pore-scale model for multicomponent reactive transport in porous media. Journal of Geophysical Research-Solid Earth 111.

Kang, Q.J., Lichtner, P.C., Zhang, D.X., 2007. An improved lattice Boltzmann model for multicomponent reactive transport in porous media at the pore scale. Water Resources Research 43.

Kang, Q.J., Zhang, D.X., Chen, S.Y., 2003. Simulation of dissolution and precipitation in porous media. Journal of Geophysical Research-Solid Earth 108.

Kang, Q.J., Zhang, D.X., Chen, S.Y., He, X.Y., 2002. Lattice Boltzmann simulation of chemical dissolution in porous media. Physical Review E 65.

Kang, Q.J., Zhang, D.X., Lichtner, P.C., Tsimpanogiannis, I.N., 2004. Lattice Boltzmann model for crystal growth from supersaturated solution. Geophysical Research Letters 31.

Katsev, S., Rancourt, D.G., L'Heureux, I., 2004. dSED: a database tool for modeling sediment early diagenesis. Computers & Geosciences 30, 959-967.

Kechagia, P.E., Tsimpanogiannis, I.N., Yortsos, Y.C., Lichtner, P.C., 2002. On the upscaling of reaction-transport processes in porous media with fast or finite kinetics. Chemical Engineering Science 57, 2565-2577.

Kelemen, P.B., Whitehead, J.A., Aharonov, E., Jordahl, K.A., 1995. Experiments on Flow Focusing in Soluble Porous-Media, with Applications to Melt Extraction from the Mantle. Journal of Geophysical Research-Solid Earth 100, 475-496.

Knapp, R.B., 1989. Spatial and Temporal Scales of Local Equilibrium in Dynamic Fluid-Rock Systems. Geochimica Et Cosmochimica Acta 53, 1955-1964.

Kocar, B.D., Borch, T., Fendorf, S., 2010. Arsenic repartitioning during biogenic sulfidization and transformation of ferrihydrite. Geochimica Et Cosmochimica Acta 74, 980-994.

Kumblad, L., Gilek, M., Naeslund, B., Kautsky, U., 2003. An ecosystem model of the environmental transport and fate of carbon-14 in a bay of the Baltic Sea, Sweden. Ecological Modelling 166, 193-210.

Li, L., Peters, C.A., Celia, M.A., 2006. Upscaling geochemical reaction rates using pore-scale network modeling. Advances in Water Resources 29, 1351-1370.

Li, L., Peters, C.A., Celia, M.A., 2007. Effects of mineral spatial distribution on reaction rates in porous media. Water Resources Research 43.

Li, L., Steefel, C.I., Yang, L., 2008. Scale dependence of mineral dissolution rates within single pores and fractures. Geochimica Et Cosmochimica Acta 72, 360-377.

Lichtner, P.C., 1985. Continuum Model for Simultaneous Chemical-Reactions and Mass-Transport in Hydrothermal Systems. Geochimica Et Cosmochimica Acta 49, 779-800.

Lichtner, P.C., 1988. The Quasi-Stationary State Approximation to Coupled Mass-Transport and Fluid-Rock Interaction in a Porous-Medium. Geochimica Et Cosmochimica Acta 52, 143-165.

Lichtner, P.C., Tartakovsky, D.M., 2003. Stochastic analysis of effective rate constant for heterogeneous reactions. Stochastic Environmental Research and Risk Assessment 17, 419-429.

Lovley, D.R., Phillips, E.J.P., 1986. Organic-Matter Mineralization with Reduction of Ferric Iron in Anaerobic Sediments. Applied and environmental microbiology 51, 683-689.

Lu, G.P., DePaolo, D.J., Kang, Q.J., Zhang, D.X., 2009. Lattice Boltzmann simulation of snow crystal growth in clouds. Journal of Geophysical Research-Atmospheres 114.

Luff, R., Haeckel, M., Wallmann, K., 2001. Robust and fast FORTRAN and MATLAB (R) libraries to calculate pH distributions in marine systems. Computers & Geosciences 27, 157-169.

Macquarrie, K.T.B., Sudicky, E.A., Frind, E.O., 1990. Simulation of Biodegradable Organic Contaminants in Groundwater .1. Numerical Formulation in Principal Directions. Water Resources Research 26, 207-222.

Manning, B.A., Fendorf, S.E., Goldberg, S., 1998. Surface structures and stability of arsenic(III) on goethite: Spectroscopic evidence for inner-sphere complexes. Environmental science & technology 32, 2383-2388.

Matisoff, G., Holdren, G.R., 1995. A Model for Sulfur Accumulation in Soft-Water Lake-Sediments. Water Resources Research 31, 1751-1760.

Meile, C., Tuncay, K., 2006. Scale dependence of reaction rates in porous media. Advances in Water Resources 29, 62-71.

Meysman, F.J.R., Middelburg, J.J., Herman, P.M.J., Heip, C.H.R., 2003a. Reactive transport in surface sediments. I. Model complexity and software quality. Computers & Geosciences 29, 291-300.

Meysman, F.J.R., Middelburg, J.J., Herman, P.M.J., Heip, C.H.R., 2003b. Reactive transport in surface sediments. II. Media: an object-oriented problem-solving environment for early diagenesis. Computers & Geosciences 29, 301-318.

Miller, W., Succi, S., 2002. A lattice Boltzmann model for anisotropic crystal growth from melt. Journal of Statistical Physics 107, 173-186.

Molins, S., and Silin, D., 2009. Pore-scale modeling of biogeochemical alteration of the transport properties of the sediment, AGU.

O'day, P.A., Vlassopoulos, D., Root, R., Rivera, N., 2004. The influence of sulfur and iron on dissolved arsenic concentrations in the shallow subsurface under changing redox

conditions. Proceedings of the National Academy of Sciences of the United States of America 101, 13703-13708.

Pallud, C., Kausch, M., Fendorf, S., Meile, C., 2010. Spatial Patterns and Modeling of Reductive Ferrihydrite Transformation Observed in Artificial Soil Aggregates. Environmental science & technology 44, 74-79.

Parmigiani, A., Huber, C., Bachmann, O., Chopard, B., 2011. Pore-scale mass and reactant transport in multiphase porous media flows. Journal of Fluid Mechanics 686, 40-76.

Pastor, L., Cathalot, C., Deflandre, B., Viollier, E., Soetaert, K., Meysman, F.J.R., Ulses, C., Metzger, E., Rabouille, C., 2011. Modeling biogeochemical processes in sediments from the Rhone River prodelta area (NW Mediterranean Sea). Biogeosciences 8, 1351-1366.

Pedersen, H.D., Postma, D., Jakobsen, R., 2006. Release of arsenic associated with the reduction and transformation of iron oxides. Geochimica Et Cosmochimica Acta 70, 4116-4129.

Pratihary, A.K., Naqvi, S.W.A., Naik, H., Thorat, B.R., Narvenkar, G., Manjunatha, B.R., Rao, V.P., 2009. Benthic fluxes in a tropical Estuary and their role in the ecosystem. Estuarine Coastal and Shelf Science 85, 387-398.

Pruess, K., 1991. TOUGH2: A general simulator for multiphase fluid and heat flow. Lawrence Berkeley Laboratory, Berkeley, CA.

Qi, Y.Q., Donahoe, R.J., 2008. The environmental fate of arsenic in surface soil contaminated by historical herbicide application. Science of the Total Environment 405, 246-254.

Qi, Y.Q., Donahoe, R.J., 2011. Modeling Arsenic Sorption in the Subsurface with a Dual-Site Model. Ground Water 49, 219-226.

Qian, Y.H., Dhumieres, D., Lallemand, P., 1992. Lattice Bgk Models for Navier-Stokes Equation. Europhysics Letters 17, 479-484.

Raoof, A., Hassanizadeh, S.M., 2010. Upscaling Transport of Adsorbing Solutes in Porous Media. Journal of Porous Media 13, 395-408.

Redman, A.D., Macalady, D.L., Ahmann, D., 2002. Natural organic matter affects arsenic speciation and sorption onto hematite. Environmental science & technology 36, 2889-2896.

Regnier, P., Jourabchi, P., Slomp, C.P., 2003. Reactive-transport modeling as a technique for understanding coupled biogeochemical processes in surface and subsurface environments. Netherlands Journal of Geosciences-Geologie En Mijnbouw 82, 5-18.

Root, R.A., Dixit, S., Campbell, K.M., Jew, A.D., Hering, J.G., O'Day, P.A., 2007. Arsenic sequestration by sorption processes in high-iron sediments. Geochimica Et Cosmochimica Acta 71, 5782-5803.

Sahai, N., Lee, Y.J., Xu, H.F., Ciardelli, M., Gaillard, J.F., 2007. Role of Fe(II) and phosphate in arsenic uptake by coprecipitation. Geochimica Et Cosmochimica Acta 71, 3193-3210.

Sanchez-Vila, X., Dentz, M., Donado, L.D., 2007. Transport-controlled reaction rates under local non-equilibrium conditions. Geophysical Research Letters 34.

Schauser, I., Hupfer, M., Bruggemann, R., 2006. Sensitivity analysis with a phosphorus diagenesis model (SPIEL). Ecological Modelling 190, 87-98.

Scheibe, T.D., Fang, Y.L., Murray, C.J., Roden, E.E., Chen, J.S., Chien, Y.J., Brooks, S.C., Hubbard, S.S., 2006. Transport and biogeochemical reaction of metals in a physically and chemically heterogeneous aquifer. Geosphere 2, 220-235.

Schulz, M., Kohler, J., 2006. A simple model of phosphorus retention evoked by submerged macrophytes in lowland rivers. Hydrobiologia 563, 521-525.

Servan-Camas, B., Tsai, F.T.C., 2008. Lattice Boltzmann method with two relaxation times for advection-diffusion equation: Third order analysis and stability analysis. Advances in Water Resources 31, 1113-1126.

Skeel, R.D., Berzins, M., 1990. A Method for the Spatial Discretization of Parabolic Equations in One Space Variable. Siam Journal on Scientific and Statistical Computing 11, 1-32.

Smedley, P.L., Kinniburgh, D.G., 2002. A review of the source, behaviour and distribution of arsenic in natural waters. Applied Geochemistry 17, 517-568.

Soetaert, K., Herman, P.M.J., Middelburg, J.J., 1996. A model of early diagenetic processes from the shelf to abyssal depths. Geochim Cosmochim Ac 60, 1019-1040.

Steefel, C.I., DePaolo, D.J., Lichtner, P.C., 2005. Reactive transport modeling: An essential tool and a new research approach for the Earth sciences. Earth and Planetary Science Letters 240, 539-558.

Steefel, C.I., Vancappellen, P., 1990. A New Kinetic Approach to Modeling Water-Rock Interaction - the Role of Nucleation, Precursors, and Ostwald Ripening. Geochimica Et Cosmochimica Acta 54, 2657-2677.

Stiebler, M., Toelke, J., Krafczyk, M., 2008. Advection-diffusion lattice Boltzmann scheme for hierarchical grids. Computers & Mathematics with Applications 55, 1576-1584.

Succi, S., 2001. The Lattice Boltzmann Equation for Fluid Dynamics and Beyond. Oxford University Press, New York.

Suga, S., 2006. Numerical schemes obtained from lattice Boltzmann equations for advection diffusion equations. International Journal of Modern Physics C 17, 1563-1577.

Szegedi, K., Vetterlein, D., Nietfeld, H., Jahn, R., Neue, H.U., 2008. New tool RhizoMath for modeling coupled transport and speciation in the rhizosphere. Vadose Zone Journal 7, 712-720.

Tartakovsky, A.M., Meakin, P., Scheibe, T.D., Wood, B.D., 2007. A smoothed particle hydrodynamics model for reactive transport and mineral precipitation in porous and fractured porous media. Water Resources Research 43.

Tartakovsky, A.M., Redden, G., Lichtner, P.C., Scheibe, T.D., Meakin, P., 2008. Mixing-induced precipitation: Experimental study and multiscale numerical analysis. Water Resources Research 44.

Tokoro, C., Yatsugi, Y., Koga, H., Owada, S., 2010. Sorption Mechanisms of Arsenate during Coprecipitation with Ferrihydrite in Aqueous Solution. Environmental science & technology 44, 638-643.

Torres E., C.R.M., Shafei B., Ruiz Cánovas C., Ayora C., 2011. Sediment Diagenesis Modelling in a AMD Contaminated Reservoir. MACLA 15, 191-192.

Tronc, E., Belleville, P., Jolivet, J.P., Livage, J., 1992. Transformation of Ferric Hydroxide into Spinel by Fe(Ii) Adsorption. Langmuir 8, 313-319.

Valocchi, A.J., 1985. Validity of the Local Equilibrium Assumption for Modeling Sorbing Solute Transport through Homogeneous Soils. Water Resources Research 21, 808-820.

Valocchi, A.J., Street, R.L., Roberts, P.V., 1981. Transport of Ion-Exchanging Solutes in Groundwater - Chromatographic Theory and Field Simulation. Water Resources Research 17, 1517-1527.

VanCappellen, P., Gaillard, J.F., 1996. Biogeochemical dynamics in aquatic sediments. Reactive Transport in Porous Media 34, 335-376.

VanCappellen, P., Wang, Y.F., 1996. Cycling of iron and manganese in surface sediments: A general theory for the coupled transport and reaction of carbon, oxygen, nitrogen, sulfur, iron, and manganese. American Journal of Science 296, 197-243.

Walsh, S.D.C., Burwinkle, H., Saar, M.O., 2009. A new partial-bounceback lattice-Boltzmann method for fluid flow through heterogeneous media. Computers & Geosciences 35, 1186-1193.

Wang, Y.F., VanCappellen, P., 1996. A multicomponent reactive transport model of early diagenesis: Application to redox cycling in coastal marine sediments. Geochimica Et Cosmochimica Acta 60, 2993-3014.

Westrich, J.T., Berner, R.A., 1984. The Role of Sedimentary Organic-Matter in Bacterial Sulfate Reduction - the G Model Tested. Limnology and Oceanography 29, 236-249.

Wolf-Gladrow, D.A., 2000. Lattice-gas cellular automata and lattice Boltzmann models - Introduction. Lattice-Gas Cellular Automata and Lattice Boltzmann Models 1725, 1-13.

Wolthers, M., Charlet, L., Van der Weijden, C.H., Van der Linde, P.R., Rickard, D., 2005. Arsenic mobility in the ambient sulfidic environment: Sorption of arsenic(V) and arsenic(III) onto disordered mackinawite. Geochimica Et Cosmochimica Acta 69, 3483-3492.

Xu, T., Sonnenthal, E., Spycher, N., and Pruess, K., 2003. TOUGHREACT: A new code of the TOUGH family for non-isothermal multiphase reactive geochemical transport in variably saturated geologic media. Lawrence Berkeley Laboratory, Berkeley, CA.

Yang, L., Steefel, C.I., Marcus, M.A., Bargar, J.R., 2010. Kinetics of Fe(II)-Catalyzed Transformation of 6-line Ferrihydrite under Anaerobic Flow Conditions. Environmental science & technology 44, 5469-5475.

Yeh, G.T., Tripathi, V.S., 1989. A Critical-Evaluation of Recent Developments in Hydrogeochemical Transport Models of Reactive Multichemical Components. Water Resources Research 25, 93-108.

Yudianto, D., Xie, Y.B., 2010. A comparison of some numerical methods in solving 1-D steady-state advection dispersion reaction equation. Civil Engineering and Environmental Systems 27, 155-172.

Zavala-Sanchez, V., Dentz, M., Sanchez-Vila, X., 2007. Effective dispersion in a chemically heterogeneous medium under temporally fluctuating flow conditions. Advances in Water Resources 30, 1342-1354.

Zhang, H., Selim, H.M., 2006. Modeling the transport and retention of arsenic (V) in soils. Soil Science Society of America Journal 70, 1677-1687.

Zhang, H., Selim, H.M., 2008. Reaction and transport of arsenic in soils: Equilibrium and kinetic modeling. Advances in Agronomy, Vol 98 98, 45-115.

Zhang, X.X., Bengough, A.G., Deeks, L.K., Crawford, J.W., Young, I.M., 2002. A novel three-dimensional lattice Boltzmann model for solute transport in variably saturated porous media. Water Resources Research 38.

Zhang, X.X., Crawford, J.W., Young, L.M., 2008. Does pore water velocity affect the reaction rates of adsorptive solute transport in soils? Demonstration with pore-scale modelling. Advances in Water Resources 31, 425-437.

Zou, Q.S., He, X.Y., 1997. On pressure and velocity boundary conditions for the lattice Boltzmann BGK model. Physics of Fluids 9, 1591-1598.